

# PHOTOCHEMICAL AND PHOTOPHYSICAL PROPERTIES OF DIKETOPYRROLOPYRROLE ORGANIC PIGMENTS

THÈSE N° 1616 (1997)

PRÉSENTÉE AU DÉPARTEMENT DE CHIMIE

ÉCOLE POLYTECHNIQUE FÉDÉRALE DE LAUSANNE

POUR L'OBTENTION DU GRADE DE DOCTEUR ÈS SCIENCES

PAR

**Martin ESCHLE**

Ingénieur physicien diplômé EPF  
originaire de Lucerne et Entlebuch (LU)

acceptée sur proposition du jury:

Prof. M. Grätzel, directeur de thèse  
Prof. J.-P. Ansermet, corapporteur  
Prof. A. Braun, corapporteur  
Dr A. Iqbal, corapporteur  
Dr J.-E. Moser, corapporteur

Lausanne, EPFL  
1997

To my parents

## Abstract

Various aspects of the pigment class based on 1,4-diketo-3,6-diphenylpyrrolo(3,4-c)pyrrole (DPP) are investigated. The thesis consists of two parts: the first part, motivated by the degradation problems of DPP, focuses on the molecular photophysics of the DPP class of compounds. The second part, motivated by photovoltaic applications, focuses on the electrical and photovoltaic properties of solid state DPP.

Investigation of the photoluminescence of the main commercial derivative, *p*-Cl DPP (PCD) showed, that the emission of the pigment in polymer matrices may be attributed to aggregates at the surface and that it is sensitized by monomers of DPP. From the distinct excitation spectrum of the monomers it is thus concluded that these play a major role in the photoactivity and photodegradation of the pigments.

In solution the dominant role of singlet oxygen in the degradation of the molecule has been shown. The quenching of the singlet excited state of DPP by oxygen efficiently produces singlet oxygen and triplet states of DPP. The latter is again an efficient sensitizer of singlet oxygen. The triplet state energy has been measured for DPP ( $28.5 \pm 2$  kcal/mol) and the *p*-dimethylamino derivative DMADPP ( $29.5 \pm 2$  kcal/mol). The triplet energy for DMADPP is slightly higher than for DPP, although the respective singlet energies have the opposite trend (DPP: 56 kcal/mol and DMADPP: 51 kcal/mol). Based on molecular orbital calculations this observation is attributed to the structure of the HOMO and LUMO orbitals and it is concluded that the large singlet to triplet energy splitting is a property of the core of the pyrrolopyrrole chromophore.

DPP and DTPP (dithioketo-DPP) are used in electrochemical and heterojunction solid state photovoltaic cells based on porous TiO<sub>2</sub> electrodes. MCDPP, a derivative of DPP using a carboxylic anchoring group yielded an incident photon to current conversion efficiency of 47% in a photoelectrochemical cell. The solid state photovoltaic cells yielded poor photocurrents. The use of MCDPP in the TiO<sub>2</sub>/DPP heterojunction increased the photocurrent.

Surface photovoltage spectroscopy and Kelvin probe measurements were used to determine the workfunction of DPP (5.38 eV), DTPP (4.95 eV) and DMADPP (5.08 eV) and to investigate surface and interface band bendings of DTPP on SnO<sub>2</sub>. A band diagram is proposed for this system. DTPP and DPP showed both *p*-type band bending.

## Résumé

Ce travail concerne l'étude de la classe des pigments 1,4-dicéto-3,6-diphényl-pyrrolo(3,4-c)pyrrole (DPP). Dans la première partie, motivée par les problèmes de dégradation du DPP, on s'intéresse à leur photophysique moléculaire. La seconde partie traite des propriétés électriques et photochimiques de ce matériau en phase solide, dans l'optique d'applications photovoltaïques.

Des études de la photoluminescence du principal dérivé commercial, p-CI DPP (PCD), ont montré que l'émission du pigment dispersé dans une matrice de polymère peut être attribuée aux agrégats de surface et qu'elle est sensibilisée par les monomères. On conclut à partir de l'observation du spectre d'excitation distinct du monomère, que celui-ci joue un rôle primordial dans la photoactivité et la photodégradation des pigments.

En solution, l'oxygène singulet a un rôle déterminant dans le processus de dégradation de la molécule. L'oxygène singulet est sensibilisé efficacement par le *quenching* de l'état excité singulet du DPP qui conduit à l'état triplet du DPP. Celui-ci est à son tour un sensibilisateur efficace menant à l'oxygène singulet. Les énergies des états triplets ont été mesurées pour le DPP ( $28.5 \pm 2$  kcal/mol) et pour le dérivé p-diméthylamino DMADPP ( $29.5 \pm 2$  kcal/mol). L'énergie de l'état triplet du DMADPP est légèrement supérieure à celle du DPP, bien que les énergies respectives des états singulets aient des tendances opposées (DPP: 56 kcal/mol, DMADPP: 51 kcal/mol). Sur la base de calculs d'orbitales moléculaires, on attribue ces observations à la structure des orbitales HOMO et LUMO; on en conclut que le grand éclatement des niveaux singulets et triplets est une propriété du noyau du chromophore pyrrolo-pyrrole.

Le DPP et le DTPP (dithiocéto-DPP) sont utilisés dans des cellules photovoltaïques électrochimiques et à l'état solide basées sur des électrodes poreuses de TiO<sub>2</sub>. Le MCDPP, dérivé du DPP avec groupe d'attache carboxylique, a permis d'atteindre une efficacité de conversion de l'intensité lumineuse monochromatique incidente en courant de 47% dans une cellule photoélectrochimique. Les cellules photovoltaïques à l'état solide, donnent de faibles photocourants. L'adjonction de MCDPP dans la jonction TiO<sub>2</sub>/DPP permet d'augmenter le photocourant.

La *surface photovoltage spectroscopy* (SPS) et des mesures sonde de Kelvin permettent la détermination de la fonction de travail du DPP (5.38 eV), DTPP (4.95 eV) et du DMADPP (5.08 eV), et d'étudier la courbure de bandes surfacique et interfaciale du DTPP sur SnO<sub>2</sub>. Un diagramme de bandes a été proposé pour ce système. Le DPP et le DTPP montrent tous deux une courbure de bande caractéristique d'un dopage p.



# Table of contents

Abstract.....	I
Résumé .....	II
Table of contents .....	III
<b>1. Introduction.....</b>	<b>1</b>
References .....	3
<b>2. Experimental.....</b>	<b>5</b>
2.1. Materials .....	5
2.1.1. Synthesis of MCDPP.....	6
2.1.2. Other chemicals .....	7
2.1.3. Evaporated layers.....	7
2.2. Experimental setups.....	8
2.2.1. Laser flash photolysis .....	8
2.2.2. Fluorescence lifetime measurements .....	9
2.2.3. Absorption and fluorescence spectra .....	9
2.2.4. Solar cell characterization .....	9
2.2.5. Cyclic voltammetry.....	10
2.2.6. Time of Flight measurements.....	10
2.2.7. Surface photovoltage spectroscopy (SPV/SPS).....	10
2.2.8. Computational methods .....	11
2.3. References .....	11
<b>3. Pigment surface.....</b>	<b>12</b>
3.1. Introduction.....	12
3.2. Sample preparation .....	12
3.3. Results and discussion .....	14
3.3.1. Absorption spectra .....	14
3.3.2. Fluorescence spectra .....	16
3.4. Conclusion .....	24
3.5. References .....	25
<b>4. Photophysics and photochemistry of the DPP monomers .....</b>	<b>26</b>
4.1. Introduction.....	26
4.2. Absorption and fluorescence .....	27
4.2.1. Radiative Lifetimes .....	28
4.2.2. Transition dipole moment .....	30
4.3. Reactions with singlet oxygen .....	33
4.3.1. Experimental.....	33
4.3.2. Results and discussion .....	34
4.3.2.1. Singlet oxygen yield of DPP and DMDPP in solution .....	34
4.3.2.2. Kinetic model and degradation rates in different solvents .....	35
4.3.2.3. Influence of singlet oxygen and superoxide quenchers.....	40
4.3.3. Discussion and Conclusion.....	43

4.4. Triplet states .....	45
4.4.1. Theory and applied methods .....	45
4.4.1.1. Triplet energy transfer .....	46
4.4.2. Results and discussion .....	48
4.4.2.1. Identification of the triplet states sensitized by triplet donors .....	48
4.4.2.2. Triplet state energy .....	52
4.4.2.3. Triplet enhancement by O <sub>2</sub> .....	57
4.4.2.4. Triplet enhancement by TEMPO .....	62
4.5. Molecular Orbital Calculations based on Semiempirical Quantum Mechanical Methods .....	69
4.5.1. Theory .....	69
4.5.1.1. Methods used for calculation of electronic spectra .....	71
4.5.1.2. Method used for geometry optimization .....	73
4.5.2. Results and discussion .....	74
4.5.2.1. Geometries .....	74
4.5.2.2. Electronic spectra and shapes of molecular orbitals .....	77
4.6. Conclusion .....	82
4.7. References .....	83
5. Electrical and photovoltaic properties of solid state DPP and derivatives .....	87
5.1. Introduction .....	87
5.2. Heterogeneous charge injection from DPP derivatives adsorbed on TiO <sub>2</sub> .....	89
5.2.1. Adsorption onto TiO <sub>2</sub> .....	89
5.2.2. Fluorescence quenching on the surface of TiO <sub>2</sub> particles .....	91
5.2.3. Photovoltaic electrochemical cell .....	94
5.3. Conductivity of DMADPP .....	98
5.3.1. Experimental .....	99
5.3.2. Results and discussion .....	100
5.4. Solid state solar cells .....	101
5.4.1. Sample preparation .....	101
5.4.2. Results and discussion .....	102
5.5. Surface photovoltage spectroscopy .....	110
5.5.1. Theory of the SPV/SPS method .....	110
5.5.2. Sample preparation .....	114
5.5.3. Results and discussion .....	115
5.6. Conclusion .....	122
5.7. References .....	123
<b>6. Conclusion .....</b>	<b>127</b>
<b>Acknowledgement .....</b>	<b>129</b>
<b>Curriculum vitae .....</b>	<b>130</b>

# 1. Introduction

In the Penguin Books Dictionary of Chemistry<sup>1</sup> we find:

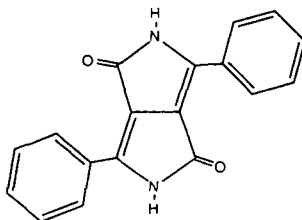
*“pigments Materials which are used to impart color to surfaces, plastics, inks, etc., although the pigments may incidentally affect other properties of the substrate. Distinct from dyestuffs which operate on a molecular level, pigments tend to be particulate and insoluble. ...”*

Organic pigments are a subject of increasing interest because of environmental and toxicological constraints. Nevertheless, the dominant pigment chromophores on the market, such as azos, perylenes and phthalocyanines have been known for 50 years or longer. One decade ago Iqbal et al.<sup>2,3</sup> have published the synthesis and application of a new class of pigments based of the new chromophore 1,4-diketopyrrolo(3,4-c)pyrrole (DPP). These pigments have known a large commercial success<sup>4</sup> and have a large environmental compatibility<sup>5</sup>.

The chromophore was first reported by Farnum et al.<sup>6</sup> and received the industrial interest only 6 years later. DPP pigments exhibit an intensive red color and a high brilliance due to its sharp absorption edge accompanied with a high fastness. These properties motivated the development of a palette of derivatives covering colors from yellow-red to violet-blue. All the DPP pigments are remarkably resistant to migration and highly insoluble<sup>2</sup> which is the major reason for their stability. The absorption of the compounds undergoes a bathochromic shift from solution to the solid state.<sup>7-13</sup>

The applications of DPP are not limited to paints and pigments for plastics. The hole conducting properties of this dye class have been reported by Mizuguchi et al.<sup>14-18</sup>. Its application for optical information storage system has been suggested by Mizuguchi<sup>8</sup> and Langhals<sup>19</sup>. Its fluorescent properties attracted the interest for the application of the DPP class in fluorescent solar collectors and dye lasers<sup>11,12,20</sup>. However, these potential applications have not yet been developed on a large scale. The application to organic photovoltaic devices has not yet been investigated.

The color and shade of pigmented substrates are mainly determined by the color properties of the pigment material itself, but scattering effects of the particles



1,4-diketo-3,6-diphenylpyrrolo(3,4-c)pyrrole (DPP)

and their optical properties also influence the final aspect. Changes of color, brilliance and shade are therefore not only due to the chromophore itself but also to the morphology of the particles and to the composed system of pigment and matrix. The stability of the polymer matrix has been continuously improved and is no longer the limiting element<sup>21</sup>, thus challenging the pigment development. Although DPP exhibits an extraordinary light fastness, photodegradation is the main problem for the long-term quality of these products. The stabilization by various well-known stabilizers had limited success<sup>21</sup> thus asking for a more profound investigation of the initiator steps of the photodegradation.

The first part of this thesis focuses on the photophysical and photochemical properties of degradation reactions of the DPP monomers. The importance of singlet oxygen is shown and the mechanism of its sensitization by DPP is investigated. Molecular orbital calculations are used to rationalize the experimental observations. The involvement of the monomer in the pigment/polymer system is shown through observations of fluorescence on the pigment particles in polymer matrices.

The use of the DPP class of compounds for photovoltaic applications is the focus of the second part. Organic solar cells offer potential for low cost alternatives as photoelectrochemical systems<sup>22,23</sup> or solid state devices<sup>24-30</sup> to the presently dominating technologies. However the best power conversion efficiencies achieved so far do not exceed 1%<sup>31-33</sup>.

DPP and the sulfur analog DTPP were used in solid state heterojunction photovoltaic cells. DPP was modified with a carboxylic anchoring group for TiO<sub>2</sub> and has been used as a sensitizer in a photoelectrochemical cell and as an interfacing molecule in a TiO<sub>2</sub>/DPP heterojunction solid state cell. Surface photovoltage (SPV) and surface photovoltage spectroscopy (SPS)<sup>34-37</sup> based on the Kelvin probe method was used to study the most promising compound, DTPP, and to propose a band model for the sandwich type photovoltaic cells.

## References

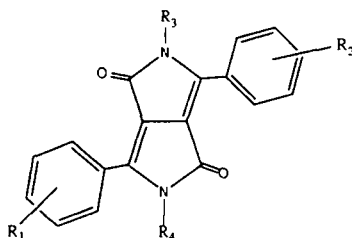
- (1) *Dictionary of Chemistry*; 2nd ed.; Sharp, D. W. A., Ed.; Penguin Books: London, 1990, pp 434.
- (2) Iqbal, A.; Cassar, L.; Rochat, A. C.; Pfenninger, J.; Wallquist, O. *Journal of Coatings Technology* **1988**, *60*, 37-45.
- (3) Iqbal, A.; Jost, M.; Kirchmayr, R.; Pfenninger, J.; Rochat, A.; Wallquist, O. *Bull. Soc. Chim. Belg.* **1988**, *97*, 615-643.
- (4) Jacob, A. *Neue Zürcher Zeitung* **1990**, 283, 69.
- (5) Flierl, K. *Revue Ciba* **1993**, *2*, 12.
- (6) Farnum, D. G.; Mehta, G.; Moore, G. G. I.; Siegal, F. P. *Tetrahedron Letters* **1974**, *29*, 2549-2552.
- (7) Mizuguchi, J.; Wooden, G. *Ber. Bunsenges. Phys. Chem.* **1991**, *95*, 1264-1274.
- (8) Mizuguchi, J.; Rochat, A. C. *J. Imag. Tech.* **1991**, *17*, 123-126.
- (9) Mizuguchi, J. Habilitation Thesis for Privatdozent Thesis, Bern, 1993.
- (10) Adachi, M.; Nakamura, S. *J. Phys. Chem.* **1994**, *98*, 1796-1801.
- (11) Langhals, H.; Potrawa, T.; Nöth, H.; Lüthi, G. *Angew. Chem. Int. Ed.* **1989**, *28*, 478-480.
- (12) Langhals, H.; Potrawa, T.; Nöth, H. *Angew. Chem.* **1989**, *101*, 497-499.
- (13) Srivatsavoy, V. J. P. "Size effect of DPP pigments on the absorption spectrum," EPFL-ICP2, manuscript in preparation.
- (14) Mizuguchi, J.; Rochat, A. C. *J. Imag. Sci.* **1988**, *32*, 135-140.
- (15) Mizuguchi, J. *J. Appl. Phys.* **1989**, *66*, 3111-3113.
- (16) Mizuguchi, J.; Homma, S. *J. Appl. Phys.* **1989**, *66*, 3104.
- (17) Mizuguchi, J.; Rihs, G. *Ber. Bunsenges. Phys. Chem.* **1992**, *96*, 597-606.
- (18) Mizuguchi, J. *Ber. Bunsenges. Phys. Chem.* **1993**, *97*, 684-701.
- (19) Langhals, H. *J. Inf. Rec. Mater.* **1991**, *19*, 449-454.
- (20) Langhals, H.; Potrawa, T. *Chem. Ber.* **1987**, *120*, 1075-1078.
- (21) Chassot, L. *Chimia* **1994**, *48*, 432-435.
- (22) O'Regan, B.; Grätzel, M. *Nature* **1991**, 353,
- (23) Nazeeruddin, M. K.; Kay, A.; Rodicio, I.; Humphry-Baker, R.; Müller, E.; Liska, P.; Vlachopoulos, N.; Grätzel, M. *J. Am. Chem. Soc.* **1993**, *115*, 6382-6390.
- (24) Skotheim, T.; Yang, J.-M.; Otvos, J.; Klein, M. P. *J. Chem. Phys.* **1982**, *77*, 6144-6150.
- (25) Wang, Y. In *Encyclopedia of Chemical Technology*; 4 ed.; Kirk-Othmer, Ed.; John Wiley & Sons: 1996; Vol. 18; pp 837.

- (26) Panayotatos, P.; Prikh, D.; Sauers, R.; Bird, G.; Peichowski, A.; Husain, S. *Solar Cells* **1986**, *18*, 71-84.
- (27) Yu, G.; Gao, J.; Hummelen, J. C.; Wudl, F.; Heeger, A. J. *Science* **1995**, *270*, 1789-1791.
- (28) Tsuzuki, T.; Hirota, B.; Noma, N.; Shirota, Y. *Thin Solid Films* **1996**, *273*, 177.
- (29) Hiramoto, M.; Fujiwara, H.; Yokoyama, M. *J. Appl. Phys.* **1992**, *72*, 3781-3787.
- (30) Hiramoto, M.; Fukusumi, H.; Yokoyama, M. *Appl. Phys. Lett.* **1992**, *61*, 2580-2582.
- (31) Tang, C. W. *Appl. Phys. Lett.* **1986**, *48*, 183.
- (32) Ghosh, A. K.; Feng, T. *J. Appl. Phys.* **1978**, *49*, 5982-5989.
- (33) Hiramoto, M.; Fujiwara, h.; Yokoyama, M. *Appl. Phys. Lett.* **1991**, *58*, 1062-1064.
- (34) Lagowski, J. *Surface Science* **1994**, *299/300*, 92.
- (35) Lüth, H. *Appl. Phys.* **1975**, *8*, 1.
- (36) Pfeiffer, M.; Leo, K.; Karl, N. *J. Appl. Phys.* **submitted**,
- (37) Moons, E.; Savenije, T.; Goossens, A. "Direct determination of surface potential of porphyrin layers on ITO using Kelvin probe technique," Delft University of Technology, manuscript in preparation.

# 2. Experimental

## 2.1. Materials

1,4 Diketo-pyrrolo[3,4-c]pyrrole (DPP) and its derivatives were received from CIBA unless otherwise stated. The compounds were used without further purification.



compound	R <sub>1</sub>	R <sub>2</sub>	R <sub>3</sub>	R <sub>4</sub>
DPP	H	H	H	H
PCD	p-Cl	p-Cl	H	H
DMDPP	H	H	-CH <sub>3</sub>	-CH <sub>3</sub>
DMADPP	p-N(CH <sub>3</sub> ) <sub>2</sub>	p-N(CH <sub>3</sub> ) <sub>2</sub>	H	H
DPADPP	p-N(C <sub>6</sub> H <sub>6</sub> ) <sub>2</sub>	p-N(C <sub>6</sub> H <sub>6</sub> ) <sub>2</sub>	H	H
MCDPP	H	H	CH <sub>2</sub> COOH	H

DTPP 1,4 Dithioketo-diphenyl-pyrrolo[3,4-c]pyrrole (DTPP) has been synthesized by CIBA according to the method described by Mizuguchi and Homma<sup>1</sup>.

The compound is unstable in oxygen containing solutions, but shows promising properties in the solid state. In oxygen containing solution the thiocarbonyl groups substitute rapidly with oxygen to form the carbonyl groups, thus yielding DPP and other degradation products. All solution experiments involving DTTP were done in Ar-bubbled degassed solutions.

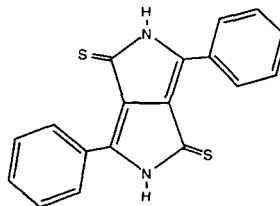
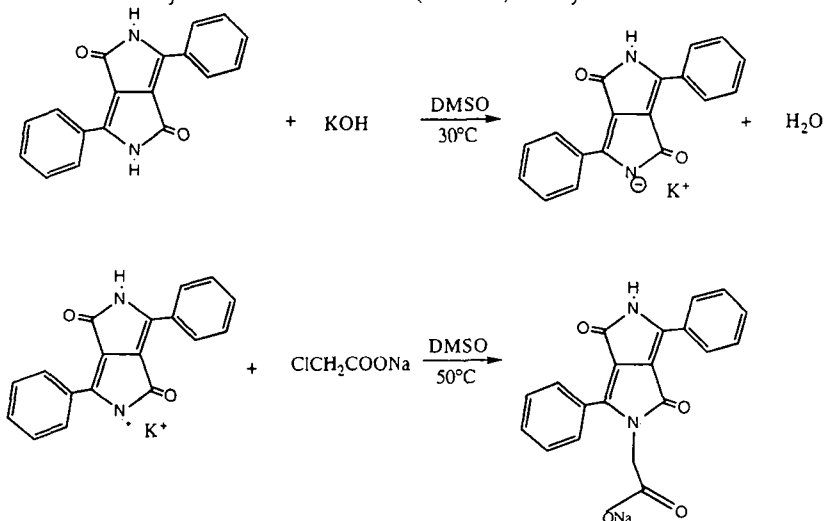


Fig. 2.1: DTTP

## 2.1.1. Synthesis of MCDPP

The monocarboxylated derivative of DPP (MCDPP) was synthesized at EPFL.



1.85 g DPP were added to 30 ml DMSO. The dissolution is not complete. 1.8 g (4.3 eqmol) of grinded KOH powder were added and the solution was stirred during 30 min. at room temperature. The absorption spectrum allowed to monitor the deprotonation of the nitrogen atom<sup>2</sup>. For the alkylation step 2.245 g (3 eqmol) of 1-chloroacetic sodium salt and the solution was then stirred for 3 hrs at 50°C. Again the absorption spectrum allowed to monitor the reaction. The solution was diluted with 300 ml water and filtered with a P4 glass frit filter. The compound was precipitated by acidifying the solution with 1 M HCl, filtered on a P4 filter and dried in a dessicator overnight, followed by 15 minutes drying under vacuum.

The product was further purified by extraction of the impurities from alkaline aqueous solution with 200 ml dichloromethane. The solvent extraction is repeated twice. The product is finally precipitated using 1M HCl, filtered with a P4 filter and dried. 826 mg of product are obtained. The yield is 45% with respect to initial DPP quantity.

The product is the mono-*N*-alkylated DPP, as concluded from the NMR spectrum (fig. 2.2) and the UV-vis absorption spectrum. Comparison of the MCDPP spectrum to the mono-*N*-methylated DPP synthesized by Mizuguchi et al.<sup>2</sup> indicates that the product is mono-*N*-alkylated.



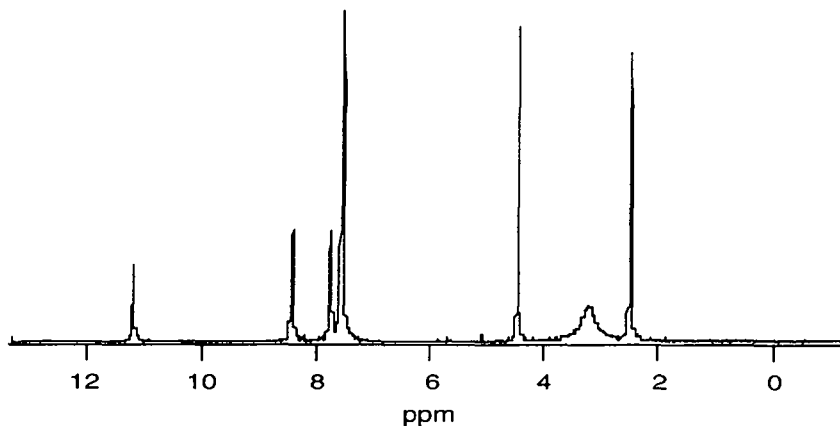


Fig. 2.2: NMR spectrum of MCDPP.

### 2.1.2. Other chemicals

Solvents were Fluka puriss. and used without further purification unless otherwise stated in the text.

Triplet donors 1,8-diphenyl-1,3,5,7-octatetraene (DPO, Aldrich, HPLC grade) and 1,6-diphenyl-1,3,5-hexatriene (DPH), fluorenone, pyrene, anthracene, zinc-phthalocyanine were all puriss. from Fluka. 2,2,6,6-tetramethylpiperidine N-oxyl radical (TEMPO) was Fluka purum.

TiO<sub>2</sub> colloidal suspensions in ethanol were prepared according to the procedure described by Moser<sup>3</sup>. TiO<sub>2</sub> colloidal thin films were prepared according to the procedure described by Barbé<sup>4</sup>.

### 2.1.3. Evaporated layers

The evaporator used for the organic layers is a in-house modified apparatus based on a 30 cm diameter evaporation chamber from Edwards. The pump system is an oil diffusion pump and a rotary pump (both Balzers). Background pressure was  $2 \cdot 10^{-6}$  to  $5 \cdot 10^{-6}$  mbar. The distance from the evaporation source (molybdenum, Balzers) to the samples was 7 cm. The layer thickness and evaporation rate were controlled using a Baltech QSG60 swing quartz thickness monitor and a manual heating control. Final layer thickness were measured on a Tencor Instruments alpha step 200. Thickness of 200 nm or less were measured by the absorption of the layers.

Au layers were evaporated in a Edwards Auto 306 evaporator at a background pressure of  $10^{-6}$  mbar. The samples had to be exposed to air for the transfer between the evaporators.

## 2.2. Experimental setups

### 2.2.1. Laser flash photolysis

Time-resolved absorption measurements were carried out using a Nd:YAG-laser for 532 nm excitation or a ruby laser for 347 nm excitation. Both lasers have a pulsewidth of 15 ns. For excitation wavelengths other than 532 nm or 347 nm a Nd:YAG 355 nm pumped OPO system was used allowing to choose the excitation wavelength continuously between 420 nm and 690 nm. The pulsewidth of this system is 7 ns.

The analyzing beam produced by the Xe arc lamp (Osram XBO, 450W) had a light power output of  $100\text{mW}/\text{cm}^2$ . The analyzing beam power could be increased by a factor of 10 during 2 ms for the acquisition of short ( $< 10\ \mu\text{s}$ ) transient signals. The detection wavelength was selected by a Bausch & Lomb F-33-005 monochromator and the signal was then detected by a photomultiplier tube (Hamamatsu R928) using only 3 dynodes with a total voltage of 750 V. The digital oscilloscopes are Tektronix DSA 602A or Tektronix TDS 524A. The two digital oscilloscopes were used interchangeably. Both allow a digitizing frequency of 1 GHz in continuous acquisition. The data were subsequently treated on a Apple Macintosh computer using the IGOR data analysis and presentation software.

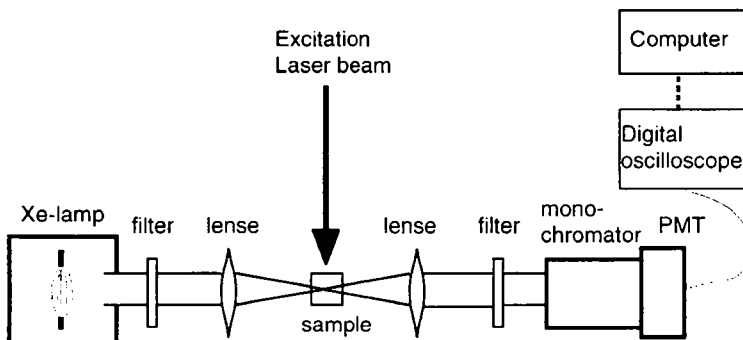


Fig. 2.3: Laser flash photolysis set-up

### 2.2.2. Fluorescence lifetime measurements

The fluorescence lifetimes were measured recording the transient fluorescence signal. The excitation laser (JK AML Nd:YAG) has a pulsewidth of 180 ps at 355 nm or 532 nm. The fluorescence was detected by a fast photodiode (Motorola MRD550) on a 90 V reverse bias. The signal was recorded by a Tektronix digital oscilloscope (TDS 524) in a repeated signal acquisition mode. Data were subsequently analyzed on an Apple Macintosh computer.

### 2.2.3. Absorption and fluorescence spectra

Absorption spectra were recorded on a HP 8450 diode array spectrophotometer or a Varian Cary 5 spectrophotometer. The two setups were used interchangeably. The fluorescence spectra were recorded on a SPEX Fluorolog fluorimeter, using a Xe-lamp source and a single monochromator for the excitation and a double monochromator and a single photon counting setup for the detection side. Fluorescence spectra of PVC films and evaporated layers were recorded in a front face geometry. The spectra from solution samples were recorded in a right angle geometry.

### 2.2.4. Solar cell characterization

The solar cells were characterized for their current-voltage (I-V) characteristics and their IPCE spectra. IPCE (incident photon to current conversion efficiency) is an uncorrected quantum yield of charge injection for monochromatic light.

$$\text{IPCE}(\lambda) = \frac{n_{\text{electrons}}(\lambda)}{n_{\text{photons}}(\lambda)} = \frac{I(\lambda) h c}{P_{\text{in}}(\lambda) e \lambda} \quad (2.1)$$

Corrections for surface- and interface reflection losses are neglected. IPCE has become a standard value for cell performance comparisons in spite of the missing corrections.

The light source for white light characterization was a 450W Xe-lamp with a 400 nm UV cutoff filter and a 5 cm water filter to remove the IR part of the spectrum<sup>5</sup>. For low currents of the solid state samples the potential was controlled by a potentiostat from EG&G Princeton Applied Research, model 362 and an Oriol monochromator model 77250 was used for monochromatic light. For higher currents of the photoelectrochemical cells a fully automated system was used. The system has been described by von Planta<sup>6</sup>. The system is based on Xe-lamp and a bandpass filter to cut the UV and IR parts of the spectrum. The spectrum is close to AM1.5 and for

$\text{RuL}_2(\text{SCN}^-)_2$ , L=dicarboxy bipyridine, as sensitizers, mismatch factors of 0.98 were obtained.

### 2.2.5. Cyclic voltammetry

Cyclic voltammetry was performed with a scanning potentiostat from EG&G Princeton Applied Research, model 362. The working electrode was a glassy carbon electrode with  $0.3 \text{ cm}^2$  surface area. Solvents were degassed with Ar for at least 15 min.

### 2.2.6. Time of Flight measurements

Transient current and time-of-flight measurements were done with a shunt-resistor current measurement setup.

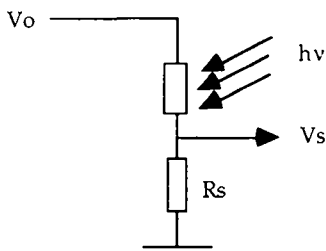


Fig. 2.4: Schematic setup for the transient current and time-of-flight measurements. The shunt resistor was varied between  $50 \Omega$  and  $100 \text{ k}\Omega$ . The time response for  $50 \Omega$  was 70ns FWHM for thick samples with low capacity.

The voltages applied were supplied by a DC 0-30 V voltage source (Weir). The data acquisition was done with a Tektronix DSA 602A or Tektronix TDS 524 digitizing oscilloscope.

### 2.2.7. Surface photovoltage spectroscopy (SPV/SPS)

SPS were recorded using a Kelvin probe controller S from Besocke Delta Phi and a Macintosh computer system for the data acquisition. The probe was a gold grid, allowing irradiation of the sample through the probe. The light source was a 450W Xe-lamp and a Bausch&Lomb monochromator mod. 33-86-79 with a 300 nm blaze. Slit width was 3 mm corresponding to a bandwidth of 30 nm. Cut-off filters were used to cut second harmonic wavelengths during large wavelengths spans. The light intensity was not corrected for the variation of the Xe-lamp intensity and the monochromator response over the spectrum.

### 2.2.8. Computational methods

For the molecular orbital calculations the Tektronix CAChe system was employed. CAChe (Computer Aided Chemistry) is a Macintosh based soft- and hardware package providing a convenient Macintosh-like user interface with many graphic facilities. The system is designed by Oxford Molecular and provided by Tektronix. CAChe allows to generate input files and present the results for the following programs:

- Molecular Mechanics
- Extended Hückel
- ZINDO
- MOPAC

The semiempirical computational methods available from ZINDO and MOPAC will be further described where they will be used.

## 2.3. References

- (1) Mizuguchi, J.; Homma, S. *J. Appl. Phys.* **1989**, *66*, 3104.
- (2) Mizuguchi, J.; Wooden, G. *Ber. Bunsenges. Phys. Chem.* **1991**, *95*, 1264-1274.
- (3) Nazeeruddin, M. K.; Liska, P.; Moser, J.; Vlachopoulos, N.; Grätzel, M. *Helv. Ch. Acta* **1990**, *73*, 1788-1803.
- (4) Barbé, C.; Arendse, F.; Comte, P.; Jirousek, M.; Lenzmann, F.; Shklover, V.; Grätzel, M. "Nanocrystalline TiO<sub>2</sub> electrodes for photovoltaic applications," accepted for publication in *J. Am. Cer. Soc.* 1997.
- (5) Braun, A. M.; Maurette, M.-T.; Oliveros, E. *Technologie Photochimique*; Presses Polytechniques Romandes: Lausanne, 1986.
- (6) Planta, C. V. Thesis No. 1537, EPFL, 1996.

# 3. Pigment surface

## 3.1. Introduction

DPP and its derivatives are used in commercial applications in pigment form<sup>1</sup>. The molecule had shown an insufficient stability in solution, but as a pigment it has proven very high thermal and photochemical stability<sup>2</sup>. In commercial applications mainly the para-chloro-phenyl analog of DPP, PCD, is used as a pigment in a polymer matrix.

The pigments of PCD are highly insoluble in most organic solvents and can be prepared in different particle sizes. Although the absorption properties have been discussed by various authors<sup>3-</sup>

<sup>8</sup> up to now little information exists on the emission properties of the solid crystalline state of these molecules. Emission studies provide a sensitive tool to probe and understand the surface versus bulk behavior of these materials.

In the following measurements of PCD particles in a PVC matrix and suspensions in a PVC solvent equivalent, tri-chloro-propane, or in acetonitrile are studied. Pigments in PVC matrices show the presence of surface adsorbed monomeric fluorescers.

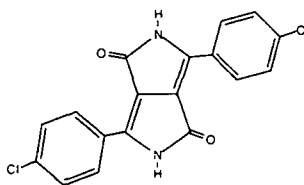


Fig. 3.1: PCD

## 3.2. Sample preparation

The crystallinity, size and morphology of dye pigments have a large effect on the color strength, shade chroma and light- and weatherfastness of the product<sup>1</sup>. The formation and growth of DPP pigment particles can be controlled, in particular, by *in situ* chemical methods both during and after the pigment formation step. Besides the control of morphology of a pure product, mixed synthesis methods may be used to control the crystallization behavior during the pigment particle formation. Low percentages of asymmetric m-cyano-PCD are frequently used for the particle size control.



Fig. 3.2: Scanning electron micrograph of PCD particles (sample A).

PCD pigments used in this study were prepared by ball milling or by precipitation from different solvents under different conditions method. The large PCD crystallites (samples A) used in the following have an average size of 400 nm and a specific surface area of  $24 \text{ m}^2/\text{g}$ . The density of the material is  $1.62 \text{ g}/\text{cm}^3$ . They are produced by controlled crystallization from isopropanol. This solvent allows high concentrations of the solute due to its ability to form hydrogen bonds with DPP<sup>5</sup>. The so produced particles are non-spheric. The morphology allows to conclude that the particles are at least partially crystallized as shown by electron microscopy (fig. 3.2). Small PCD particles (samples B and C) were obtained from precipitation of a mixture of 370 ml MeOH/100 ml H<sub>2</sub>O and 49g H<sub>2</sub>SO<sub>4</sub>. This yielded an average particle size of 30 nm. The particles were treated by ball-milling for 6 hrs

with sodium chloride in diacetyl alcohol or diethylene glycol as a solvent (samples C).

The PVC film contained 0.02% wt of the pigments and were prepared from the polymer/pigment mixture by a first calendering (passing between heavy cylinders) at 170°C and second pass at room temperature.

Irradiation experiments were carried out using a weatherometer (Atlas WSR, C165, C156A) which was equipped with a 6.5 kW Xenon B irradiation source. A borosilicate filter was used to cut-off the UV. The irradiation was carried out in a 4 hr cycle of 160 min. light, 20 min. light + water spray, 40 min. dark and 20 min. light + water spray.

Trichloropropane was received from Fluka. In order to remove any impurities that could solubilize PCD it was distilled at 41°C in a Fisher distillation column corresponding to 90 plateaus and using a 50% reflux.

### **3.3. Results and discussion**

#### **3.3.1. Absorption spectra**

The absorption spectrum of the PVC film containing PCD is given in fig. 3.3. A further evidence for the crystallinity of the pigment particles is given by the comparison of the absorption spectra of evaporated PCD layers before and after vapor treatment. Vapor treatment is known to lower activation energies for the crystallization process by partially solvating individual molecules and rendering them mobile within the bulk<sup>9-12</sup>. This facilitates crystallization and phase change at room temperature.



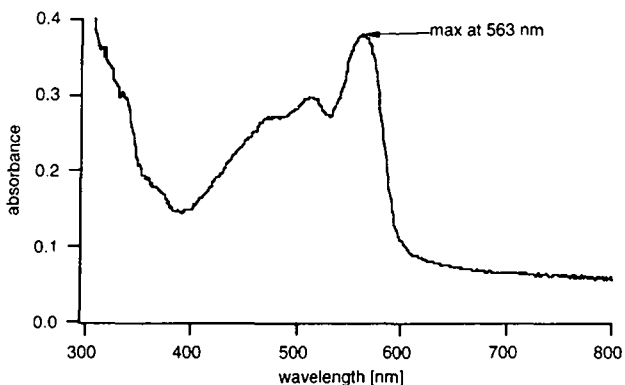


Fig. 3.3: absorption spectrum of PCD (A) in PVC film containing 0.02% PCD, recorded using an integrating sphere

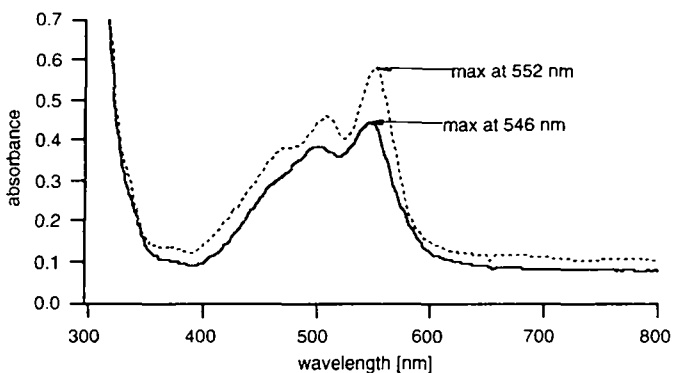


Fig. 3.4: PCD evaporated on a glass substrate under vacuum. The solid line shows the sample before vapor treatment. The dashed line shows the sample after exposure to acetone vapor for 30 minutes.

The absorption spectrum is clearly red shifted on going from the solution to the solid state and after the vapor treatment. In the solid state the spectrum is dependent on the size of the crystallites<sup>13</sup> yielding a larger red shift of the absorption spectrum for large particles. Since this shift is continuous with particle size, we do not expect a phase change to occur, as this has been shown in the case of Di-thioketo-DPP (DTPP)<sup>9</sup>.

### 3.3.2. Fluorescence spectra

The fluorescence spectra were recorded using a front face geometry for the PVC matrix samples and a right angle geometry for suspension samples.

DPP has in the solid state only a weak fluorescence compared to that of the monomer in solution. The fluorescence is heavily quenched due to the interactions with the neighboring molecules in the solid state leading to non-radiative decay.

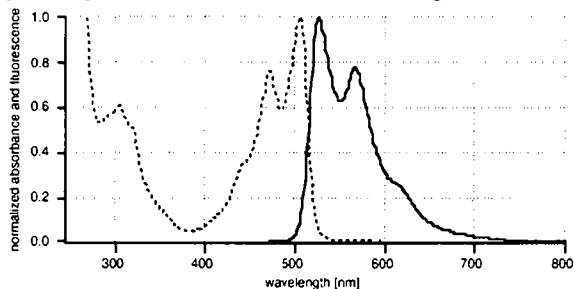


Fig. 3.5: Absorbance and fluorescence spectrum of PCD in DMSO solution.

The fluorescence spectrum of the pigments shows a new peak around 600 nm. A similar emission is present in the PVC matrix, the tri-chloro-propane suspension and on evaporated samples. In the PVC matrix the peak is observed at 590 to 605 nm depending on the preparation. In tri-chloro-propane it is observed at 580 nm. Finally the emission of evaporated samples has a very large spectrum with an ill-defined maximum at 620 nm. This shows that this fluorescence is strongly depending on the surrounding medium and on the preparation method. Fig. 3.6 shows the fluorescence of a standard PCD pigment and a more crystallized product. The degree of crystallization was determined by X-ray spectroscopy, where the more crystalline product showed 2 additional peaks. Both samples show the same fluorescence features. The differences in intensity are within the sample-to-sample variations generally observed. The degree of crystallinity of the pigments does not influence the fluorescence, suggesting that the emission is independent of the bulk crystallinity.

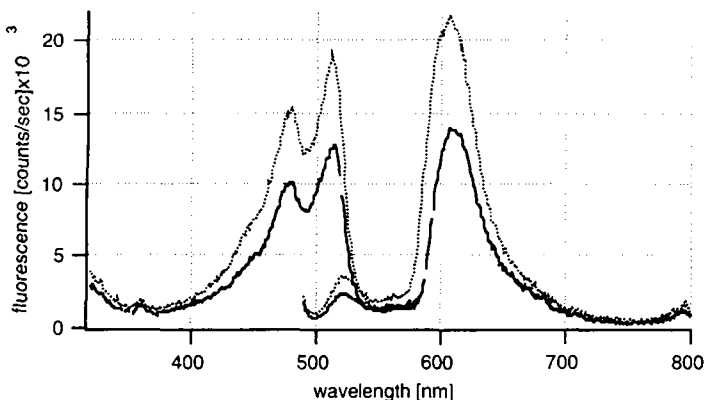


Fig. 3.6: Fluorescence emission and excitation spectra of large particles (A) in PVC matrix. For the emission spectrum the excitation is at 470 nm, for the excitation spectrum the emission is at 609 nm. The solid line presents the fluorescence of a standard industrial product, the dotted line presents the fluorescence of a more crystallized product.

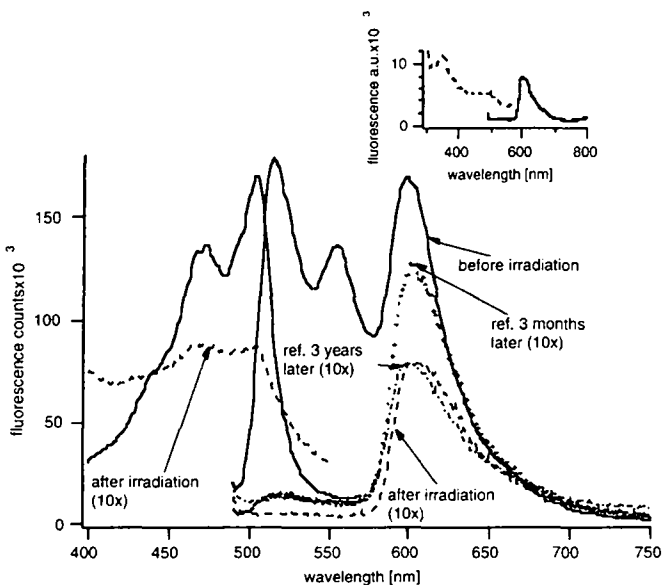


Fig. 3.7: Fluorescence emission and excitation spectra of fresh PCDB in PVC matrix. For the emission spectrum the excitation is at 470 nm, for the excitation spectrum the emission is at 600 nm. The solid line shows the spectra of freshly prepared particles, the dashed line shows the spectra after 200 hrs irradiation (measurement of fresh samples by V.J.P. Srivatsavoy). The inset shows the same sample after 3 years in dark.

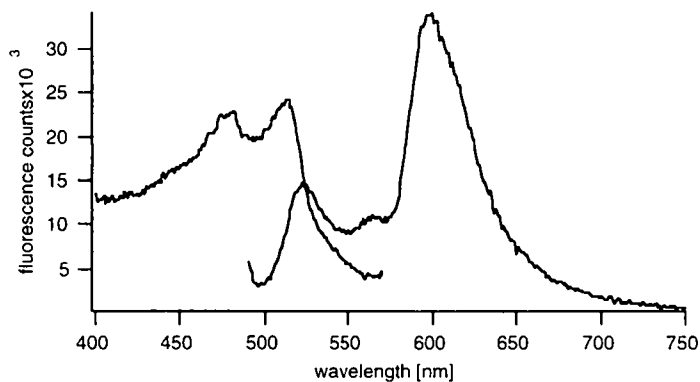


Fig. 3.8: Fluorescence emission and excitation spectra of ball-milled PCD (C) in PVC matrix. For the emission spectrum the excitation is at 470 nm, for the excitation spectrum the emission is at 600 nm (measurement by V.J.P. Srivatsavoy).

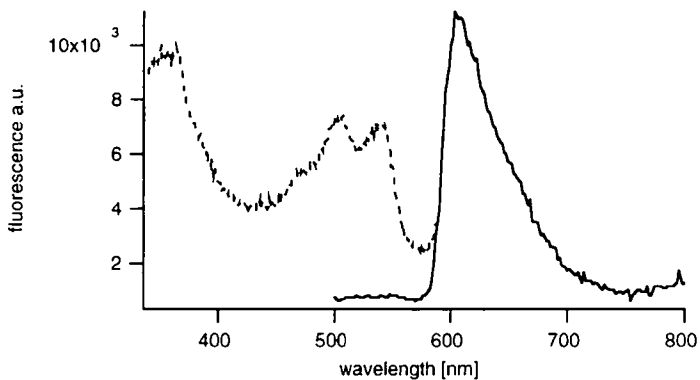


Fig. 3.9: Fluorescence emission and excitation spectra of PCD A2 in PVC matrix. For the emission spectrum the excitation is at 470 nm, for the excitation spectrum the emission is at 600 nm.

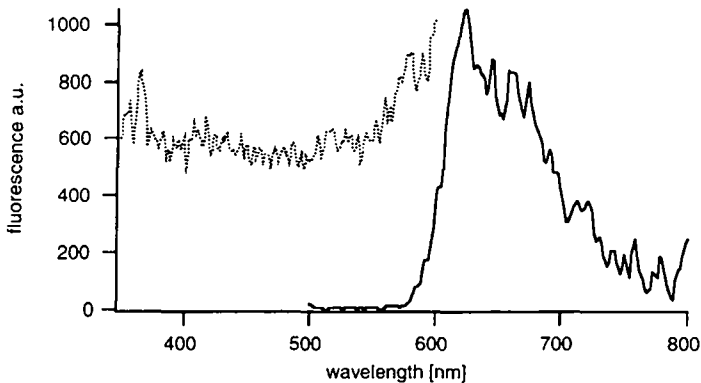


Fig. 3.10: Fluorescence of PCD evaporated layer, 300 nm thick. For the emission spectrum the excitation is at 470 nm, for the excitation spectrum the emission is at 600 nm.

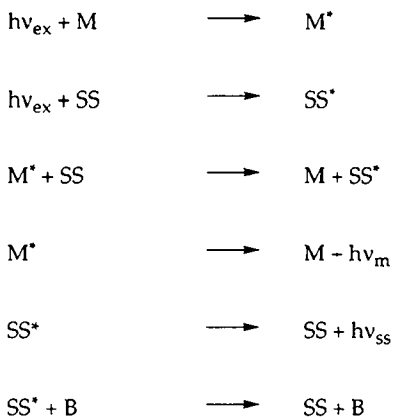
The emission source of the emission around 600 nm was investigated recording the excitation spectra. The excitation spectra do not follow the absorption spectra of the particles, neither in the PVC matrix nor in the tri-chloro-propane suspension. Excitation at the absorption maximum yields a much lower emission than excitation in the envelope of the monomer absorption around 420 to 500 nm.

On freshly prepared PVC films excitation at 470 nm yields an emission spectrum that may be decomposed into two contributions (fig. 3.7), one from the monomer emission at 515 nm and one from a secondary species emitting at 600 nm. The latter will be called surface species in the following.

Excitation at 540 nm outside the monomer absorption eliminates completely the contribution of the monomer emission in both the PVC matrix and tri-chloro-propane suspension, consistent with the attribution to monomers. This effect is more pronounced in the tri-chloro-propane suspensions, since the monomer contribution is higher in this case.

The excitation spectrum of the surface species emission at 600 nm has an important contribution corresponding to the monomer absorption spectrum. In the PVC films the monomer emission extending to 600 nm is not high enough to explain the excitation spectrum by a superposition of two independent fluorescence spectra. Moreover, some particles prepared by the industrial procedure (A) have a different excitation spectrum with a peak at 540 nm and no monomer fluorescence is observable (sample A2 in fig. 3.9). This excitation spectrum corresponds closely to the absorption spectrum of evaporated films but indicate even smaller crystallites due to the blue shifted absorption maximum. The evaporated films have been shown to be in a microcrystalline phase<sup>11</sup>, thus consisting of small particles or aggregates.

This leads to the interpretation below, that the surface species are identified as aggregates on the particle surface. On aged samples stored for 3 years at dark (inset of fig. 3.7) the excitation spectrum changes considerably, showing the loss of the prominent monomer absorption, but showing a higher plateau that can be interpreted as the superposition of spectra distributed over the spectral range of excitation. The emission however still shows a contribution of the monomer emission at 520 nm and the emission at 600 nm. The observations can tentatively be rationalized by a model involving both surface attached aggregates (surface species) and surface attached monomers acting as antennae:



where:

- M = monomer
- SS = Surface species
- B = Bulk
- $hv_{\text{ex}}$  = excitation photon energy
- $hv_{\text{m}}$  = monomer emission photon energy
- $hv_{\text{ss}}$  = surface species emission photon energy

The monomers transfer their energy to the surface species, thus their fluorescence is quenched. The residual monomer fluorescence observed is attributed to free monomers, that do not transfer their energy to an acceptor. They may be detached from the surface or be in a configuration where energy transfer is not efficient for geometric reasons, such as a weak orientation factor or a weak orbital overlap. In order to eliminate these free monomers PVC films were irradiated ( $\lambda > 350$  nm) during 200 hrs. Since the free monomers are expected to be the most photoreactive species due to their long (7 nsec. in solution) and unquenched lifetime

of the excited state, they are expected to photodegrade first. Indeed the irradiation resulted in an almost complete elimination of the monomer emission and the total emission of the surface species decreased by a factor of 10. Fig. 3.7 shows the corresponding emission spectra. However, the excitation spectrum still shows a feature of the monomer. This means, that there are still monomers absorbing the excitation light but their fluorescence is quenched. Several monomers may be attached to a surface aggregate acting as antennae. The emission at 600 nm is thus excited both directly and through energy transfer from the monomers apparently attached on the surface.

This observation could not be confirmed in tri-chloro-propane suspension. In this suspension the excitation spectrum of the surface species emission after irradiation does not show the features of the monomer around 500 nm (figure 3.11). Here the spectra can be well explained with the superposition of the monomer fluorescence and a surface species fluorescence. Since the monomers involved in the above mechanism are in this model pending on the surface, they are easily solubilized in the suspension, whereas they will remain on the surface of the particle in the polymer matrix due to the much lower diffusion constants.

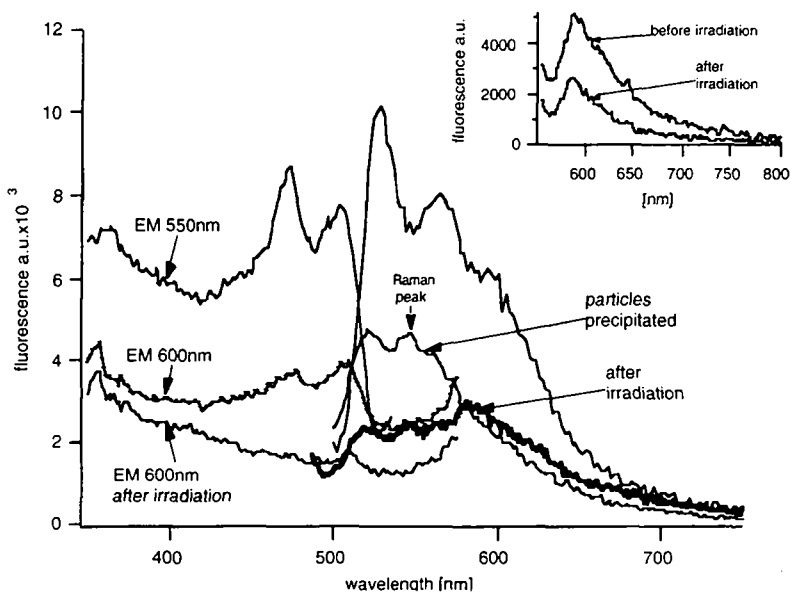


Fig. 3.11: Fluorescence of a suspension of PCD in trichloropropane. Excitation wavelength was 470 nm, emission wavelengths are indicated. The inset shows emission spectra obtained with 540 nm excitation. The irradiation was done with visible light during 10 hours with 2 suns intensity.

Chassot<sup>14</sup> claims that PCD is not soluble in acetonitrile. Particle suspensions in this solvent were used for the screening of stabilizers and irradiation of PCD-paint, containing PCD pigments in a melamine matrix, dipped in a closed vessel containing acetonitrile reduced the necessary time to produce a color change by at least two orders of magnitude. However fluorescence measurements show that PCD is not completely insoluble in acetonitrile. From the spectra in figure 3.12 it is seen that the observed monomer fluorescence remains after the particles had precipitated. The suspension showed no measurable absorbance of any residual particles after 3 days in the dark, when the particles had precipitated completely. The same observation was made in trichloropropane (fig. 3.11). There the sample was irradiated during 10 hours with a xenon lamp with an intensity of 1 sun. A UV filter was used to cut-off light below 350 nm. Immediately after the irradiation the monomer fluorescence had decreased by 50%. However, after several days in the dark the particles precipitated and molecules were dissolved during a slow process. Moreover, the fluorescence at 520 nm originating from monomers was efficiently quenched by oxygen. As will be shown in the next chapter in more detail, oxygen quenches the fluorescence of the monomers in solution with diffusion controlled rate, and in oxygen saturated solutions (1 atm) the fluorescence is quenched by up to 35% depending on the solvent properties. Saturating the acetonitrile suspension with oxygen at 1 atm selectively reduced the monomer fluorescence by 30%, indicating that the fluorescence is produced by free monomers with a lifetime corresponding to their radiative lifetime in solution. Energy transfer from the excited singlet state of DPP to oxygen is discussed in the next chapter below.

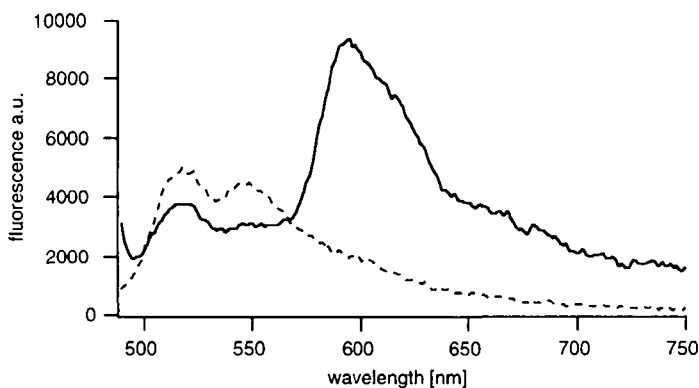


Fig. 3.12: Fluorescence of a suspension of PCD in acetonitrile. The solid line shows the fluorescence spectrum of a well dispersed suspension, the dashed line shows the fluorescence of the same sample several days later after the particles had precipitated.



Acetonitrile apparently solubilizes the molecules thus suggesting that the observed degradation proceeds through the monomers of PCD. This conclusion is still valid for the degradation of PCD in acetonitrile saturated paints<sup>14</sup>. Caution must therefore be taken during these stabilizer tests to control if the inhibited degradation process in acetonitrile exposed samples is as well the major degradation process in acetonitrile free samples.

The wavelength of the emission maximum,  $\lambda_{\max}$ , around 600 nm depends on the environment and the preparation. PVC films prepared at CIBA showed a variation of  $\lambda_{\max}$  between 590 and 605 nm depending on the preparation method of the films. In tri-chloropropane the emission even shifts to 580 nm. Since the preparations start from the same products, this is a clear evidence that the emission originates from a surface sensitive species and not from the bulk of the material.

The energy transfer is likely to happen by a Förster type or Dexter type energy transfer. The monomer fluorescence has a large overlap with the bulk absorption spectrum and with the absorption spectrum of very small aggregates such as they are observed in evaporated layers with an absorption maximum at 545 nm. Förster energy transfer would allow long distance energy transfer up to 50 Å, whereas Dexter type energy transfers involves electron exchange and thus is active only over small distances, allowing non-zero orbital overlap. The detailed geometry of the monomers and the surface species is not clear and thus conclusions about the distance of energy transfer are difficult. It is known from X-ray analysis<sup>8</sup> that PCD forms hydrogen bonded linear structures in the solid state. On the surface one therefore expects an interruption of these structures and molecules that are only partially integrated in the crystal matrix. These molecules are hydrogen bonded only on one side. They are therefore subject to less vibrational interaction than the molecules in the bulk and they are subject only partially to the hydrogen bonding induced bathochromic shift<sup>3</sup>. It is therefore reasonable to propose that the molecules on the surface produce the fluorescence. The molecules are then close to their neighbors, within the intermolecular distances of the crystal and a short distance energy transfer mechanism can not be excluded.

The fluorescence lifetime of the 600 nm emission was measured using a single photon counting setup. The measured decay signal could not be fitted with a single exponential fit. A good fit was obtained however using a double exponential fit exhibiting two components with lifetimes of 1 ns and 3.7 ns respectively. The signal may however be interpreted as being produced by the superposition of very different lifetimes. James and Ware<sup>15</sup> have shown, that many different lifetime distributions produce emission results that allow very good fitting with a double

exponential function. Considering the disorder on the surface taken as a basis for the proposed model the signal is indeed more likely produced by a superposition of fluorescers with different lifetimes. However, the fluorescers must have lifetimes in the order of 1 ns and 4 ns. These lifetimes are long considering the low fluorescence yield. They may be explained by the fact that the observed absorption of the films is mainly due to the bulk of the particles, and the fluorescing units only have a small absorption. Lacking the possibility to separate them, it is not possible to compute fluorescence quantum yields for these, but their yields may be assumed high consistent with the relatively long lifetimes.

### 3.4. Conclusion

PCD pigment particles have a characteristic emission around 600 nm. The corresponding excitation spectrum does not reflect the particle absorption spectrum in solid matrices, suggesting the existence of antennae like species on the surface of the particles transferring their energy to the emitting species. The excitation spectrum has a very good overlap with the absorption and excitation spectrum of the monomers in solution. In suspensions where the particles have very low solubility, monomers separate from the surface and are detected in the solvent after particle precipitation.

The presence of photophysically active monomers in both solid matrices and suspensions and the observed acceleration of degradation experiments<sup>14</sup> in solvent exposed samples allows the conclusion, that the photochemical degradation involves the monomers at least in an intermediate step.

As will be shown below,  $^1\Delta O_2$  is the major reactant for the degradation of DPP in solution. Considering the fact that HALS, the hydrogen equivalent to TEMPO, is not effective in PVC matrices whereas TEMPO is<sup>14</sup>, and that both are efficient radical interceptors but TEMPO is a more efficient singlet oxygen quencher, it may be expected that the degradation proceeds through the monomer and singlet oxygen.

### 3.5. References

- (1) Iqbal, A.; Cassar, L.; Rochat, A. C.; Pfenninger, J.; Wallquist, O. *Journal of Coatings Technology* **1988**, *60*, 37-45.
- (2) CIBA "internal report," Ciba, 1990.
- (3) Adachi, M.; Nakamura, S. *J. Phys. Chem.* **1994**, *98*, 1796-1801.
- (4) Mizuguchi, J. *Ber. Bunsenges. Phys. Chem.* **1993**, *97*, 684-701.
- (5) Mizuguchi, J. *Ber. Bunsenges. Phys. Chem.* **1994**, *98*, 28-34.
- (6) Mizuguchi, J.; Wooden, G. *Ber. Bunsenges. Phys. Chem.* **1991**, *95*, 1264-1274.
- (7) Mizuguchi, J.; Grubenmann, A.; Wooden, G.; Rihs, G. *Acta Crystallogr. Sect. B* **1992**, *b48*, 696-700.
- (8) Mizuguchi, J.; Grubenmann, A.; Rihs, G. *Acta Crystallogr. Sect. B* **1993**, *B49*, 1056-1060.
- (9) Mizuguchi, J.; Homma, S. *J. Appl. Phys.* **1989**, *66*, 3104.
- (10) Mizuguchi, J.; Rochat, A. C. *J. Imag. Sci.* **1988**, *32*, 135-140.
- (11) Mizuguchi, J.; Rihs, G. *Ber. Bunsenges. Phys. Chem.* **1992**, *96*, 597-606.
- (12) Gregg, B. A. *J. Phys. Chem.* **1996**, *100*, 852.
- (13) Srivatsavoy, V. J. P. "Size effect of DPP pigments on the absorption spectrum," EPFL-ICP2, manuscript in preparation.
- (14) Chassot, L. *Chimia* **1994**, *48*, 432-435.
- (15) James, D. R.; Ware, W. R. *Chem. Phys. Lett.* **1985**, *120*, 455-459.

# 4. Photophysics and photochemistry of the DPP monomers

## 4.1. Introduction

DPP and its derivatives are commercially applied in their solid state form as pigments in paints or as pigments in various polymer matrices. The molecules have a moderate stability in solution and photodegradation is efficient. But as a pigment the compounds exhibit a remarkable stability that has led to the commercial success of the class of pigments even. Despite that stability light induced color and shade changes are still observed and are a field of development. The discussion in the previous chapter has shown that the molecules at the surface of the particles possess long lifetime excited states, thus suggesting that the photochemical reactions leading to degradation happen mainly through the monomers on the surface. Progressing degradation will then expose new molecule layers as surface monomers. This model is supported by the observation that solvent dipping of paints and PVC samples increases the degradation by several orders of magnitude<sup>1</sup>. It has been shown that the degradation is inhibited by the exclusion of oxygen<sup>2</sup>, indicating that the degradation proceeds via an oxidation step. However it has not been clarified yet whether the oxidation proceeds mainly via singlet oxygen or the superoxide anion. The limited success of well known stabilizers such as ferrocenes and nitroxyls<sup>1,3,4</sup> raises this question as well.

The spectroscopic properties of the singlet ground state have been described by Mizuguchi et al.<sup>5-7</sup>. In the following the excited states and in particular the triplet state of the monomer will be investigated and their relevance for possible reaction mechanisms will be discussed.

## 4.2. Absorption and fluorescence

The absorption spectra of DPP and DM DPP were discussed by Mizuguchi<sup>5</sup>, yet little information has been published about the emission spectra of the monomers.

The fluorescence yields were measured using diphenyl anthracene as a standard. The fluorescence yields of DPP, DM DPP and DM ADPP (see chapter 2) were all unity within 5% error limit in degassed solutions.

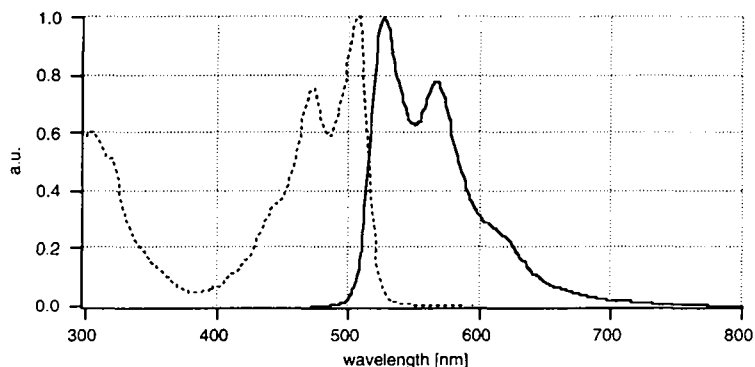


Fig. 4.1: excitation (dashed line) and emission spectra (solid line) of DPP  $10^{-6}$  mol  $l^{-1}$  in DMSO. Excitation wavelength was 450 nm, emission wavelength was 620 nm.

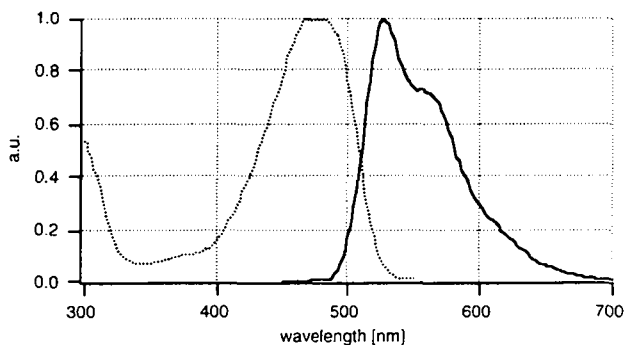


Fig. 4.2: excitation (dashed line) and emission spectra (solid line) of DM DPP  $10^{-6}$  mol  $l^{-1}$  in dioxane. Excitation wavelength was 450 nm, emission wavelength was 570 nm.

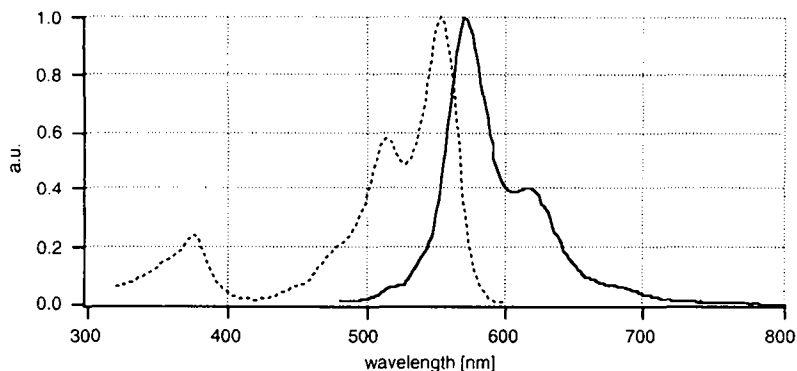


Fig. 4.3: excitation (dashed line) and emission spectra (solid line) of DMADPP  $5 \cdot 10^{-7}$  mol l<sup>-1</sup> in DMF. Excitation wavelength was 450 nm, emission wavelength was 620 nm.

The solutions of DPP in different solvents show a weak solvatochromic shift (table 4.1). This shows that the dipole moment of the excited state  $|\vec{\mu}_e|$  is of the same magnitude as the dipole moment of the ground state  $|\vec{\mu}_g|$ . For symmetry reasons the allowed states may not have a state dipole moment. The solvatochromic effect has been assigned to the hydrogen bonds formed between the solvent and DPP<sup>5,8</sup>. Intermolecular hydrogen bonding has been discussed in the solid state of DPP as the major reason for the bathochromic shift<sup>5,9</sup>.

solvent	$\lambda_{\max}$ (nm)	$E_T^R$ (kcal mol <sup>-1</sup> )	Dielectric constant
Dioxane	500	36	2.2
THF	501	37.4	7
DMF	504	43.8	36.7
DMSO	506	45	47
EtOH	500	51.9	24
NMP	507		32

Table 4.1: Absorption maxima of DPP in different solvents.  $E_T^R$  is the solvent polarity according to Reichardt's scale<sup>10</sup>. Dielectric constant data is compiled from references<sup>11,12</sup>.

#### 4.2.1. Radiative Lifetimes

The spontaneous emission lifetime of the radiative decay is determined by the coupling of the state  $n$  to state  $m$  according to the Einstein coefficient<sup>13</sup>  $A_{nm}$ :

$$\frac{1}{\tau_r^0} = k_r = A_{nm} = 2.881 \cdot 10^{-9} \nu_{nm}^2 n^2 A \quad (4.1)$$

where  $A$  is the integrated absorption coefficient.

For DPP's  $k_r$  can easily be measured by the observed fluorescence lifetime. Since in degassed solutions the fluorescence yield is unity within the precision of the measurement, we have

$$k_r = k_{obs} = \frac{1}{\tau_f} \quad (4.2)$$

The fluorescence decay time was measured by direct observation of the fluorescence kinetics using a fast diode detector and a 180 ps pulsewidth excitation at 355 nm or 532 nm (for DMADPP).

compound	solvent	conc. [mol/l]	$\tau_f$ [ $10^{-9}$ sec]	$\tau_r^0$ [ $10^{-9}$ sec]	$\tau_f / \tau_r^0$
DMADPP	DMF	$2 \cdot 10^{-6}$	4.3	3.4	1.26
DPP	DMF	$4 \cdot 10^{-6}$	7.1	5.4	1.31
DPP	DMSO	$5 \cdot 10^{-6}$	7.2	5.4	1.33
DMDPP	DMF	$4 \cdot 10^{-6}$	8.5	5.7	1.49

**Table 4.2:** fluorescence lifetimes of DPP and derivatives measured ( $\tau_f$ ) using the transient signal recorded from a diode detector.  $\tau_r^0$  calculated values were obtained from absorption spectra and equation 4.1.

The experimental lifetimes are all longer than the calculated values by 25 to 50%. The largest difference is observed for DMDPP. In this molecule the observed change in the vibrational structure from the excitation spectrum to the emission spectrum and the Stokes shift are large and the distortion of the phenyl rings out of the molecular plane is important due to steric reasons. The differences may therefore be attributed to changes between conformations of the ground to the excited state, i.e. a twisted excited state.

### 4.2.2. Transition dipole moment

The transition dipole moment describes the displacement vector of the charge density during the transition  $n \leftarrow m^*$ . The only change in charge density is the promotion of 1 electron from the ground state to the first excited state. In the case of DPP this is the LUMO  $\leftarrow$  HOMO transition. If  $\Psi_n$  and  $\Psi_m$  denote two different given by  $\Psi_i = \psi_i \cdot S_i \cdot N_i$ , where  $\psi_i$  is the electronic wavefunction,  $S_i$  is the spinfunction and  $N_i$  is the nuclear wavefunction, and  $q$  is the elementary charge, the transition dipole moment is then given by

$$\begin{aligned} \vec{\mu} &= q \cdot \vec{r} \\ \vec{\mu}_{nm} &= \langle \Psi_n | \vec{\mu} | \Psi_m \rangle \\ \vec{\mu}_{nm} &= \langle n | \vec{\mu} | m \rangle \langle S_n | S_m \rangle \langle N_n | N_m \rangle \end{aligned} \quad (4.3)$$

The INDO/S method allows to calculate the transition dipole moment of the transitions  $n \leftarrow m$ . This quantity is an upper limit for what may be expected from the experimental observations, since the spin overlap and nuclear overlap integrals are supposed to be unity due to the pure singlet character of the transition and the rigidity of the molecular structure during the calculation. Nevertheless, the direction of  $\vec{\mu}_{\text{LUMO} \leftarrow \text{HOMO}}$  is not affected by this approximations.

The present results were calculated with the INDO/S method. Details of the calculation method will be presented in chapter 4.5, where extensive use is made for the calculation of transition energies.

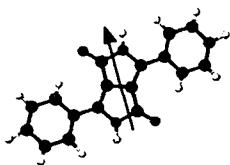


Fig. 4.4: Direction of the dipole moment found by Mizuguchi<sup>14</sup> using polarized reflection spectra on DPP single crystals.

$\vec{\mu}_{\text{LUMO} \leftarrow \text{HOMO}}$  has been measured by Mizuguchi<sup>15</sup> by reflection of single crystals. It has been calculated by Adachi<sup>9</sup> with the INDO/S method. The two results do not match. The present results of  $\vec{\mu}_{\text{LUMO} \leftarrow \text{HOMO}}$  direction confirm the calculations of Adachi<sup>9</sup>. The differences may be explained by the fact, that Mizuguchi had measured  $\vec{\mu}$  in a single crystal of DPP.

Hence the molecule is subject to the effect of the hydrogen bonds with its neighbors that changes the electron density on the nitrogen atoms according to Mizuguchi<sup>5</sup>. Moreover, Mizuguchi's measurements determine only the direction of the projection of the transition dipole moment into

\* General convention in spectroscopy: the upper state is noted on the left, the lower state on the right. The direction of the arrow indicates the transition (left: excitation, right: deactivation)



the plane given by the crystallographic axes  $a$  and  $b$  due to the measurement technique based on the reflection of the (001) face. The difference between the transition dipole directions is its component on the  $c$  axis. The result of Mizuguchi must therefore be interpreted as the direction of the projection of the transition dipole moment on the plane ( $a,b$ ). In this sense it agrees with the direction predicted by Adachi and the present results.

The directions of the transition dipole moments calculated for the 3 different molecules below differ only by small amounts. They are all in the planes of the molecules. The direction of  $\vec{\mu}$  of DMA differs slightly from the directions calculated for DPP and DMDPP. It reflects the differences found in the shapes of the HOMO presented in chapter 4.5.

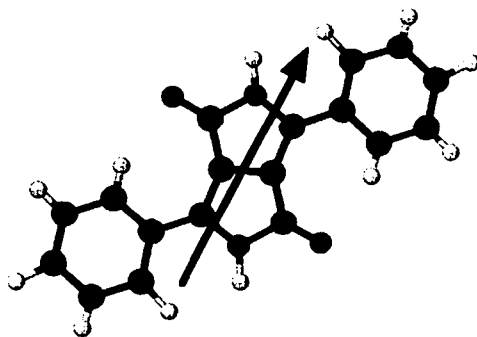


**Fig. 4.5:** Direction of the transition dipole moment of DPP calculated using the INDO/S method. The oscillator strength is 0.9802.

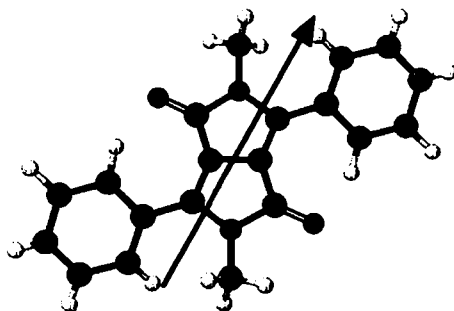


Fig. 4.6: Direction of the transition dipole moment of DMDPP calculated using the INDO/S method. The oscillator strength is 0.8658.

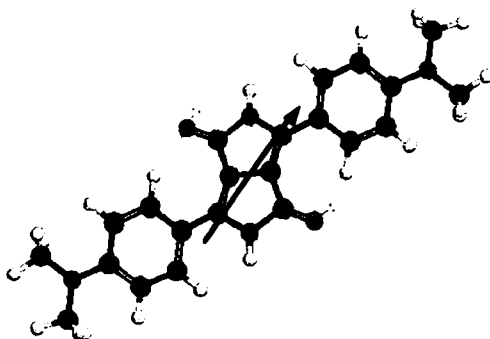


Fig. 4.7: Direction of the transition dipole moment of DMADPP calculated using the INDO/S method. The oscillator strength is 1.1957.

### 4.3. Reactions with singlet oxygen

The involvement of oxygen in the photodegradation reactions of DPP is obvious from previous experiments in solutions and suspensions<sup>2</sup>. However the reaction pathways were not clarified and in particular the role of singlet oxygen was not investigated. In the following the involvement of singlet oxygen will be investigated.

#### 4.3.1. Experimental

The influence of singlet oxygen  $^1\Delta\text{O}_2$  on the degradation of the molecular DPP was investigated by the observation of degradation kinetics. Di-Methyl-DPP (DMDPP) was chosen as a model compound for these studies, since it is much more soluble in different solvents and side effects of solubility limitations such as precipitation due to salt addition could be avoided.

DMDPP concentrations were monitored by measuring the absorbance of the solution. Singlet oxygen was produced by sensitization by well known singlet oxygen sensitizers absorbing light out of the absorbance range of DMDPP. The following constraints needed to be met simultaneously for the sensitizers:

- high quantum yield for generation of  $^1\Delta\text{O}_2$  to exclude side reactions
- triplet energy between the energy of singlet oxygen ( $94.5 \text{ kJ mol}^{-1}$ ) and the triplet energy of DPP ( $120 \text{ kJ mol}^{-1}$ , see chapter 4.4 ) to exclude efficient triplet energy transfer to DMDPP
- high absorption at  $\lambda > 600 \text{ nm}$
- high stability for the time spans of the experiments to maintain a constant singlet oxygen sensitization yield

Sensitizer	$\Phi(\text{isc})$	$\Phi(^1\Delta\text{O}_2)$	$E_{\text{Triplet}}$ [kJ mol <sup>-1</sup> ]	$\tau_{\text{Triplet}}$ [μs]	$\lambda_{\text{max}}$ [nm]	$\epsilon$ [l mol <sup>-1</sup> cm <sup>-1</sup> ]
Tetraphenylporphyrine (TPP)	0.82	0.65	137	1380	548	7400
Zinc(II)-phthalocyanine (ZnPc)	0.65	0.5	109	270	672	281800
Erythrosine	0.83	0.69	184	630	530	131800

Table 4.3: Photophysical data of singlet oxygen sensitizers. Data are compiled from refs <sup>12,16</sup>.

To quench singlet oxygen sodium azide ( $\text{NaN}_3$ ) and diazobicyclooctane (DABCO) were used. Benzoquinone (BQ) was used as a superoxide quencher.

Solutions of DMDPP and the singlet oxygen sensitizer S were prepared in dioxane,  $\text{CCl}_4$  and DMSO (all Fluka puriss.) without further purification. The samples were deaerated or oxygen saturated by bubbling the gas through the solutions for at least 10 minutes.

The samples were irradiated by a Xenon arc lamp of 450W yielding *ca.* 1 sun intensity. 570 nm cutoff filters were used to cover the spectral range where DMDPP is absorbing. The light intensity in the wavelength range where the sensitizer is absorbing was measured with a pyranometer using different filters covering partially the wavelength range of interest. Measurements with filters of different cutoff wavelengths allowed to estimate the intensity per wavelength window. This measurement showed that the light intensity is constant between 550 and 700 nm. The light intensity was  $8\text{W}/\text{m}^2 \cdot \text{nm}$ .

#### 4.3.2. Results and discussion

##### 4.3.2.1. Singlet oxygen yield of DPP and DMDPP in solution

The singlet oxygen yield in solution of two compounds has been measured by Olivieros and Braun using the continuous irradiation method for the production and detection of  $^1\Delta\text{O}_2$ . The production of  $^1\Delta\text{O}_2$  was monitored through detection of its luminescence at the near-IR wavelength of 1270 nm with a cooled Ge detector<sup>17,18</sup>. The reference used was fluorenone and the assumption was made, that the singlet oxygen yield of fluorenone<sup>19</sup> in dioxane is the same as in benzene,  $\Phi_{^1\Delta\text{O}_2} = 0.85$ . The solutions were in equilibrium with air, and thus the oxygen concentration is assumed as 21% of that in dioxane at an oxygen pressure of 1 atm which is  $6.2 \text{ E-}3 \text{ mol/l}$ .

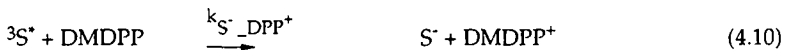
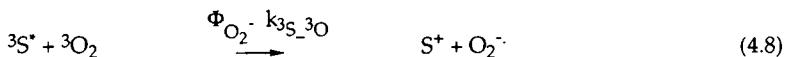
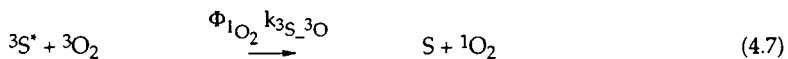
compound	$\Phi_{^1\Delta\text{O}_2}$	
	$\lambda_{\text{exc.}} = 308\text{nm}$	$\lambda_{\text{exc.}} = 437\text{nm}$
DPP	0.17	0.16
DMDPP	0.14	0.16

Table 4.4: singlet oxygen yield of DPP and DMDPP in solution. The solvent was dioxane.

These yields are high considering the low triplet yield of the compounds if the commonly supposed process<sup>18</sup> of eq. 4.29 is considered. They can however be well explained, if the reactions of eq. 4.30 and eq. 4.29 are both considered. A similar reaction scheme has recently been proposed for anthracene by Olea and Wilkinson<sup>20</sup>.

4.3.2.2. *Kinetic model and degradation rates in different solvents*

The reactions considered in the experiments are:



Under steady state conditions follows from these reactions that the concentration of the sensitizer triplet is given by

$$[{}^3S^*] = \frac{\Phi_{3S} \cdot \left(\frac{dn_{ph}}{dt}\right)}{\left(k_{3S\_3O} \cdot [{}^3O_2] + k_{3S\_3DPP} \cdot [{}^1DPP] + k_{3S}\right) \cdot N_{AV} \cdot V} \quad (4.15)$$

and the singlet oxygen concentration by

$$[{}^1O_2] = \frac{\Phi_{1O_2} \cdot k_{3S\_3O} \cdot [{}^3S] \cdot [{}^3O_2]}{\left(k_{1O_2\_DPP} \cdot [{}^1DPP] + k_{1O_2} + k_{1O_2\_Q} [Q]\right)} \quad (4.16)$$

combining these gives for the singlet oxygen concentration:

$$[{}^1O_2] = \frac{\Phi_{1O_2} \cdot k_{3S\_3O} \cdot \frac{\Phi_{3S} \cdot \left(\frac{dn_{ph}}{dt}\right)}{\left(k_{3S\_3O} \cdot [{}^3O_2] + k_{3S\_3DPP} \cdot [{}^1DPP] + k_{3S}\right) \cdot N_{AV} \cdot V} \cdot [{}^3O_2]}{\left(k_{1O_2\_DPP} \cdot [{}^1DPP] + k_{1O_2} + k_{1O_2\_Q} [Q]\right)} \quad (4.17)$$

and for oxygen concentrations such that  $k^{3S\_3O} \cdot [{}^3O_2] \gg k^{3S\_3DPP} \cdot [{}^1DPP] + k^{3S}$

$$[{}^1O_2] = \frac{\Phi_{1O_2} \cdot \Phi_{3S} \cdot \left(\frac{dn_{ph}}{dt}\right)}{\left(k_{1O_2\_DPP} \cdot [{}^1DPP] + k_{1O_2} + k_{1O_2\_Q} [Q]\right) \cdot N_{AV} \cdot V} \quad (4.18)$$

Thus the  ${}^1O_2$  concentration becomes independent of the oxygen concentration. Indeed in the experiment the degradation rate is found to be quasi independent of the oxygen concentration for oxygen concentrations of  $1.3 \cdot 10^{-3} \text{ mol l}^{-1}$ , i.e. in equilibrium with air. Figure 4.8 shows the degradation rates of DMDPP in dioxane where singlet oxygen was sensitized by TPP.

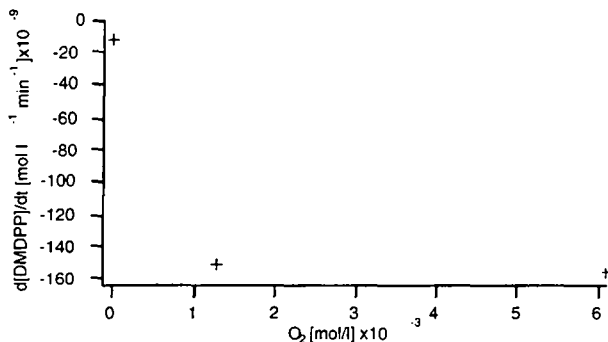


Fig. 4.8: Variation of the degradation yield as a function of the oxygen concentration. The points show degradation yields of Ar-bubbled, aerated and oxygen saturated samples of DMDPP in dioxane and TPP as singlet oxygen sensitizer.

The result presented in figure 4.8 allows to exclude the reaction of  $^1S^*$  with either oxygen or DMDPP, in particular reaction 4.6. This reaction with  $S = DPP$  is relevant in the case of singlet oxygen sensitization by DPP, but it is obviously not relevant for  $S = TPP$ , and thus confirms the standard mechanism proposed for singlet oxygen sensitization<sup>18,19,21-25</sup> which is reaction 4.7. This is generally justified by the high triplet yield, the short lifetime of the singlet excited state and the low energy splitting between the first singlet and triplet excited state of visible light absorbing singlet oxygen sensitizers.

Using the same hypothesis as above,  $k_{3S_3O} \cdot [^3O_2] \gg k_{3S_3DPP} \cdot [^1DPP] + k_{3S}$ , all direct reactions between the sensitizer triplet and DMDPP can be neglected. The degradation rate of DMDPP is then described by the following equation:

$$\begin{aligned} \frac{d[DPP]}{dt} = & -\Phi_{1O_2-DPP} \frac{\Phi_{1O_2} \cdot \Phi_{3S} \cdot \left(\frac{dn_{ph}}{dt}\right) \cdot k_{1O_2-DPP} [DPP]}{\left(k_{1O_2-DPP} \cdot [DPP] + k_{1O_2} + k_{1O_2} Q \cdot [Q]\right) \cdot N_{AV} \cdot V} \\ & - \Phi_{O_2^- -DPP} \frac{\Phi_{O_2^-} \cdot \Phi_{3S} \cdot \left(\frac{dn_{ph}}{dt}\right) \cdot k_{O_2^- -DPP} [DPP]}{\left(k_{O_2^- -DPP} \cdot [DPP] + k_{O_2^-} + k_{O_2^-} Q \cdot [Q]\right) \cdot N_{AV} \cdot V} \end{aligned} \quad (4.19)$$

which may be simplified with the following assumptions:

$$k_{1O_2-DPP} = 3 \cdot 10^9 \text{ s}^{-1}$$

$$k_{1O_2} = 5 \cdot 10^4 \text{ s}^{-1}$$

$$k_{O_2^-} \cdot [DPP] = 9 \cdot 10^4 \text{ s}^{-1} \gg k_{O_2^-} \text{ in pure solvents}$$

$$k_{3DPP} = k_{3DPP-1DPP} = 10^4 \text{ s}^{-1}$$

$$[1DPP]_0 = 3 \cdot 10^{-5} \text{ mol/l}$$

and rewritten as

$$\frac{d[DPP]}{dt} = -c_1 \cdot \frac{k_{1O_2-DPP} [DPP]}{(k_{1O_2-DPP} \cdot [DPP] + k_{1O_2})} - c_2 \quad (4.20)$$

whereas  $c_1$  and  $c_2$  stand for the factors assumed constant during the experiment, they are obvious by comparison with equation 4.19. In order to estimate the importance of the decay constant of singlet oxygen compared to the reaction rate of singlet oxygen with DMDPP the singlet oxygen lifetimes were measured in the employed solvents.

Solvent	Sensitizer	$k_{1O_2}$ [s <sup>-1</sup> ]	$\tau_{1O_2}$ [μsec]
CD <sub>3</sub> OD	RB	$3.69 \cdot 10^3$	271
CH <sub>3</sub> OH	RB	$9.07 \cdot 10^4$	11
Dioxane	TPP	$3.62 \cdot 10^4$	27.6
DMA	TPP	$6.22 \cdot 10^4$	16.1
DMF	TPP	$4.70 \cdot 10^4$	21.2
DMSO	TPP	$1.34 \cdot 10^5$	7.4
D <sub>2</sub> O	RB	$1.61 \cdot 10^4$	62

**Table 4.5:** Singlet oxygen lifetimes and corresponding decay constants in various employed solvents measured by direct detection of the transient IR emission of  $^1\Delta_{O_2}$  in a laser flash photolysis experiment.  $\lambda_{ex} = 532 \text{ nm}$ . The abbreviations are: RB = Rose Bengal, TPP = Tetraphenylporphyrine, DMA = Dimethylacetamide, DMF = Dimethylformamide, DMSO = Dimethylsulfoxide.

Comparison of the lifetimes listed in table 4.5 to the reaction rate of singlet oxygen with DMDPP  $k_{1O_2-1DPP}[^1DPP] = 1.6 \cdot 10^5 \text{ s}^{-1}$  shows that also for the pure singlet oxygen induced degradation the kinetics are neither pure first order nor pure zero order. However in solvents where  $k_{1O_2}$  is small quasi zero order kinetics are expected, whereas in solvent where  $k_{1O_2}$  is large a deviation from zero order is expected.



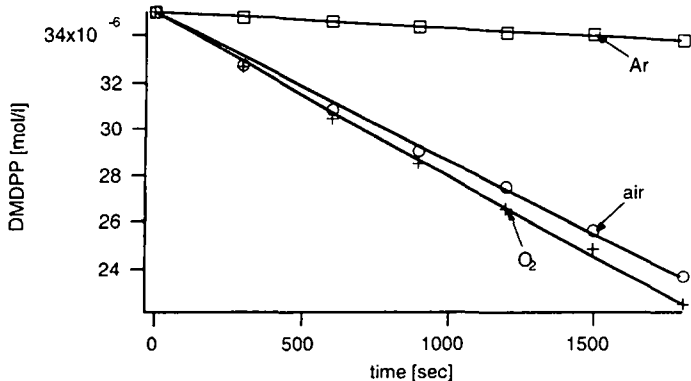


Fig. 4.9. a: Kinetics of the degradation of DMDPP in dioxane sensitized by tetraphenyl porphyrine (TPP) at different oxygen concentrations. The initial concentration of DMDPP was  $3.5 \cdot 10^{-5}$  mol/l.

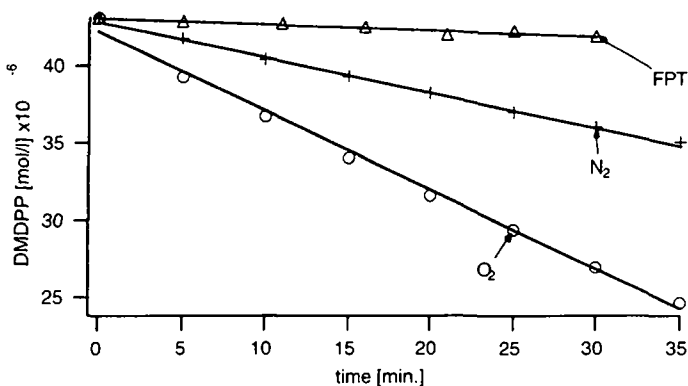


Fig. 4.9. b: Degradation of DMDPP in  $\text{CCl}_4$ . Singlet oxygen was sensitized by TPP.

The degradation experiments were conducted over *ca.* 30 minutes for each sample. The plots obtained for the DMDPP concentration decrease in dioxane using TPP as a singlet oxygen sensitizer show a quasi zero order behavior (fig. 4.9. a). Deviations from zero order kinetics were observed with ZnPc. ZnPc is however not stable under the experimental conditions and substantially degrades during the timespan of the experiment, thus decreasing the absorbance and finally the singlet oxygen yield. For low DMDPP concentration below  $10^{-6}$  mol/l deviations were observed as well. They are in agreement with equation 4.20. In this case the decay of  $^1\Delta\text{O}_2$ ,  $k_{1\text{O}_2}$ , becomes significant and the kinetics are no longer pseudo zero-order.

In order to further establish the importance of singlet oxygen experiments were conducted in  $\text{CCl}_4$  (fig. 4.9. b). In this solvent lifetimes of  $^1\text{O}_2$  reported range from  $700 \pm 200 \mu\text{s}$ <sup>26</sup> up  $26000\text{-}31000\mu\text{s}$ <sup>25</sup> and the oxygen saturation pressure is as high as  $12.4 \cdot 10^{-3} \text{ mol/l}$ <sup>12</sup>. Also the triplet lifetime of the singlet oxygen sensitizer is expected to be long due to the weak vibrational coupling with a solvent characterized by low frequency vibration modes. Therefore the effect of triplet oxygen concentration independence of the degradation rate outlined above and shown in figure 4.8 for samples in dioxane is more pronounced in  $\text{CCl}_4$ . Indeed the degradation rate in  $\text{CCl}_4$  where oxygen was removed by bubbling nitrogen for more than 10 minutes decreased only by 50%, whereas in the FPT (freeze-pump-thaw) degassed solution the degradation rate decreased by more than 90%. This shows that the reactive species is long lived in  $\text{CCl}_4$  in accordance with its assignment to singlet oxygen. Direct reactions of  $\text{CCl}_4$  with excited species such as anthracene are known<sup>23</sup>. They may however be excluded in our case as a major degradation path due to the fact that the degradation rate decreases strongly in FPT degassed solutions.

#### 4.3.2.3. *Influence of singlet oxygen and superoxide quenchers*

Although the singlet oxygen sensitizers used have low yields for side reactions such as electron transfer to oxygen yielding superoxide anions, they can hardly be completely excluded. In order to scrutinize a particular reaction path specific quenchers can be added either to block the other remaining reactions or to block the reaction path of interest. For the distinction between singlet oxygen and superoxide anion as main reactive species, Braun et al.<sup>27</sup> have proposed furfuryl alcohol (FA) as a selective singlet oxygen quencher in water and benzoquinone (BQ) as a selective superoxide anion quencher. Indeed singlet oxygen is not quenched by BQ<sup>27,28</sup>. FA acts as a chemical quencher of singlet oxygen<sup>29,30</sup>. Diphenyl-iso-benzofurane (DPBF) is an efficient chemical quencher for singlet oxygen and widely used for the determination of singlet oxygen yields<sup>30-33</sup>. Another widely known singlet oxygen quencher is  $\beta$ -carotene<sup>26,34</sup>, which acts mainly as a physical quencher by energy transfer due to its low triplet state energy, but also reacts chemically according to our experience and vanishes from the solution during the experiment. Tetramethylpiperidine-N-oxyl (TEMPO) has been described as an efficient singlet oxygen quencher by Bellus<sup>34</sup>. It has been used for the stabilization of PCD (*p*-chloro-DPP) in PVC matrix and  $\text{CH}_3\text{CN}$  suspensions, but the mechanism of action has not yet been further investigated<sup>1</sup>. 1,4-diazabicyclo[2,2,2]octane (DABCO), although it is not a very efficient singlet oxygen quencher<sup>4</sup> ( $k_q = 2.4 \cdot 10^7 \text{ mol}^{-1} \text{ s}^{-1}$  average in different solvents), is used as a diagnostic agent for the participation of singlet oxygen in oxygenation reactions as well as a standard for the determination of

relative quenching efficiencies because it is a physical quencher and oxidatively stable. Its oxidation potential is 1.2 V vs SCE<sup>35</sup> and is therefore much less redox active than TEMPO, the redox potential of which is 0.6V vs SCE<sup>36</sup>. DABCO is therefore preferred as a diagnostic compound. Sodium azide is often used as a diagnostic for singlet oxygen involvement in oxidation reactions<sup>37-39</sup>. It has a high quenching efficiency ( $5 \cdot 10^8 \text{ mol}^{-1}\text{s}^{-1}$  in water<sup>37</sup>). It is however discussed in the literature whether it has a significant yield of superoxide as a result of the quenching reactions or not. Harbour and Issler<sup>39</sup> had found that at least 15% of the charge transfer complexes formed in the quenching reactions dissociate into free ions prior to recombination<sup>40</sup>. Haag and Mill<sup>37</sup> on the contrary found that more than 99.8% of the quenching events result in physical deactivation. Moreover  $\text{N}_3^-$  reacts itself with aromatic compounds and may thus lead to side reactions<sup>41,42</sup>.

In the present work DABCO was used as a singlet oxygen quencher and BQ as a superoxide quencher. These allow to selectively eliminate one or the other reaction path and thus to show their relevance for the observed photodegradation. Physical quenchers of singlet oxygen were preferred over chemical quenchers, since the observed degradation yield of DPP by singlet oxygen are well below the diffusion limit. The chemical quenchers therefore are consumed within a short period and steady state concentrations can not be assumed during the timespan of the experiments.

#### *Influence of DABCO*

The average singlet oxygen quenching rates for DABCO in different solvents reported are  $k_q = 2.4 \cdot 10^7 \text{ mol}^{-1} \text{ s}^{-1}$ . It was employed at  $2 \cdot 10^{-2} \text{ mol/l}$  concentration.

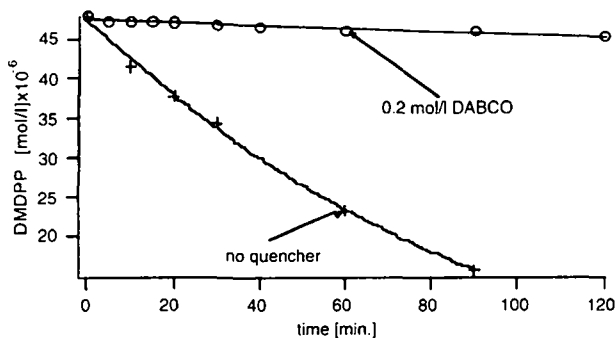


Fig. 4.11: Degradation quenching effect of  $0.2 \text{ mol l}^{-1}$  DABCO for DMDPP in dioxane. Singlet oxygen was sensitized by TPP.

Figure 4.11 shows that the degradation of DMDPP in dioxane solution is strongly inhibited by the addition of 0.5 mol/l of DABCO. In order to eliminate the hypothesis that the singlet oxygen quencher triplet TPP is directly quenched by DABCO, the triplet lifetime of TPP was measured using flash photolysis. The excitation wavelength was 532 nm from a NdYAG laser with 10 ns pulse width and the detection wavelength was 450 nm where  ${}^3\text{TPP}^*$  has a large absorption. In a dioxane solution degassed by nitrogen bubbling the triplet lifetime of TPP  $\tau_{\text{TTPP}}$  was 164  $\mu\text{sec}$ . This lifetime is a lower limit, since the kinetics exhibited some second order component from triplet-triplet annihilation. No significant change of the triplet lifetime was observed upon addition of 0.2 mol/l DABCO. The quenching efficiency of the TPP triplet by DABCO is therefore less than  $6 \cdot 10^3 \text{ mol}^{-1} \text{ l s}^{-1}$ . Direct quenching of the singlet oxygen sensitizer can therefore be excluded and the observed decrease of the degradation efficiency is due to the quenching of the singlet oxygen and not of its sensitizer.

This experiment allows to calculate the reaction rate constant for the reaction of DMDPP with  ${}^1\text{O}_2$ . Assuming a reaction constant of  $2.4 \cdot 10^7 \text{ mol}^{-1} \text{ s}^{-1}$  for the quenching of  ${}^1\text{O}_2$  by DABCO, and observing a decrease of degradation rate  $k_{\text{deg}}$  by a factor of  $\frac{k_{\text{deg}}^{\text{O}}}{k_{\text{deg}}} = 17$  upon addition of 0.2 mol/l DABCO to the solution we calculate

$$k_{\text{obs}}^{\text{O}} = \frac{k_{1\text{O}_2\text{-DPP}} [\text{DMDPP}]}{k_{1\text{O}_2\text{-DPP}} [\text{DMDPP}] + k_{\text{q}} [\text{DABCO}]} k_{\text{deg}}^{\text{O}}$$

$$\frac{1}{17} = \frac{k_{1\text{O}_2\text{-DPP}} [\text{DMDPP}]}{k_{1\text{O}_2\text{-DPP}} [\text{DMDPP}] + k_{\text{q}} [\text{DABCO}]}$$

$$k_{1\text{O}_2\text{-DPP}} = \frac{k_{\text{q}} [\text{DABCO}]}{16 \cdot [\text{DMDPP}]}$$

$$= 6 \cdot 10^9 \text{ mol}^{-1} \text{ s}^{-1}$$

This value is above the diffusion controlled limit for dioxane, which is according to the Smoluchowski formula  $4.5 \cdot 10^9 \text{ l mol}^{-1} \text{ s}^{-1}$ . Considering the error from the assumed quenching rate of DABCO for dioxane, that was interpolated from data in other solvents since no precise data were available for dioxane. It may be concluded that DMDPP reacts with  ${}^1\text{O}_2$  within diffusion the controlled limit.

Similar results were obtained using sodium azide ( $\text{NaN}_3$ ) as singlet oxygen quencher in DMSO solution. However, the quenching efficiency was less than

expected from the reported reaction rates of  $N_3^-$  in the literature. The observations can however be attributed to radical reactions of  $N_3^*$  radical<sup>39</sup> and extend the reactions under consideration.

#### *Influence of BQ*

Although TPP is assumed to have a negligible yield of superoxide, this reaction path can a priori not be completely excluded. BQ has been demonstrated to be a selective quencher for superoxide anions, not quenching the singlet oxygen<sup>27</sup>. BQ was employed with a concentration of  $10^{-2}$  mol/l in a solution in dioxane containing  $6.2 \cdot 10^{-5}$  mol/l DMDPP. The concentration was smaller than the concentration of DABCO in the previous experiment to maintain the product  $k_q \cdot [Q]$  constant. The reaction rate constant of BQ with the superoxide anion in water<sup>27</sup> is  $3 \cdot 10^8 - 7 \cdot 10^8$  l mol<sup>-1</sup> s<sup>-1</sup>

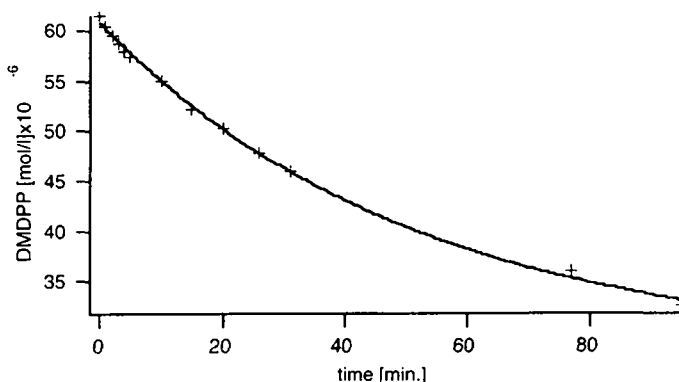


Fig. 4.12: Degradation of DMDPP in dioxane with  $10^{-2}$  mol l<sup>-1</sup> BQ.

The degradation is not inhibited by BQ as shown in figure 4.12. It may therefore be concluded that superoxide does not play a major role in the degradation of the monomer in solution.

#### 4.3.3. Discussion and Conclusion

From these experiments we conclude that the monomer is mainly degraded by singlet oxygen with a diffusion controlled rate. As shown below DPP is able to sensitize singlet oxygen even though it has a very low intrinsic triplet yield and a fluorescence yield of close to 100% in oxygen free solutions. The reported stabilization effect of TEMPO<sup>1</sup> is well explained by the singlet oxygen quenching

effect of this compound<sup>3,4</sup>. Moreover, the observed failure of HALS compounds<sup>1</sup> indicates that singlet oxygen is still the main responsible for the degradation of DPP pigments. HALS are known as polymer stabilizers, where their action is attributed to radical trapping<sup>4</sup>, rather than their singlet oxygen quenching effect, since their reaction rates for singlet oxygen deactivation is two orders of magnitude smaller than the corresponding rate for TEMPO, while the polymer stabilizing effects are comparable. In our case however, the difference in singlet oxygen quenching efficiency explains the differences observed in the stabilization effects.

The reactivity of DPP with singlet oxygen can be interpreted in the following way: The HOMO of DPP has a high electron density on the double bonds of the carbons of the pyrrolo-pyrrole structure, allowing the formation of dioxetanes<sup>22,25</sup> from singlet oxygen. The highly localized electron density of the frontier orbital distinguishes DPP from e.g. tetracarboxylic-diimide-perylene compounds (PTCDI), that exhibit a similar energy structure<sup>43</sup>. Although PTCDI have similar singlet and triplet energies, they are more stable. Preliminary Molecular orbital calculations showed, that the HOMO is highly delocalized on the perylene core, which rationalizes the difference of stability observed.

## 4.4. Triplet states

The triplet state plays an important role in photochemical reactions, particularly in the course of singlet oxygen sensitization, due to its generally long lifetime. In the triplet state of a molecule two electron spins are unpaired. Generally organic molecules need to be in an excited state to allow two or more unpaired spins. Triplet states are therefore longlived excited states and carry energy to initiate chemical reactions or to transfer to other molecules. This makes the triplet state important in photophysical reactions, including reactions that potentially lead to degradation<sup>44,45</sup> particularly if it interacts with oxygen<sup>24,46,47</sup>. For the DPP monomer the triplet state has not yet been investigated. Its involvement in the degradation mechanism is suggested by the observation of photoactive monomers in the pigment particle fluorescence. It has been shown that the degradation of the PCD pigment in a paint is increased by the addition of nitroxy radicals<sup>1</sup> which is known to trap radicals and to quench efficiently the singlet states<sup>48</sup> and to enhance the triplet states as well as to quench singlet oxygen<sup>3,4</sup>, but their interaction with DPP is not clear. In this chapter the role and the energetics of the triplet state will be discussed.

### 4.4.1. Theory and applied methods

The triplet state of a molecule is defined as the state with spin multiplicity of 3. The spin multiplicity is  $2 \cdot S + 1$ , thus  $S$  needs to be equal to 1. The spin of an electron is  $+\frac{1}{2}$  or  $-\frac{1}{2}$ , thus the triplet state is the electronic configuration in which two electron spins are unpaired. From Pauli's exclusion principle follows that these electrons need to be in different orbitals. In general the first triplet state  $T_1$  is therefore the first excited state of the molecule in which the spins of the two electrons in the highest orbitals are unpaired. In general the  $T_1$  state has a lower energy than the  $S_1$  state due to *spin correlation* or electron exchange effects. However, the transition from the singlet to the triplet manifold is in general spin forbidden and thus the  $T_1$  state is not easily accessed, neither by intersystem crossing  $S_1 \longrightarrow T_1$  nor the direct excitation  $T_1 \longleftarrow S_0$ , unless there exists a strong spin-orbit coupling. Since the transition  $T_1 \longrightarrow S_0$  is spin forbidden the radiative lifetime of  $T_1$  is long compared to the  $S_1$ .

To satisfy Pauli's principle the total electronic wave function must be antisymmetric. In the absence of spin-orbital coupling, the wavefunction can be written in the form of the product of a spatial wavefunction and a spin function. A full calculation illustrating the separation in a product for the case of a two electron system is given e.g. by Rivail<sup>49</sup>. In triplet states the spin function is symmetric, thus

forcing the spatial part of the wave function to be antisymmetric. This leads to nodes in the spatial part of the wavefunction and thus to a better spatial separation of the electronic charges. The reduced repulsion forces lead to an energy lowering compared to the corresponding singlet excited state. The energy lowering is therefore a consequence of Pauli's principle and is summarized by Hund's rule<sup>22,50</sup> of maximum multiplicity, saying that for a set of states with degenerate energy the configuration with maximum multiplicity lies lowest in energy.

Triplet states can be produced in several ways:

direct excitation of  $T_1 \leftarrow S_0$ : In organic molecules such as DPP this transition is spin-forbidden. This excitation may become less spin-forbidden by the action of the magnetic field induced by the electrons of the heavy atom. The magnetic field gives rise to a spin-orbit coupling term in the molecule and thus renders the  $T_1 \leftarrow S_0$  less forbidden<sup>23</sup>. Heavy atoms may be part of the molecule, of the solvent molecule or in micelles<sup>51</sup>.

intersystem crossing decay: If the transition  $S_1 \rightarrow T_1$  is rapid, the molecule may undergo spontaneous intersystem crossing yielding the triplet state. However in highly fluorescent molecules, such as DPP, this transition is slow compared to  $k_r$  from the singlet excited state and leads to negligible yield of  $T_1$ . Intersystem crossing may be enhanced by heavy atoms<sup>23,52</sup> or stable radicals<sup>48</sup> that allow the spin transition due to orbital mixing in a bimolecular reaction.

Triplet energy transfer:<sup>53</sup> the energy and the spin multiplicity from a higher energy triplet state from a donor molecule that itself undergoes rapid intersystem crossing will be transferred in a bimolecular reaction to the acceptor molecule. The total spin is preserved during the reaction.

DPP and its derivatives are organic molecules with no heavy atoms, thus the direct excitation of  $S_0 \rightarrow T_1$  is not expected to be efficient. The molecules have fluorescence yields of unity in degassed solutions. The intersystem crossing is therefore negligible compared to the radiative decay of  $S_1$ . The method of choice is therefore triplet energy transfer<sup>53,54</sup> or enhanced intersystem crossing by heavy atoms<sup>52</sup> or radicals<sup>48</sup>.

#### 4.4.1.1. *Triplet energy transfer*

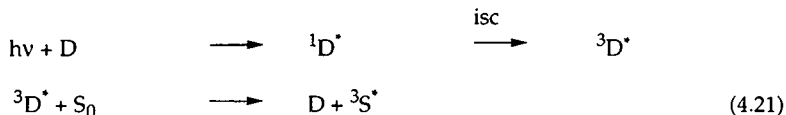
In this method of generating the triplet state, a donor molecule is needed that can be excited to its triplet state efficiently and yields an higher energy triplet state in order to ensure enough driving force for the triplet energy transfer. Higher energy



triplets may be produced by pulse radiolysis or by flash photolysis<sup>54</sup>. In this work all the triplets were excited by the flash photolysis method:

Flash Photolysis:

In a flash photolysis experiment the triplet donor molecule D is chosen to have a high intersystem crossing yield and to absorb in a wavelength region where absorption of the dye molecule S is weak to minimize direct excitation of S. <sup>3</sup>D is excited during the laser pulse and <sup>3</sup>S is then produced through the following reaction scheme:



Reaction 4.21 leads, under favorable energy conditions usually during a collision to 100% triplet energy transfer. Due to the long triplet lifetimes encountered in organic donor molecules, even a low concentration of S leads to quantitative quenching of <sup>3</sup>D. In the transient absorption experiment the absorption of <sup>3</sup>D and subsequently of <sup>3</sup>S can be monitored. The triplet lifetime is measured in a degassed solution, in order to avoid the quenching by O<sub>2</sub>.

Mechanism of the triplet energy transfer

The triplet transfer rate constant k<sub>q</sub> was shown to be independent of the oscillator strength T<sub>1</sub> ← S<sub>0</sub><sup>53,55</sup>. This supports that the mechanism of triplet energy transfer is not a dipole-dipole interaction but is based on electron exchange (Dexter type energy transfer<sup>56</sup>). It was confirmed by the measurement of the cross sections of the bimolecular rate constants that the transfer happens over short distances. The small cross sections obtained suggest a short range interaction mechanism<sup>23</sup>. Furthermore orbital interaction is needed to allow the otherwise spin-forbidden T<sub>1</sub> ← S<sub>0</sub> transition. Electron exchange occurs therefore only at short (<15Å<sup>23</sup>) distances as opposed to dipole-dipole (Förster type) energy transfer (< 50Å). The choice of the triplet donor D is thus independent of the absorption and emission spectra of D and A. Since the energy transfer mechanism is not dipole-dipole interaction, it is not dependent on the optical properties of the donor and acceptor molecules<sup>23</sup>, the choice of the triplet donors does therefore not depend on their emission spectra.

k<sub>q</sub> depends on the excess energy of the donor triplet (ΔE<sub>T</sub>) in the following way<sup>53</sup>:

$$k_q = \frac{d\left(\frac{d[{}^3D^*]}{dt}\right)}{d[A]} = \frac{1}{1 + \exp(-\Delta E_T/kT)}$$

$$\Delta E_T = E_T(D) - E_T(A)$$

Sandros pointed out the possibility of back energy transfer to the donor if the energy difference is small. This slows down the observed energy transfer rate since some of the quenched triplet states of the donor are restored by the back energy transfer and its apparent lifetime is increased. For large differences between the lifetimes of the excited states involved in the reactions under comparison the back energy transfer yield varies proportionally to the respective lifetimes and the observed kinetics may vary even if the energies of the species involved remains the same. However back energy transfer becomes negligible if the energy difference is 1000 cm<sup>-1</sup> or higher.

#### 4.4.2. Results and discussion

##### 4.4.2.1. Identification of the triplet states sensitized by triplet donors

The triplet state of DPP was estimated to 30 kcal/mol by preliminary MOPAC calculations. The derivatives of the molecule have similar triplet state energies. However the internal triplet yield is very low (<1%). The triplet states may easily be sensitized by triplets of higher energy, where in general an energy difference of the donor to the acceptor triplet of 8-12 kcal/mol is recommended as a driving force<sup>54</sup> according to the dependence  $k_q$  on the excess energy of the donor triplet,  $\Delta E_T$ . Anthracene is a candidate triplet donor. It has a triplet energy of 42 kcal/mol, a triplet yield of 70% and a triplet lifetime of 670  $\mu$ s to 3300  $\mu$ s depending on the solvent<sup>12</sup>.

The triplet states of DPP, DMDPP and DMADPP have been sensitized by anthracene in DMF and dioxane degassed by Ar bubbling for more than 15 minutes. The transient spectra are printed in the figures 4.13, 4.15, 4.16 and 4.17. The absorption of the anthracene triplet is well observable at 425 nm. Fig. 4.14 b shows the rise and decay of the triplet signal. The rise of the transient absorption at 530 nm (fig. 4.14 b) corresponds to the decay of the <sup>3</sup>anthracene\* at 425 nm (fig. 4.14 a) thus showing that <sup>3</sup>anthracene\* is quenched by DPP. The transient at 530 nm may therefore be attributed to <sup>3</sup>DPP\*. The differences in the kinetics between <sup>3</sup>anthracene\* decay and <sup>3</sup>DPP\* rise are due to the recovery from the fluorescence signal at 530 nm that is superimposed to the <sup>3</sup>DPP\* signal.

In degassed (Ar bubbled) dioxane solution <sup>3</sup>DPP\* has a lifetime of 130  $\mu$ s. The addition of a drop of D<sub>2</sub>O to 3 ml solution resulted in an increase of the lifetime of <sup>3</sup>DPP to 160  $\mu$ sec. This effect is due to the change in the Franck-Condon factor. DPP can be deprotonated on the nitrogen atoms of the pyrrole rings<sup>5</sup> and can therefore

easily undergo proton to deuterium exchange. The observation supports the identification of the transient as the triplet of DPP.

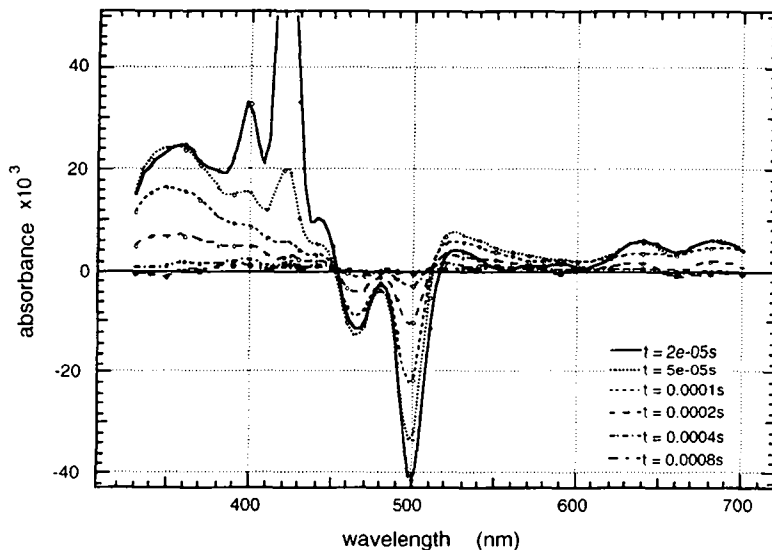


Fig. 4.13: Transient triplet absorption spectrum of DPP  $3.5 \cdot 10^{-5} \text{ mol l}^{-1}$  in dioxane sensitized by anthracene ( $1.5 \cdot 10^{-4} \text{ mol l}^{-1}$ ).  $\lambda_{\text{ex}} = 347 \text{ nm}$ .

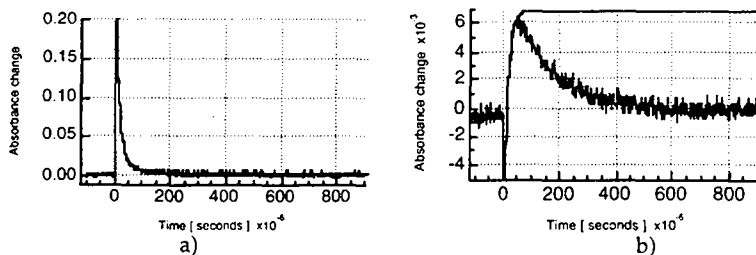


Fig. 4.14: Transient absorption signals at 425 nm (a) and 530 nm (b) of DPP  $3.5 \cdot 10^{-5} \text{ mol l}^{-1}$  in dioxane sensitized by anthracene. Excitation at 347 nm. Double exponential fit to a) yielded rate parameters of  $11400 \text{ s}^{-1}$  and  $65500 \text{ s}^{-1}$  and single exponential fit to b) from time zero to  $50 \mu\text{s}$  yielded a rate parameter of  $77500 \text{ s}^{-1}$ . Transient spectrum see fig. 4.13.

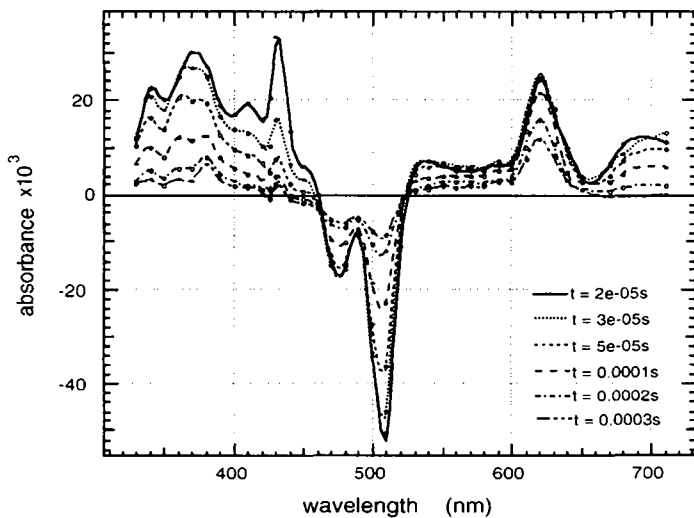


Fig. 4.15: Transient triplet absorption spectrum of DPP  $4 \cdot 10^{-5} \text{ mol l}^{-1}$  in DMF sensitized by anthracene ( $1.0 \cdot 10^{-4} \text{ mol l}^{-1}$ ). Excitation at 347 nm.

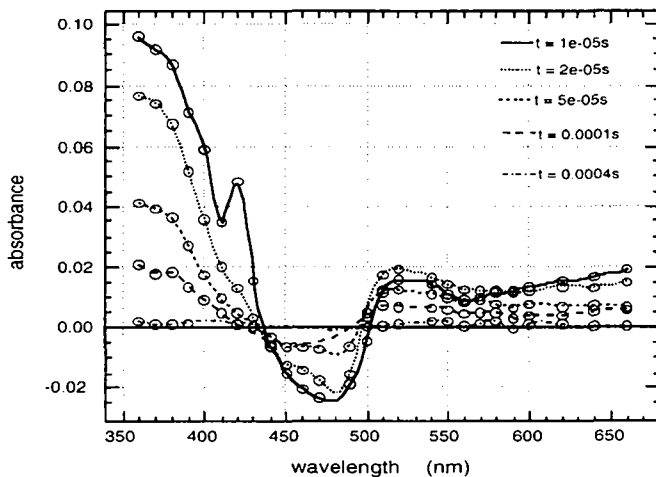


Fig. 4.16: Transient triplet absorption spectrum of DMDPP  $7.5 \cdot 10^{-5} \text{ mol l}^{-1}$  in dioxane, sensitized by anthracene ( $9 \cdot 10^{-5} \text{ mol l}^{-1}$ ). Excitation at 347 nm.

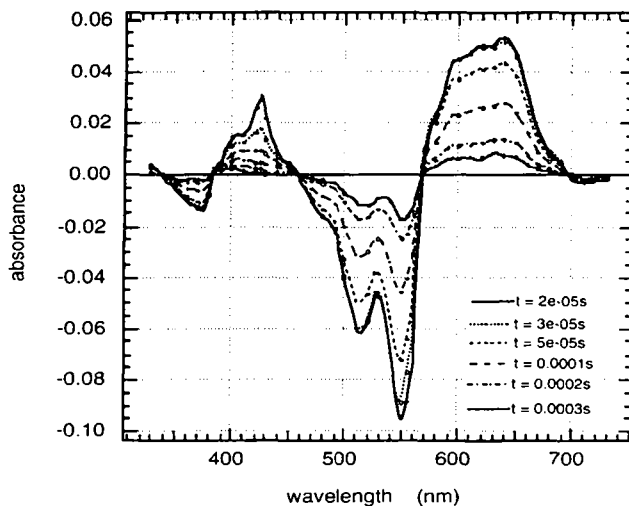


Fig. 4.17: Transient triplet absorption spectrum of DMADPP  $2 \cdot 10^{-5} \text{ mol l}^{-1}$  in DMF, sensitized by anthracene ( $8 \cdot 10^{-5} \text{ mol l}^{-1}$ ). Excitation at 347 nm.

The triplet transient spectra of DMDPP and DPP show a large structureless absorption. Triplet states often exhibit large structureless absorption spectra, such as for rose bengal<sup>57</sup>. DMADPP has a more structured triplet absorption spectrum, reflecting the fact that its vibronic structure is different from the two former molecules.

For DPP in DMF a second transient species with different kinetics and a characteristic absorption peak at 620 nm is observed. This species is completely absent in dioxane. Distinction from the triplet species is easily made based on the different kinetics and the well defined absorption peak. The 620 nm transient is observed in DMF which has a high dielectric constant of 36.7<sup>12</sup> but not in dioxane which has a low dielectric constant of 2.2<sup>12</sup>. This suggests that it is produced by electron transfer. From the bathochromic shift the transient may be attributed rather to the radical anion of DPP than to the cation. This is confirmed by the transient produced by the addition of an electron donor, triethanolamine (TEA), to a DMSO solution of DPP. In pure DMSO the 620 nm transient was not observed. The transient is presented in fig. 4.18. Triethanolamine has an oxidation potential of +1.15V vs SCE. The redox potentials for DPP was measured by cyclic voltammetry in degassed DMF with 0.1 mol l<sup>-1</sup> TBATFB (tetrabutylammonium tetrafluoroborate) and on a glassy carbon electrode. The oxidation potential of ground state DPP lies at 840 mV

vs SCE and the reduction potential is at -1130 mV vs SCE. Thus the redox potential of the excited state may be calculated,  $E^{\circ}(^1S^*/S^-) = E^{\circ}(S/S^-) + \Delta E_{0-0} = 1300 \text{ mV vs SCE}$ . This value agrees to within 100 mV with the estimation based on Loutfy's rule<sup>58</sup>. This "rule" is based on the observation made for a large variety of photographic dyes that the reduction potential of the excited state is *ca.* 350 mV more positive than the ground state oxidation potential. DPP\* is thus an oxidizing agent for TEA and also able to oxidize DMF.

Using ferrocene as a reducing agent with an even less positive oxidation potential of 307 mV vs SCE<sup>59</sup> a similar transient signal was observed. For DMADPP in DMF no secondary transient was observed. The oxidation potential (+570 mV vs SCE measured in DMSO with 0.2 mol l<sup>-1</sup> TBATFMS (tetrabutylammonium trifluoromethanesulfonate) is considerably less positive than the oxidation potential of DPP (+840 mV vs SCE in DMSO), and using Loutfy's rule we estimate  $E^{\circ}(^1\text{DMADPP}^*/\text{DMADPP}) = 820 \text{ mV vs SCE}$ , thus <sup>1</sup>DMADPP\* is less oxidizing and not able to oxidize DMF.

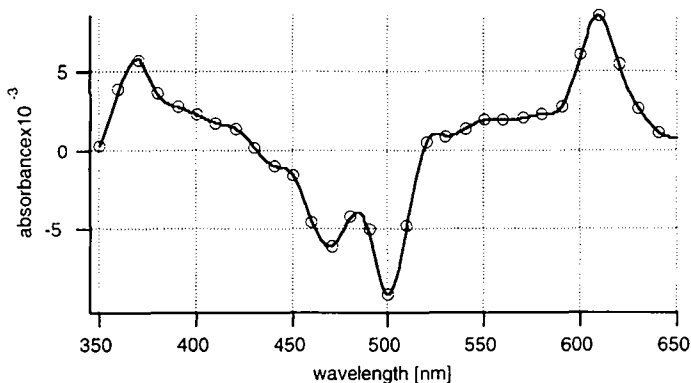
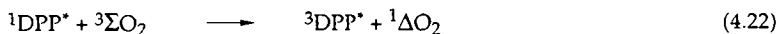


Fig. 4.18: Transient absorption spectrum of  $4 \cdot 10^{-5} \text{ mol l}^{-1}$  DPP and  $0.3 \text{ mol l}^{-1}$  Triethanolamine in DMSO recorded at  $t = 10 \mu\text{s}$  after laserpulse. Excitation at 347 nm.

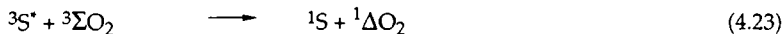
#### 4.4.2.2. Triplet state energy

It was observed that DPP is able to sensitize <sup>1</sup> $\Delta\text{O}_2$  ( see chap. 4.3) through the following reaction:



Usually this reaction is not considered, because a) for dyes absorbing in the visible the energy difference of  $E(^1S^*) - E(^3S^*)$  is too small to sensitize <sup>1</sup> $\Delta\text{O}_2$  and b)

the lifetime of the singlet excited state of the sensitizer  $^1S^*$  is short compared to its triplet lifetime  $^3S^*$ , hence the latter has much higher probability to react with  $^3\Sigma O_2$ . The reaction considered for the majority of the  $^1\Delta O_2$  sensitizers S is:



The fact that reaction 4.22 is relevant raises the question of the energy of the first triplet state of DPP above the ground state and the structure of the excited state. According to the generally applied rules, aromatic ketones have small singlet-triplet energy splittings<sup>22</sup> and only a few visible light absorbing dyes have high enough singlet-to-triplet energy splitting (greater than 22.5 kcal/mol) to allow singlet oxygen sensitization.

Triplet energies  $E_T$  can be measured by different methods. Similarly to the method of measuring the first singlet state  $E(S^*)$  it can be estimated by the phosphorescence spectrum of the compound<sup>60</sup>. However, this method bears several difficulties:

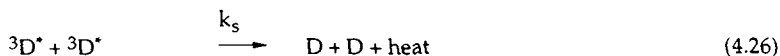
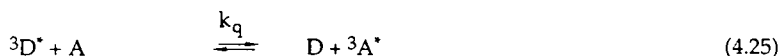
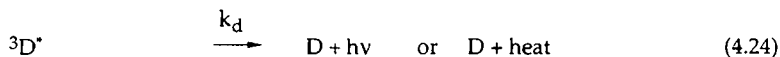
- phosphorescence yields are often small due to competition of the radiative triplet decay with vibrational deactivation.
- the phosphorescence yield is limited by the triplet yield
- for low triplet energies the phosphorescence spectrum is expected in the infrared region above 1000 nm, thus out of the detection range of most presently available fluorimeters.

The first difficulty can be reduced by freezing the molecule in a solvent matrix. The second can be reduced by enclosing the molecule into micelles including heavy atoms<sup>51</sup> thereby rendering the singlet to triplet transitions more allowed through the spin-orbit coupling induced by the heavy atoms<sup>50</sup>. Thereby the triplet yield is enhanced and the phosphorescence lifetime shortened. The third difficulty is dependent on the available instrumentation and could not be circumvented.

Another method to determine the triplet energies consists of measuring the triplet energy transfer rate from a donor to the acceptor molecule as a function of the energy difference between the donor and acceptor triplet states. This method has been widely used for organic molecules<sup>53,61</sup>, including molecules with low lying triplet states<sup>43,62</sup>.

*Triplet energy transfer method*

The triplet energy transfer method is based on the measurement of the bimolecular reaction rate of the quenching of the triplet state of the donor molecule by the acceptor molecule using the flash photolysis transient absorption method. The observed triplet lifetime is determined by the following reactions:



thus yielding the following kinetics:

$$\frac{d[{}^3\text{D}^*]}{dt} = k_d [{}^3\text{D}^*] + k_q [{}^3\text{D}^*][\text{A}] + k_s [{}^3\text{D}^*]^2 \quad (4.27)$$

where:

$k_d$  = natural decay constant of the triplet state

$k_s$  = bimolecular rate constant triplet-triplet annihilation

$$k_q = \frac{d\left(\frac{d[{}^3\text{D}^*]}{dt}\right)}{d[\text{A}]} = \frac{1}{1 + \exp(-\Delta E_T/kT)} \quad (4.28)$$

$$\Delta E_T = E_T(\text{D}) - E_T(\text{A})$$

Precautions need to be taken to reduce the quadratic term in eq. 4.27 to a negligible amount to allow simplified and more precise interpretation of the kinetics as a pseudo first order reaction. This can be achieved by reducing the excitation energy, i.e. the concentration of  ${}^3\text{S}^*$  produced during the flash photolysis experiment. The fulfillment of these conditions may be controlled by the quality of the resulting decay fit to the exponential equation and the independence of the decay constant of the excitation energy.



In the present case, DPP has a very low triplet yield. It can therefore not act as a triplet donor, but only as an acceptor. A series of triplet donors was chosen with energies around the triplet energy of DPP. In the experiments, the donor triplets were monitored by their transient absorption. For high acceptor concentrations the kinetics could be cross checked by the observation of the rise of the acceptor triplet. Care was taken to observe the donor triplets close to isosbestic points of the acceptor's transient spectrum. This allows to obtain a transient signal which is independent of the acceptor kinetics, thus allowing to measure purely the donor kinetics. Isosbestic points were determined from the TEMPO or O<sub>2</sub> enhanced transient triplet spectra.

Compound	sensitizer		$\lambda_{\text{obs}}$ [nm]	Quencher	$k_Q$ [10 <sup>7</sup> M <sup>-1</sup> s <sup>-1</sup> ]
	$E_T^a$ [kcal M <sup>-1</sup> ]	$\lambda_{\text{max}}^b$ [nm]			
Fluorenone	50.3	430	445	DMA DPP	150
Pyrene	48	420		DPP	220
Anthracene	42	425, 431	430	DPP	300
Anthracene	42	425, 431	430	DMA DPP	139
DPH	34	422	430	DMA DPP	190
DPO	28.5	440	445	DPP	133
DPO	28.5	440	435	DMA DPP	29
Zinc Phthalocyanine	26.5	480	445	DMA DPP	2.7
Zinc Phthalocyanine	26.5	480	445	DPP	0.94

Table 4.6: Spectral and kinetic properties of triplet donors and DPP triplets in solution. <sup>a</sup> Ref. <sup>12</sup> <sup>b</sup> Ref. 54.

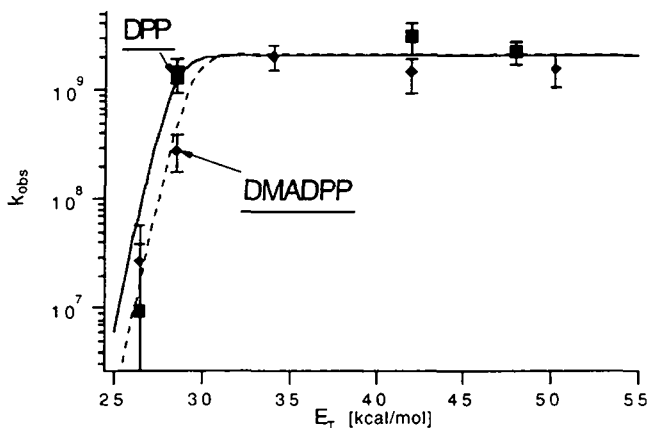


Fig. 4.19: Graph based on equation 4.28 of the quenching rates of various triplet donors by DPP and DMA DPP. The lines show the fit obtained from eq. 4.28. The quenching rates were determined from the slopes in Stern-Volmer plots for each triplet donor. The solvent was DMF. The Excitation wavelength was 355 nm for all triplet donors.

Figure 4.19 shows the quenching rates of DPP and DMADPP for the various triplet sensitizers and the corresponding fit according to eq. 4.28. The resulting fitting parameters are the triplet energies for DPP of  $28.5 \pm 2$  kcal and for DMADPP of  $29.4 \pm 2$  kcal.

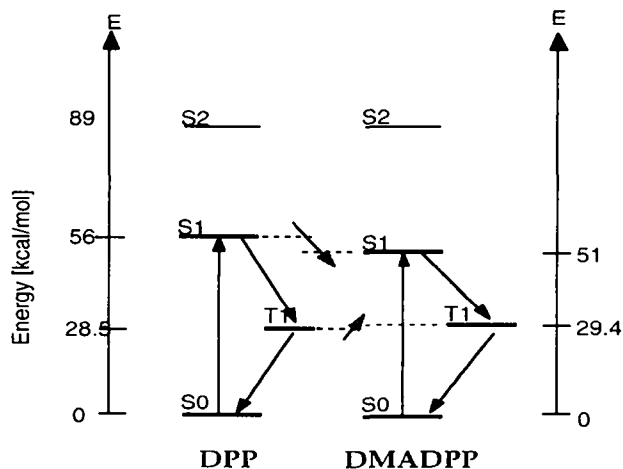


Fig. 4.20: energy diagrams of DPP and DMA DPP ground and excited states.

The triplet energies of both DPP and DMADPP are low if compared to other organic dyes absorbing in the same wavelengths range, as shown in table 4.7. Moreover, they do not follow the general rule, that ketones have small singlet-triplet splittings<sup>22</sup>. From the MO calculations (see chapter 4.5) the first transition is shown to be a  $\pi - \pi^*$  transition and not a  $n - \pi^*$  transition as is usually the case for ketones, and the generally small singlet-to-triplet splitting is therefore not found in DPP's. As indicated by the arrows in figure 4.20 the energy of the first triplet state is higher for DMADPP than for DPP while the energy of its first singlet excited state is lower. The triplet energies don't scale with the singlet energies as they do for e.g. diphenylpolyenes<sup>52</sup>, fullerenes<sup>12,61</sup> naphthalenes<sup>12</sup>. Since the singlet-to-triplet energy splitting is due to spin correlation, the spin distribution and in particular the spin interaction between the HOMO and the LUMO change between DPP and DMADPP. The MO calculations below (chapter 4.5) will give an explanation of these observations based on the spatial form of the molecular orbitals.

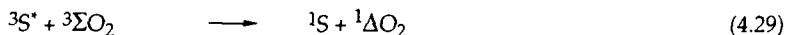
compound	$E_S$ [kcal]	$E_T$ [kcal]
DPP	56	28.5
DMADPP	51	29.5
Acridine orange	56	49.3
2-amino-Anthracene	61.5	44
Azulene	40.7	39
$C_{60}$	46.2	36.1
Chlorophyll <i>a</i>	42.34	29.9
Phthalocyanine	47	28.7
Rhodamine B	50.9	42.6
Perylene Bis (2,5-di- <i>tert</i> -butylphenyl)imide	54	27.5

**Table 4.7:** Singlet and triplet energies of DPP's and various dyes for comparison. The data are compiled from Murov<sup>12</sup>.

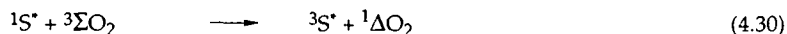
The singlet-to-triplet energy splitting is thus larger or equal to the energy of singlet oxygen. The low triplet energies explain, why the singlet states of DPP's are efficiently quenched by ground state oxygen to yield singlet oxygen, since the singlet-to-triplet energy splitting allows to sensitize a singlet oxygen molecule. The resulting triplet states of DPP can thereafter be quenched again by ground state oxygen to yield a second singlet oxygen molecule.

#### 4.4.2.3. Triplet enhancement by $O_2$

Singlet oxygen plays an important role in the degradation of DPP monomers. The commonly considered way of sensitization of is energy transfer from a donor in its triplet state to ground state oxygen.



DPP's have very low triplet yield of  $\approx 1\%$  and this reaction is a priori not important. However, since the singlet to triplet energy splitting is high enough to allow to sensitize  ${}^1\Delta O_2$ , oxygen enhances the triplet yield of S through the following equation:

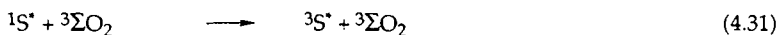


The  ${}^3S^*$  subsequently can sensitize  ${}^1\Delta O_2$  through eq. 4.29

The reaction 4.30 is referred to as oxygen triplet yield enhancement due to its similarity with paramagnetic species and heavy atom enhancement of triplet yields.

The processes in these three cases are however different. The case of paramagnetic species (e.g. stable radicals) will be discussed below.

The quenching of triplet states of aromatic hydrocarbons by oxygen is usually thought of as energy transfer to  ${}^3\Sigma\text{O}_2$  yielding  ${}^1\Delta\text{O}_2$ <sup>48</sup>. It was found that oxygen quenching of energy transfer to  ${}^3\Sigma\text{O}_2$  could be accounted for by an energy-transfer theory (Kearns<sup>63</sup>, Chattopadhyay<sup>48</sup> and ref therein or Patterson<sup>64</sup>), leading to an energy gap law analogous to the energy-gap law of radiationless transitions. However paramagnetic quenching (eq. 4.31) can not be excluded and may reduce the triplet yield enhancement.



In the following the DPP triplet yield enhancement by oxygen will be demonstrated.

#### Experiments and results

Hug et al.<sup>52</sup> have proposed a method to measure the enhancement of triplet yield  $\delta$ , which is defined as

$$\delta = \frac{\text{number of quenching events resulting in a triplet excited state}}{\text{total number of quenching events}} \quad (4.32)$$

In the laser flash photolysis experiment, the triplets can be observed in the transient absorption spectrum.  $\Delta\text{OD}^{\text{T}}$  represents the absorption at the end of the laserpulse. It has been calculated as the extrapolation to  $t=0$  of the decay signal of the triplets. In this manner, the fast transient signals of the  $\text{S}_1$  state and fluorescence that would be observed at the end of the laserpulse are ignored.  $\Delta\text{OD}^{\text{To}}$  represents the signal without any quencher Q.

The triplets are generated by internal intersystem crossing and by enhanced intersystem crossing. The decay of  $\text{S}^*$  is thus described by the following kinetics:

$$\frac{d[\text{S}^*]}{dt} = -k_{\text{F}}[\text{S}^*] - k_{\text{isc}}[\text{S}^*] - k_{\text{q}}^{\text{S}}[\text{S}^*][\text{Q}] \quad (4.33)$$

and for te triplet

$$\frac{d[{}^3\text{S}^*]}{dt} = +k_{\text{isc}}[\text{S}^*] + \delta k_{\text{q}}^{\text{S}}[\text{S}^*][\text{Q}] \quad (4.34)$$

Thus:

$$\begin{aligned}
\frac{\Delta OD^T}{\Delta OD^{T_0}} &= \frac{\Phi_T}{\Phi_{T_0}} \\
&= \frac{k_o^S}{k_o^S \Phi_{T_0}} \frac{\delta k_q^S [Q] + k_o^S \Phi_{T_0}}{k_o^S + k_q^S [Q]} \\
&= \frac{k_o^S}{k_o^S + k_q^S [Q]} \frac{\delta k_q^S [Q] + k_o^S \Phi_{T_0}}{k_o^S \Phi_{T_0}} \\
&= \frac{1}{1 + K_{SV} [Q]} \left[ \frac{\delta}{\Phi_{T_0}} K_{SV} [Q] + 1 \right] \\
\frac{\Delta OD^T}{\Delta OD^{T_0}} &= 1 + \left[ \frac{\delta}{\Phi_{T_0}} - 1 \right] \frac{K_{SV} [Q]}{K_{SV} [Q] + 1} \quad (4.35)
\end{aligned}$$

Where  $K_{SV}$  is the Stern-Volmer constant for the singlet quenching. This is the result proposed by Hug et al.<sup>48</sup>. Transforming this result allows to estimate both  $\delta$  and  $k_q^S$  from the intercept and slope of the following plot<sup>52</sup>:

$$\left( \frac{\Delta OD^T}{\Delta OD^{T_0}} - 1 \right)^{-1} = \left[ \frac{\delta}{\Phi_{T_0}} - 1 \right]^{-1} \left[ \frac{1}{K_{SV} [Q]} + 1 \right] \quad (4.36)$$

Eq. 4.36 allows to determine simultaneously  $\delta$  and  $K_{SV}^T$ . But for a small  $\Phi_{T_0}$ , small values of the intercept are expected, and the values will be affected by large errors. Eq. 4.35 is preferred.

Since  $K_{SV}$  is the Stern-Volmer constant for the quenching of  $^1S^*$  independently of the resulting states, it can be measured accurately by the measurement of the quenching of the fluorescence and eq. 4.35 allows more accurate estimation of  $\delta$ . The results for  $\delta$  are dependent of  $\Phi_{T_0}$ , which has been directly estimated from  $\Delta OD^{T_0}$ :

$$\Phi_{T_0} = \frac{\Delta OD^{T_0} N_A}{\epsilon_{\lambda_{obs}} \cdot n_{\text{photons,exc.}} \cdot (1 - 10^{-A_{\lambda_{exc}}})} \quad (4.37)$$

However, for small values of  $\Phi_{T_0}$  this estimation again results in relatively large errors, due to the very small signal of  $\Delta OD^{T_0}$  that needs to be measured and to residual  $O_2$  that may enhance the triplet yield.

The singlet oxygen yield was measured directly by phosphorescence detection of the singlet oxygen emission at 1270 nm (see chapter 4.3.2.1.). The results are summarized in table 4.4. In aerated solutions the singlet oxygen yield is 15%. But in the same conditions we find that for DMDPP only  $\approx 7\%$  of  $^1S^*$  are quenched by  $O_2$  and the internal intersystem crossing is less than 1%. This allows the conclusion, that for every quenched singlet excited state of DPP,  $^1S^*$ , two singlet oxygen molecules  $^1\Delta O_2$  are produced: one through reaction 4.30 and the second one through reaction

4.29. It follows then, that  $\delta$  must be unity. We may thus go backwards through the previous calculations and use the results to estimate  $\Phi_{T0}$  more precisely.

Determination of  $K_{SV}$  and  $k_q^S O_2$

$k_q^S O_2$  has been measured by fluorescence quenching. For each compound three different oxygen concentrations can be well controlled: solution in equilibrium with air, i.e. with a 21%  $O_2$  containing gas, deaerated solution and oxygen saturated solution. The two latter equilibriums were produced by bubbling argon and oxygen respectively. The results are summarized in table 4.8.

compound	solvent	$K_{SV}$	$k_o [10^8 s^{-1}]$	$k_q^S O_2 [10^9 mol^{-1} s^{-1}]$	$k_{diff} [10^9 s^{-1}]$
DMDPP	dioxane	60	1.18	7	4.5
DPP	dioxane	53	1.4	7	4.5
DMADPP	dioxane	43	2.3	9.8	4.5
DMADPP	DMF	56	2.3	13	7.2

Table 4.8: Fluorescence quenching by  $O_2$  of DPP and derivatives in dioxane and DMF, assuming  $[O_2]_{sat} = 6.2 \cdot 10^{-3} mol l^{-1}$  in DMF at 1 atm.

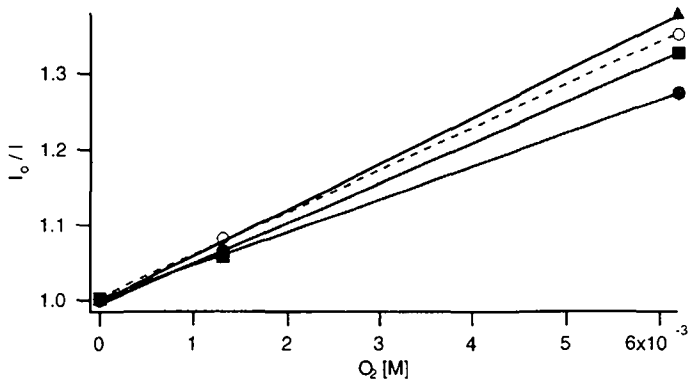


Fig. 4.21: Stern-Volmer plots of fluorescence quenching of DPP and derivatives in dioxane. (■ = DPP, ● = DMADPP, ○ = DMADPP in DMF, ▲ = DMDPP).

$k_{diff}$  is calculated using the Smoluchowski equation and the Stokes-Einstein equation for the diffusion coefficient<sup>22,65</sup> using the approximation of symmetric radii of the reactants. The higher experimental values reflect the fact that the reactant radii are not symmetric,  $O_2$  being smaller than DPP. However calculating  $k_{diff}$  with the exact radii of the reactants yields too high values. The effective radius of DPP is probably not its total molecular radius, but only the pyrrolo-pyrrole part of the molecule, where the frontier orbital is centered. Considering the approximations of

in these formulas, it is concluded that  $k_q^S \text{O}_2$  is diffusion controlled. DMADPP has a higher value than expected considering the fact that the singlet to triplet energy splitting is only  $21.5 \pm 2$  kcal/mol. It may however be explained considering the slightly larger geometric radius of the molecule and more extended HOMO. This effect is increased by the larger extension of the ground state to the phenyl rings and amino groups of the molecule.

#### Determination of $\delta/\phi_{T0}$

The triplet enhancement has been measured in the flash photolysis experiment. DMDPP was taken as a model compound for all DPP's, since it is the only one with a measurable absorbance of the intrinsic triplets and high enough solubility in dioxane, where no secondary reactions were observed that could have influenced the  $\Delta OD_0$ . Both DPP and DMADPP showed no measurable triplet yield without oxygen or nitroxyl radicals. The triplet absorption at the time 0 has been determined by the extrapolation of the decay signal of the triplet to  $t = 0$ , thus eliminating the effects of  $^1S_2^* \leftarrow ^1S_1^*$  absorption and  $^1S_1^* \rightarrow S_0$  fluorescence.

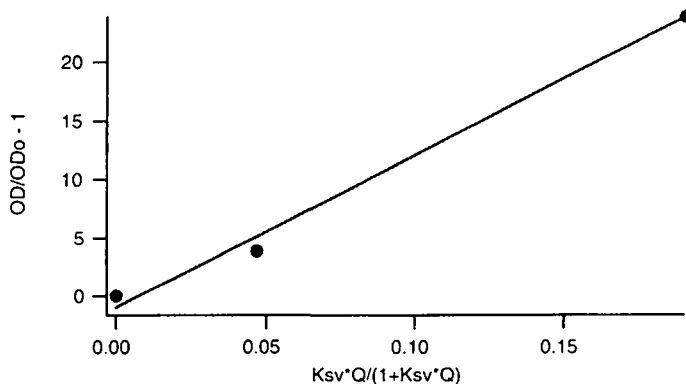


Fig. 4.22: plot of eq. 4.35 with DMDPP and  $Q =$  oxygen in dioxane.

The slope from the data in graph 4.22 is  $\delta/\phi_{T0} = 130$ . From  $\delta = 1$   $\phi_{T0}$  is inferred to be 0.77. This value is in agreement within the error limits with the direct estimations from the transient absorbance of the triplet, where the yield was estimated as 1% and with the fluorescence yield of unity within an error limit of 5%.

The data show that the product of the singlet excited state quenching by molecular oxygen results in the triplet excited state of DMDPP. This is in agreement with the singlet oxygen yield in aerated solvents, where 2 singlet oxygen molecules

are produced per quenched singlet excited  $^1\text{DPP}^*$  and thus confirming that both reactions 4.30 and 4.29 are occurring.

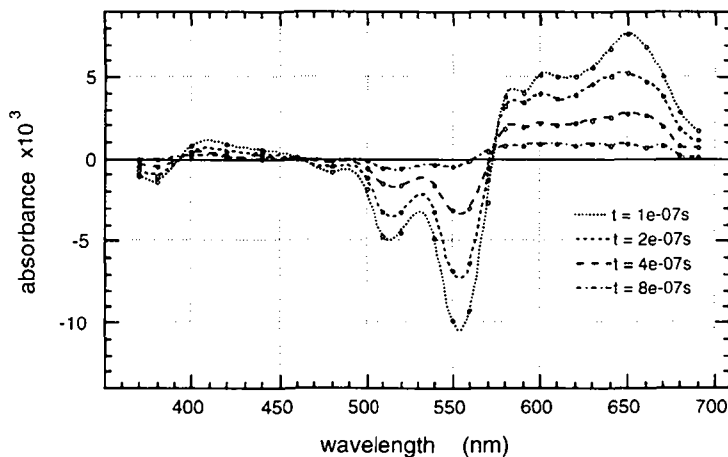
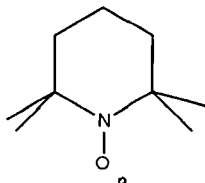


Fig. 4.23: transient absorption spectrum of DMADPP triplet in DMF enhanced by  $\text{O}_2$ .

As an example fig. 4.23 shows the transient spectrum of the DMADPP triplet with oxygen in DMF. Assuming an oxygen concentration of  $1.2 \cdot 10^{-3} \text{ mol l}^{-1}$  in DMF under air the quenching rate of the triplet by oxygen is  $2.7 \cdot 10^9 \text{ mol}^{-1} \text{ sec}^{-1}$ . The corresponding values for DMADPP in dioxane are  $2.5 \pm 0.5 \cdot 10^9 \text{ mol}^{-1} \text{ sec}^{-1}$  and  $2.4 \pm 0.5 \cdot 10^9$  for DPP in dioxane.

#### 4.4.2.4. Triplet enhancement by TEMPO

Tetramethylpiperidine nitroxyl (TEMPO) is widely used as a stabilizer<sup>4</sup> of organic compounds because of its ability to quench the triplet and singlet oxygen. Its diffusional quenching of singlet, doublet and triplet states has been studied extensively over the last 25 years<sup>66-70</sup> and intramolecular quenching has been under investigation<sup>71</sup>.



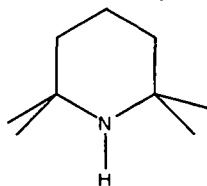
Tetramethylpiperidine nitroxyl (TEMPO)

Many different nitroxide radicals have been investigated, and it has been concluded that the mobility of TEMPO is important for its quenching efficiency in micellar applications.

TEMPO is a nitroxyl radical, also referred to as Nitroxyl Light Stabilizers (NILS) and acts very efficiently in



solution. Its hydrogenated equivalent HALS, a *Hindered Amine Light Stabilizer*, does not have a stabilizing effect on the pigment, whereas the addition of 10% wt of TEMPO brings about a stabilization of a factor<sup>1</sup> of 2. An explanation therefore was given by Bellus<sup>4</sup>. He states that *N*-methyl-tetramethyl piperidine is a very efficient <sup>1</sup>O<sub>2</sub> quencher, but undergoes itself photooxydation yielding HALS, which itself is a poor but stable <sup>1</sup>O<sub>2</sub> quencher. The stabilizing effect of TEMPO in the polymer matrix is poor ( $k=0.5$ ). However, in solution the effect of TEMPO is far more important<sup>1</sup>, supporting the previously cited result, that the mobility plays a major role in the quenching efficiency of nitroxyls. The importance of the nitroso unit has also been demonstrated by different substituents on the amine of TEMPO<sup>1</sup>.



*Hindered Amine Light Stabilizer (HALS)*

Nitroxyls are efficient quencher for the singlet states of organic molecules in solution. The observed reaction rates are in general in the diffusion controlled limit<sup>48</sup>. The triplet enhancement effect of TEMPO and other nitroxyl radicals for stilbene and longer chain diphenylpolyenes was studied by Chattopadhyay et al.<sup>48</sup>.

### *Experiments and results*

#### *Quenching of the singlet excited state of DPP's by TEMPO*

The efficiency of the quenching of the singlet excited state of DPP's was measured by fluorescence quenching in dioxane. TEMPO has a broad absorbance peak between 400 nm and 590 nm, the maximum being around 500 nm with a molar extinction coefficient of  $\epsilon = 5.5 \text{ mol l}^{-1} \text{ cm}^{-1}$ . The emission counts were therefore observed at 600 nm only and needed therefore to be corrected for the loss of excitation intensity due to the absorbance of the quencher added to the solution. The resulting Stern-Volmer plot is given in fig. 4.24

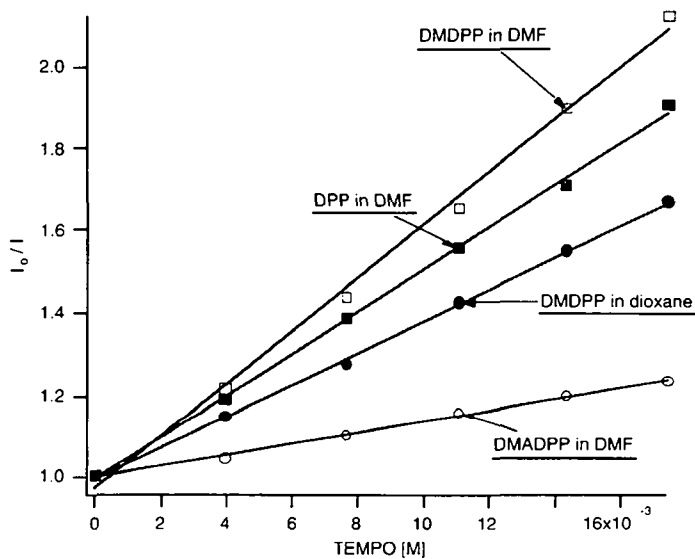
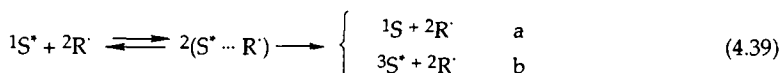
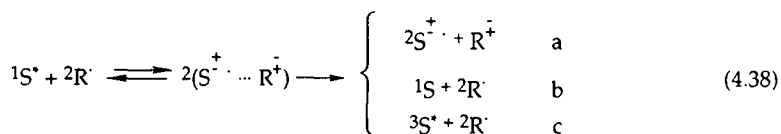


Fig. 4.24: Stern Volmer plot of the excitation corrected emission signal of DPP, DMDPP and DMA DPP fluorescence quenched by TEMPO in different solvents.

compound	solvent	$K_{sv}$	$k_o [10^8 s^{-1}]$	$k_q^S [10^9 mol^{-1} s^{-1}]$	$k_{diff} [10^9 s^{-1}]$
DMDPP	dioxane	38	1.18	4.5	4.5
DMDPP	DMF	65	1.18	7.65	7.18
DPP	DMF	51.4	1.4	7.3	7.18
DMADPP	DMF	13.8	2.3	3.2	7.18

The observed Stern-Volmer constants and the resulting  $k_q^S$  are all in the diffusion controlled limit. The comparison of DMDPP in dioxane and in DMF shows a good agreement of the experimental quenching constant with the theoretical value. No solvent polarity dependence is observed, indicating that the quenching mechanism is not based on electron transfer. This is in agreement with the observations for the singlet excited state quenching of ArH by di-*tert*-butylnitroxyl (DTBN)<sup>72</sup> and by TEMPO<sup>69</sup>. The mechanism of quenching of the singlet excited states is not yet clear. Possible reactions are



The process 4.38 a) is unlikely, since no cations were detected in the transient spectra. If this reaction would happen, one would expect to observe the cation or at least the bleaching of the ground state of S. The fact that the cation does not absorb in the visible has been demonstrated by the oxidation of DMDPP<sup>\*</sup> by methyl viologen<sup>73</sup>, where only the bleaching of DMDPP and the absorption of MV<sup>+</sup> were observed. Moreover the expected kinetics of the decay signal would be of second order from the recombination of S<sup>+</sup> and R<sup>·</sup>, as observed for MV<sup>++</sup>. TEMPO has a weak and broad absorption spectrum from 400 nm to 590 nm that has been assigned<sup>72</sup> to a symmetry-forbidden spin-allowed (doublet-doublet) transition of n $\rightarrow$   $\pi^*$  character. The excited state energies of DPP are comparable to the excitation energy of TEMPO, but the energy splitting E(S<sub>1</sub>) - E(T<sub>1</sub>) would be too low to excite TEMPO to its first excited state. We may therefore exclude any interaction through long range<sup>74</sup> (Förster type) or short range<sup>56</sup> (Dexter type) energy transfer. The same conclusion has been drawn by Green et al.<sup>72</sup> and Chattopadhyay et al.<sup>48</sup>. The same authors also argued against the charge-transfer mechanism (eq. 4.38 a-c) on the basis of a lack of solvent dependence of k<sub>q</sub><sup>S</sup>. The present data allow the same conclusions for the interaction with DPP. The lack of observation of the cation, second order kinetics and solvent dependence for the quenching of the singlet excited states argues strongly against a mechanism involving extensive charge transfer between the partners in a collisional complex.

The triplets of DPP, DMDPP and DMADPP have been produced by the above explained mechanism and the transient absorption spectra were observed in a flash photolysis experiment. Comparison of these with the donor sensitized triplet spectra allows the identification of the TEMPO enhanced transient species as the triplets of the DPP compounds. The transient spectrum of DPP in DMF shows the same additional absorption at 620 nm with a different lifetime as observed with the triplet donor anthracene.

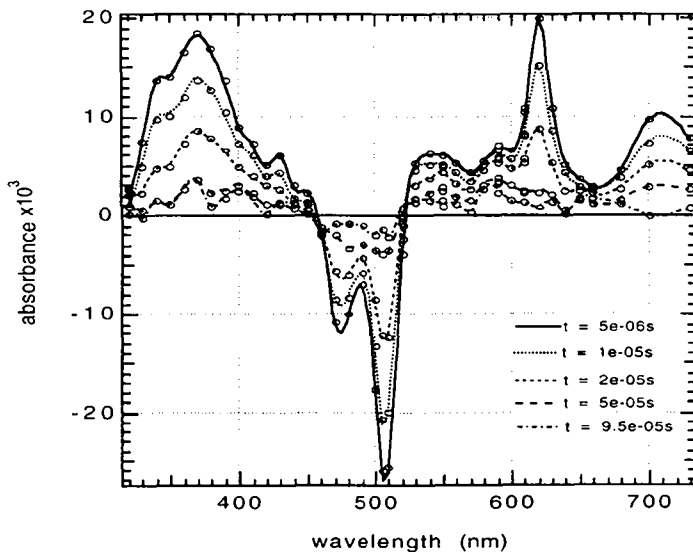


Fig. 4.25: transient triplet absorption spectrum of DPP enhanced by TEMPO in DMF. The concentrations were: TEMPO:  $0.02 \text{ mol l}^{-1}$ , DPP:  $2.5 \cdot 10^{-5} \text{ mol l}^{-1}$ . Excitation wavelength was 347 nm.

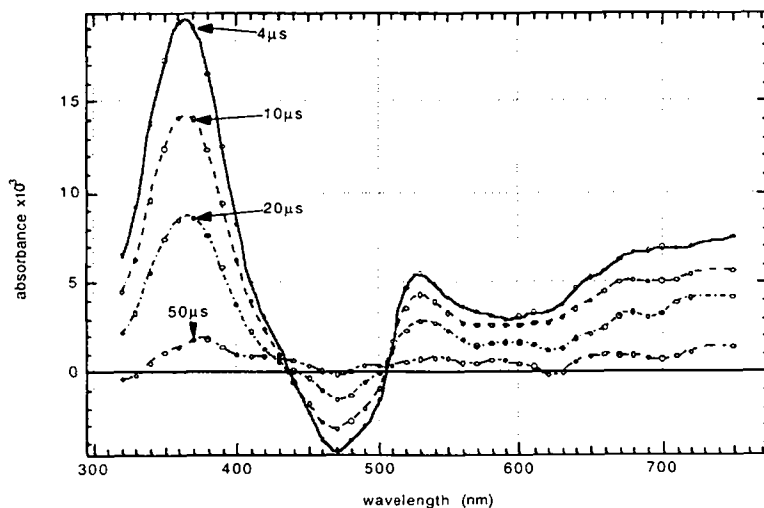


Fig. 4.26: transient triplet absorption spectrum of DMDPP enhanced by TEMPO in dioxane. The concentrations were: TEMPO:  $0.02 \text{ mol l}^{-1}$ , DMDPP:  $5 \cdot 10^{-5} \text{ mol l}^{-1}$ . Excitation wavelength was 347 nm.

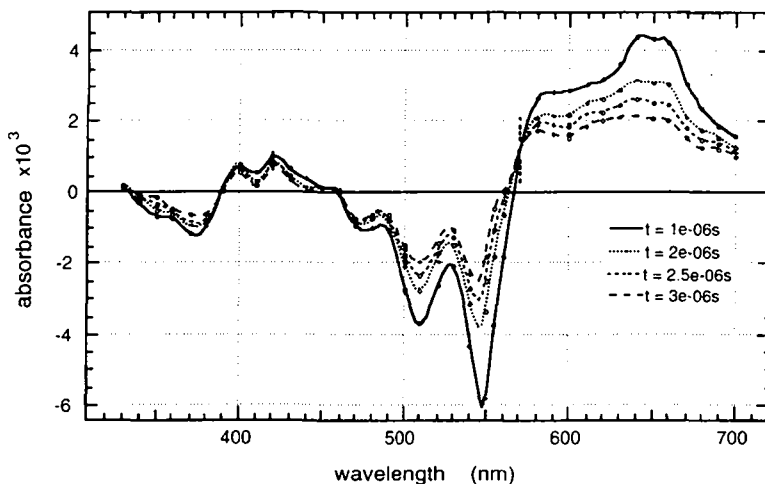


Fig. 4.27: transient absorption spectrum of DMADPP triplet enhanced by TEMPO in DMF. The concentrations were: TEMPO:  $0.03 \text{ mol l}^{-1}$ , DMADPP:  $1 \cdot 10^{-5} \text{ mol l}^{-1}$ . Excitation wavelength was 532 nm.

#### Determination of $\delta/\phi_{T_0}$

The value of the triplet yield enhancement by TEMPO has been measured in a similar way as for  $\text{O}_2$  for DMDPP as a model compound.

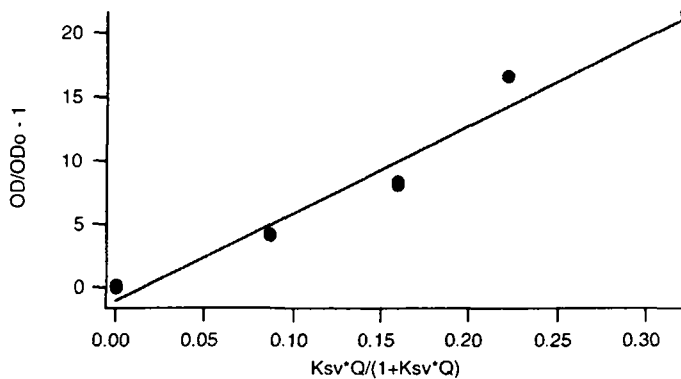


Fig. 4.28: Triplet yield enhancement by TEMPO. Plot according to eq. 4.35 for DMDPP in dioxane with  $Q = \text{TEMPO}$ . The concentrations were: DMDPP:  $5 \cdot 10^{-5} \text{ mol l}^{-1}$ , TEMPO:  $2.5 \cdot 10^{-3}$  to  $12.5 \cdot 10^{-3} \text{ mol l}^{-1}$ . Excitation wavelength was 347 nm.

From the data in figure 4.28 the slope gives  $\delta/\phi_{T_0} = 69$ . Using the value  $\phi_{T_0} = 0.77$  determined above in the oxygen triplet enhancement experiments, this yields  $\delta = 0.53$ . This value is in the range of the values observed for diphenylpolyenes<sup>48</sup>. For DPO, which has the same triplet energy as DPP,  $\delta = 0.54$  was found in nonpolar solvents<sup>48</sup>. The  $\delta$ -value for TEMPO is smaller than for oxygen. But still half of the quenched singlet excited molecules are found in the triplet state, from where they may sensitize singlet oxygen and undergo degradation if the produced singlet oxygen is not intercepted by TEMPO again. TEMPO may therefore have not only a stabilizing effect but also enhance the degradation of the dye. The relative diffusion rates of the compounds will be important for whether the stabilizing or degrading effect will be more important.

## 4.5. Molecular Orbital Calculations based on Semiempirical Quantum Mechanical Methods

The quantum mechanical treatment of a system allows to give a comprehensive description and to account for the observations linked to purely quantum mechanical concepts such as the spin. However their complexity prevents their analytically rigorous applications to large molecules. Approximations need to be accepted. The applications to larger systems such as polyatomic molecules and solids have lead to the solid development of methods using drastic approximations and have proven to produce very useful results to explain the experimental observations. The most widely used among these are the ab-initio method and its semiempirical simplified modifications CNDO and INDO, Extended Hückel and density functional theory. These methods allow with reasonable efforts to treat molecules such as DPP. The calculated parameters are rarely in quantitative agreement with the experimental observations, but are a powerful tool for the explanations of variations within a family of similar molecules. In the following part semiempirical methods are used to elucidate the variations of experimentally observed parameters on different derivatives of DPP.

### 4.5.1. Theory

The computational methods used in this work are based on the molecular orbitals constructed from linear combination of atomic orbitals (LCAO-MO). Ab-initio methods and semiempirical methods are based on these models. They are convenient for their conceptual simplicity. Atomic orbitals are constructed using approximations (Slater orbitals) to the precise solutions of the atomic hamiltonians. They are allowed to be a linear combination of several approximated solutions (Slater orbitals approximated by several gaussians). Molecular orbitals are then constructed again as a linear combination of these atomic orbitals. Their coefficients are optimized by the variational principle using the Hartree Fock operator in an iterative process towards a self consistent solution of the problem, called the self consistent field (SCF) approximation. The theoretical developments are well presented by e.g. Atkins<sup>50</sup> or Rivail<sup>49</sup>.

Using the Born-Oppenheimer approximation the Hamiltonian of the electronic wavefunction  $\Psi$  for a molecule may be written in atomic units as:

$$H = \sum_{i=1}^n H_i^c + \sum_{i,j} \frac{1}{r_{ij}} \quad (4.40)$$

where

$$H_i^c = -\frac{1}{2} \Delta_i + V_{Ni} \quad (4.41)$$

$\Delta_i = \frac{\partial^2}{\partial x_i^2} + \frac{\partial^2}{\partial y_i^2} + \frac{\partial^2}{\partial z_i^2}$  is the Laplace operator, and  $V_{Ni}$  is the coulomb potential of the nuclei for the electron  $i$ .

$$H^c = \sum_k H_k^c$$

i.e.  $H_i^c$  is the one electron Hamiltonian for the molecule, and  $r_{i,j}$  is the distance between the electrons  $i$  and  $j$ .

In the LCAO-MO approximation, the total electronic wavefunction  $\Psi$  can be written in the form of the Slater determinant to obtain a fully antisymmetrized wavefunction in order to satisfy Pauli's principle:

$$\Psi = \frac{1}{\sqrt{N!}} \begin{vmatrix} \chi_1(1) & \dots & \chi_1(n) \\ \vdots & & \vdots \\ \chi_n(1) & \dots & \chi_n(n) \end{vmatrix} \quad (4.42)$$

where the spin-orbitals  $\chi_k(1)$  are the product of a spatial wavefunction  $\phi$  and a spin function  $\sigma$

$$\chi_k(1) = \phi_k(1) \sigma_k(1) \quad (4.43)$$

Using Slater determinants for the total electronic wavefunction, the energy calculated by the electronic hamiltonian (eq. 4.40) can be expressed in the following way:

$$E = \sum_k \langle \chi_k(1) | H^c(1) | \chi_k(1) \rangle + \sum_{k,l>k} [ J_{kl} - K_{kl} ]$$

where  $J_{kl}$  is the coulomb integral and  $K_{kl}$  is the exchange integral given by:



$$J_{kl} = \langle \varphi_k(1)\varphi_l(2) | \frac{1}{r_{1,radix,2}} | \varphi_k(1)\varphi_l(2) \rangle \quad (4.44)$$

$$K_{kl} = \langle \varphi_k(1)\varphi_l(2) | \frac{1}{r_{1,radix,2}} | \varphi_l(1)\varphi_k(2) \rangle \quad (4.45)$$

Since the total wavefunction consists of the spatial part of  $\varphi$  and the spin functions  $\sigma$  these terms are multiplied by the spin overlap integrals. In the case of the exchange integral this spin overlap integral is zero if  $\varphi_l$  and  $\varphi_k$  are not associated to the same spin (both up or both down). Therefore this term explains the singlet to triplet energy splitting of the first excited states of a molecule. In the case of all electronic states being pure configurations and the molecule being in the first singlet excited state, the electrons in the HOMO and LUMO have paired spins, whereas in the triplet state these spins are unpaired. Thus the only term of the total energy expression that changes upon changing the spin of the excited electron is the term  $K_{kl}$  where  $k$  and  $l$  stand for the HOMO and the LUMO respectively. The remaining terms, i.e. where either  $k$  or  $l$  stand for an orbital HOMO -1 or less, are unchanged.

The singlet to triplet energy splitting is therefore strongly determined by the value of the exchange integral between HOMO and LUMO. Yet another phenomenon affects the singlet to triplet energy splitting. From Pauli's principle it follows that the total electronic wavefunction  $\Psi$  needs to be antisymmetric. In the ground state, supposed to be a singlet state for this discussion, the spin functions are antisymmetric and the spatial wavefunction is therefore symmetric. In the triplet state however the spin function is symmetric with regard to the unpaired spins and the corresponding spatial wavefunctions need therefore to be antisymmetric. If we denote  $\vec{x}_1$  and  $\vec{x}_2$  the coordinates for the unpaired electrons it follows from antisymmetry of  $\Psi$ , that the spatial wavefunction vanishes for  $\vec{x}_1 = \vec{x}_2$ . The spatial distribution of  $\Psi$  is thus changed between the singlet and triplet state. This phenomenon is called misleadingly *spin correlation*, since it is not a direct consequence of the spins, but a consequence of Pauli's principle. The effect of the antisymmetry in the spatial wavefunction is that the electrons with parallel spin avoid each other and thus the repulsion term decreases.

In the following we give a brief outline of the semiempirical methods used and the different approximations they involve.

#### 4.5.1.1. *Methods used for calculation of electronic spectra*

The calculations presented in this work are based on the semiempirical INDO/S method<sup>75</sup> implemented in the program package ZINDO. INDO stands for

Intermediate Neglect of Differential Overlap. This method is based on the Hartree-Fock Self Consistent Field (SCF) algorithm.

According to the standard notation we denote in the following the interelectronic repulsion integrals (eq. 4.44 and 4.45) as follows:

$$(\mu\nu | \lambda\sigma) = \int \phi_{\mu}(1)\phi_{\nu}(1)\frac{1}{r_{12}}\phi_{\lambda}(2)\phi_{\sigma}(2) d\tau_1 d\tau_2 \quad (4.46)$$

During the calculation of the inter-electronic repulsion integrals, the terms  $(\mu\nu | \lambda\sigma)$  are put equal to zero unless one of the following conditions is satisfied:

- 1)  $\mu = \nu$  and  $\lambda = \sigma$ , or
- 2)  $\mu = \lambda$  and  $\nu = \sigma$  and  $\mu$  and  $\nu$  are centered on the same atom.

These simplifications bring about an immense reduction of the calculation time needed compared to the *ab initio* method.

Furthermore, the terms of the Hartree-Fock matrix are expressed as functions of the semi-empirical Slater Condon factors. These parameters are determined in a fashion to optimize the correspondence of the calculated values to the experiment. The coulomb integrals are calculated according to the Mataga-Nishimoto formula<sup>76</sup>.

The energy corresponding to a singlet-singlet transition between pure configurations is given by<sup>75</sup>:

$$\Delta E_{ij} = \epsilon_j - \epsilon_i - J_{ij} + 2 K_{ij} \quad (4.47)$$

and for a singlet-triplet transition:

$$\Delta E_{ij} = \epsilon_j - \epsilon_i - J_{ij} \quad (4.48)$$

where

$\epsilon_k$  is the orbital energy of the orbital  $k$

$J_{kl}$  and  $K_{kl}$  are defined in eq. 4.44 and 4.45

The singlet to triplet splitting is thus given by  $2 K_{ij}$ .

This method has been widely used for calculating the electronic spectra of organic molecules. Pople and Segal<sup>77-80</sup> had made major contributions to the development of the CNDO (Complete Neglect of Differential Overlap) method, in which also the one centered exchange integrals are neglected and which formed the

first all-valence electron semiempirical method before INDO. The difference between INDO and CNDO allows INDO to take into account spin correlation effects.

The INDO method is known to yield systematically too high estimations of the singlet excited states. But since these overestimations are systematic, effects of derivatives within a class of similar molecules are in general well reproduced. Thus the relevant results from these calculations are the variations upon modifications of the molecules, rather than the absolute data.

Zerner has applied the INDO method and calculated for 1 ring aromatic molecules the excitation energies for the first singlet<sup>75</sup> and triplet<sup>81</sup> states, and extended the INDO method to transition metal complexes<sup>82</sup>. Mizuguchi<sup>7</sup> has calculated the optical absorption spectra of DPP, DTPP and DPPP and hydrogen bonding effects<sup>8</sup> using the INDO/S, CNDO/S and PPP methods. Adachi et al.<sup>9</sup> has studied the red shift of DPP in the solid state using INDO. Pressure and effects of geometry<sup>83</sup> were also studied with INDO.

#### 4.5.1.2. *Method used for geometry optimization*

The geometry of the molecules were optimized with the AM1 method implemented in the program package MOPAC. AM1 is a reparametrized version of the MNDO method which is based on the same concepts as INDO, but uses less drastic approximations. MNDO itself is based on the NDDO method (Neglect of Diatomic Differential Overlap). NDDO consists of neglecting the terms  $(\mu\nu | \lambda\sigma)$  (see eq. 4.46 above) except for the cases if

- the couples  $\mu, \nu$  and  $\lambda, \sigma$  are centered on the same atom respectively and
- $(\mu\nu | \lambda\sigma)$  is one of the following:
  - $(\mu\mu | \nu\nu)$
  - $(\mu\nu | \mu\nu)$
  - $(\lambda\lambda | \sigma\sigma)$
  - $(\lambda\sigma | \lambda\sigma)$
  - $(\mu\nu | \lambda\sigma)$
  - $(\mu\mu | \lambda\sigma)$
  - $(\mu\nu | \lambda\lambda)$

MNDO then further simplifies the calculations by introducing experimental values for the monocentric integrals and calculating bielectronic integrals using a multipole development. AM1 is a refinement of the original MNDO parameters. MOPAC allows the choice between different search methods for the energy minima. EF (Eigenvector Following) yielded the best results, as suggested by the manual text<sup>84</sup>.

This method uses less drastic approximations than the INDO method cited above. But the parametrizations are optimized for the ground state calculations, not for excited state calculations. For this reason MOPAC is preferred for geometry optimization of the ground state but not appropriate for the calculation of the electronic spectra.

For the geometry optimizations the molecules were pre-optimized with classical mechanics methods by the program Molecular Mechanics unless the crystal coordinates were available.

#### 4.5.2. Results and discussion

DPP and various derivatives were treated with the above mentioned methods. The geometries were optimized with MOPAC starting from the crystal structure in the cases of DPP and DMDPP<sup>85</sup> or from the molecular structure obtained by the Molecular Mechanics program using MM2 parameters, based on purely classical interaction forces. It was preferred to optimize the molecular structures with MOPAC even though the crystal structures were available for DPP and DMDPP in order to ensure to compare all molecules in a solution environment optimized conformation.

##### 4.5.2.1. Geometries

The geometries of DPP and DMDPP were taken from their crystalline data<sup>85</sup>. Since the molecules in the crystal lattice are subject to constraints that do not exist in solution, the geometries are expected to be different in the two cases. In order to approach the solution conformations, the geometries of DPP and DMDPP were optimized using MOPAC. This allows also direct comparison to the data of DMADPP and DPADPP, for which the crystal structure was not available. Their geometries were optimized first using a molecular mechanics program and then using MOPAC with the same parameters as for DPP and DMDPP.

Indeed the geometries found by MOPAC differ from the crystal conformation. The main difference is found in the phenyl twisting angle and in the bond lengths of the amide group of the pyrrole ring. The phenyl twisting has already been pointed out by Mizuguchi<sup>7</sup>. *In solution the molecules are not subject to the stacking effects and the phenyl rings are allowed to turn out of the molecular plane. The decreased twisting of the phenyl rings contributes to the bathochromic shift in the absorption spectrum of the solid state.*

*In order to quantify this effect in the case of DPP, the energy variation due to the phenyl ring twisting has been calculated. The energy surface is presented in fig.*

4.29. The energy variation is small within 1.6 kcal mol<sup>-1</sup> or 3 kT between the equilibrium geometry and the extreme angles of 40° chosen for this calculation. In the range of -20° to +20° the energy variation is even less than kT. One could therefore expect not only the geometry found in the crystal but a thermal distribution of the dihedral angle positions in the gas phase or solution.

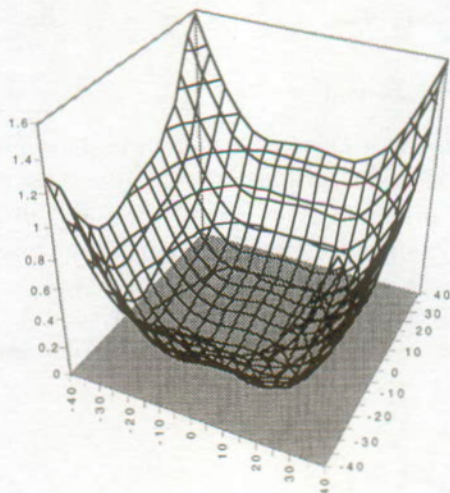


Fig. 4.29: Energy surface of DPP as a function of the phenyl ring twisting. Energy units are kcal/mol. The geometry is based on the crystal conformation of the molecule. The phenyl ring were twisted in 10° steps while the rest of the geometry was maintained rigidly.

The phenyl rings were then forced to different twisting angles in a symmetric way. For each angle the absorption spectrum was calculated using the INDO/S method. The variation of the  $S_1 \leftarrow S_0$  excitation is presented in fig. 4.30.

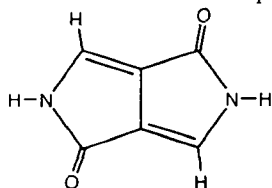


Fig. 4.30: Variation of the excitation energy for the first singlet excited state of DPP as a function of the dihedral angles of the phenyl rings.

angle [°]	E [cm <sup>-1</sup> ]	λ [nm]
0	23567	424.3
6.9	23612.5	423.5
10	23657	422.7
17	23829	419.3
20	23943	417.7
25	24161	413.9
30	24427.3	409.4
40	25077	398.8
50	25831.8	387.1
60	26609	375.8
70	27340.9	365.8
80	27819.8	359.5

Table 4.9: Variation of the excitation energy for the first singlet excited state of DPP.

The variation of the excitation energy for the first singlet excited state is only weak for the dihedral angles around the crystalline geometry (6.9°). For angles tending towards 90° the excitation energy tends towards the value obtained for the DPP molecule where the phenyl rings were substituted by hydrogens, DPPH.



DPPH

For this molecule an excitation energy of 28385 cm<sup>-1</sup> was calculated. The hypsochromic shift is due to the decrease of the  $\pi$ -overlap of the phenyl ring orbitals with the orbitals of the pyrrolo-pyrrole core of the molecule. The variation of the dihedral angle of 6.9° in the crystal lattice to 17.2° in the gas phase as found by MOPAC in agreement with Mizuguchi<sup>7</sup>

does not explain the total bathochromic shift observed on going from the solution to the solid state, but it explains a shift of about 4 nm. This is in the same order as the

effect due to hydrogen bonding described by Adachi et al.<sup>9</sup>. Their results explain a shift of 6 nm in the case of the hydrogen bonded dimer and 7 nm in the case of the linear hydrogen bonded trimer. The hydrogen bonds remain the same in the cases of DPP and PCD, but the stacking is different. In the case of PCD the overlaps<sup>86</sup> due to stacking are smaller than in the case of DPP and thus the spectral shift due to stacking is expected to be weaker.

The influence of the phenyl ring twisting angle on the spectrum and the temperature activated variation of this angles are in agreement with the observation of a hypsochromic shift of the absorption spectrum upon heating the solution<sup>14</sup>.

#### 4.5.2.2. *Electronic spectra and shapes of molecular orbitals*

The electronic spectra were calculated with the INDO/S method as described above. The results are given in table 4.10. For comparison to other molecules the excitation energies of perylene tetracarboxylic di-imide (PTCDI) was calculated in the similar way as for the DPP derivatives. Unfortunately the di-tert-butyl-N,N'-di-phenyl PTCDI, which has a singlet energy and a singlet to triplet energy splitting similar to DPP, could not be treated with ZINDO, since the atom number exceeds the allowed maximum of the program. DPADPP denotes the di-phenyl-amino-DPP analog of DMADPP. It has been proposed on the basis of the results obtained for DMADPP, for which it forms the logical extension. The di-phenyl-amino group is expected to increase the variations observed for DMADPP with respect to DPP. The expected tendency of red-shift due to the strong donor character of the di-phenyl-amino group is clearly evidenced (table 4.10). This molecule offers an interesting potential of color shift for the DPP family. Its singlet to triplet splitting is further decreased in more than the proportional value of the singlet excitation red-shift. Taking into account the spread between the computational and experimental data, the singlet to triplet energy difference is expected to be well below the excitation energy of singlet oxygen, thus eliminating this initiator path for the degradation. Moreover, the di-phenyl-amino groups attached to the phenyl ring of DPP form two tri-phenyl-amine units which are well known among the hole conducting organic materials<sup>87,88</sup>. DPADPP is therefore expected to have interesting hole conducting properties combined with an absorption spectrum reaching far into the red part of the spectrum. These qualities make it a candidate molecule for the application as a photoreceptor or in photovoltaic devices.

compound	$E_{00}^S$ [cm <sup>-1</sup> ]	$\lambda_{00}$ [nm]	$E_{00}^T$ [cm <sup>-1</sup> ]	$E_{00}^S - E_{00}^T$ [cm <sup>-1</sup> ]
DPP	24434	409	9422	15012
DMDPP	24576	407	9699	14878
DMADPP	22298	448	10548	11750
DPADPP	18626	536	8672	9954
PTCDI	22204	450	11375	10829

**Table 4.10:** excitation energies calculated by ZINDO.  $E_{00}^S$ : excitation energies for the first singlet state.  $E_{00}^T$ : excitation energy for the first triplet state.  $E_{00}^S - E_{00}^T$ : singlet to triplet splitting.

Inspection of table 4.10 shows that DPP has a remarkably high singlet to triplet energy lowering. These results were also found in the experimental measurement of the singlet and triplet energies. In order to rationalize this effect, the electron densities of the molecular orbitals of the HOMO and LUMO were calculated. The results are represented in the figures 4.31, 4.32, 4.33, 4.34. The surfaces represent the locations where the amplitude of the wavefunction have a constant value. For the four molecules different values were chosen for clarity of presentation. For the more centered orbitals, higher isosurface values were chosen.

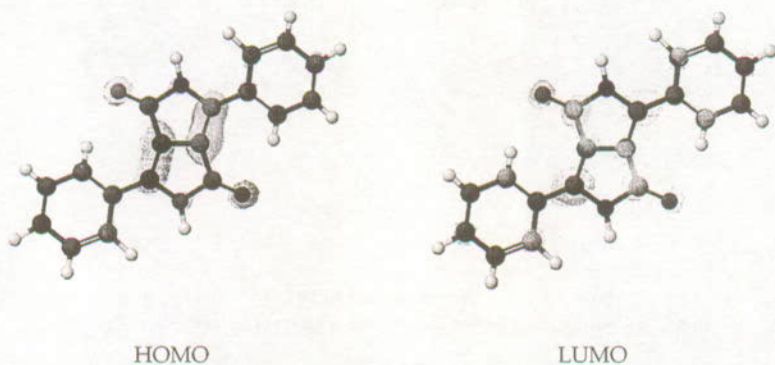


**Fig. 4.31:** HOMO and LUMO frontier orbitals of DPP according to the INDO/S method. The isosurfaces are drawn where the amplitude of the wavefunction is 0.05.



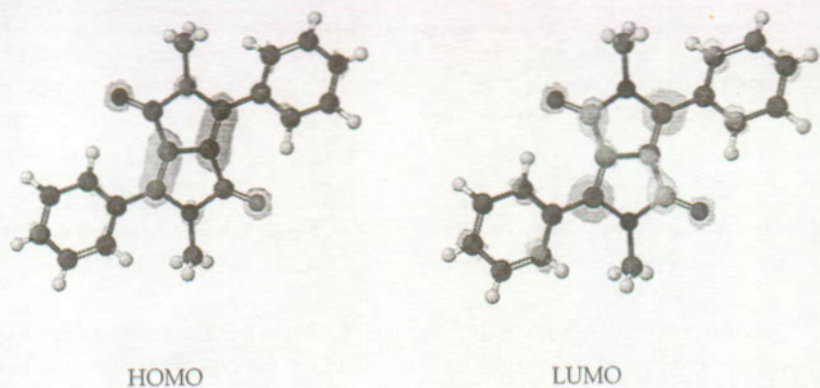


Fig. 4.32: HOMO and LUMO frontier orbitals of DMDPP according to the INDO/S method. The isosurfaces are drawn where the amplitude of the wavefunction is 0.05.

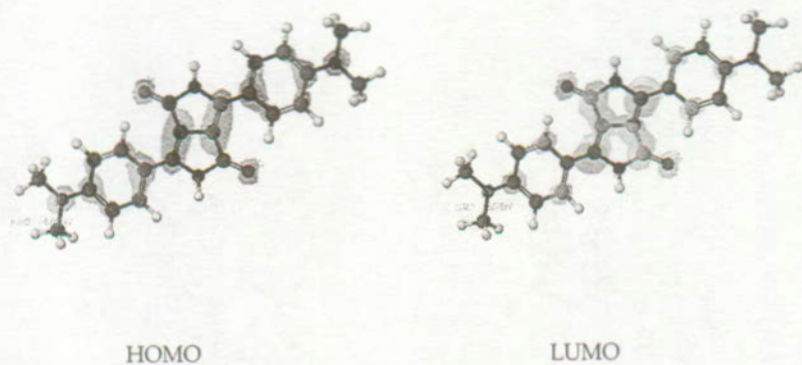
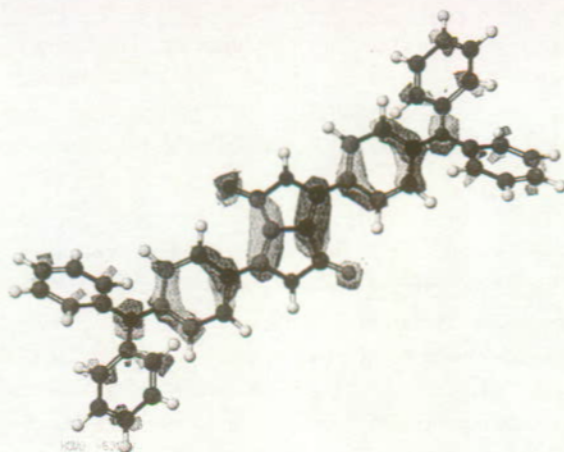
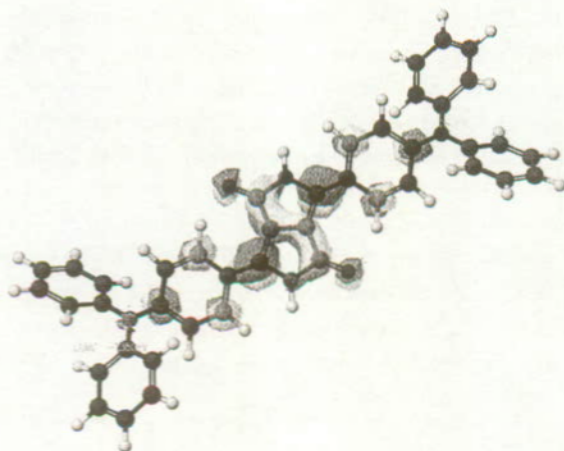


Fig. 4.33: HOMO and LUMO frontier orbitals of DMADPP according to the INDO/S method. The isosurfaces are drawn where the amplitude of the wavefunction is 0.04.



HOMO



LUMO

Fig. 4.34: HOMO and LUMO frontier orbitals of DPADPP according to the INDO/S method. The isosurfaces are drawn where the amplitude of the wavefunction is 0.03.

The orbital shapes show, that both on DPP and DMDPP, the HOMO and the LUMO are strongly concentrated in the core part, the di-pyrrolo-pyrrole, of the molecule. The phenyl ring electron density contributes a minor part to these orbitals. This is confirmed experimentally by the fact that the various substitutions on the

para position on the phenyl ring do not significantly influence the absorption spectrum. However, the meta positions do, since by steric interaction with the dipyrrolo-pyrrole part they force the phenyl rings out of plane. The same effect happens in the case of the N-methylation in DMDPP. The absorption spectrum loses the vibrational structure. The  $E_{00}$  excitation energy however is not changed significantly.

In the DMADPP molecule, the dimethyl-amino group changes the distribution of the HOMO electron density, increasing the contribution of the phenyl rings. This leads to an increased delocalization of the HOMO. The LUMO however is even more concentrated on the central part of the molecule.

The calculated transitions after CI are nearly pure HOMO to LUMO transitions in all derivatives. The discussion of the ground and first excited states may therefore be restricted to these two orbitals. The large singlet-to-triplet energy splitting of DPP may now be explained by the large overlap of the HOMO and LUMO on the carbon atoms 4 and 16 and between the neighboring atoms 15 and 16 and 4 and 19 respectively. These overlaps do not vary significantly between DPP and DMDPP. However in DMADPP the HOMO is less concentrated on these carbon atoms, even though the LUMO remains concentrated. The overlap thus decreases, and the singlet to triplet energy splitting decreases as well, as the calculations show. The same effect has been observed in the experimental determination of the triplet energies above.

A similar effect has been found by Beljonne et al.<sup>89</sup> for oligothiophenes. Based on configuration interaction calculations and on experimental evidence from absorption spectra they found that the evolution of the  $S_0 \longrightarrow T_1$  energy is much slower than that of the  $S_0 \longrightarrow S_1$  excitation. The singlet-triplet energy difference is only lowered by 0.2 eV compared to a lowering of 1.4 eV for the singlet-singlet absorption. This effect is attributed to the more localized character of triplet state. The extension of the triplet state over not more than one ring had been confirmed by Optically-Detected Magnetic Resonance<sup>90</sup>.

## 4.6. Conclusion

It has been shown that the monomers of DPP and its derivatives have excited state energies that allow the sensitization of singlet oxygen which subsequently reacts with the dye leading to degradation. The singlet-to-triplet energy splitting is large for this class of compound and is a property of the core part on the pyrrolo-pyrrole of the molecule, where the LUMO has a high electron density. It may be influenced by changing the electron density of the HOMO in the core part of the molecule by the addition of donor substituents, contributing to the HOMO far from the pyrrolo-pyrrole core.

The NILES compounds may have an ambiguous effect on the monomer by deactivating the singlet state but enhancing the intersystem crossing yielding triplet excited states, which sensitize singlet oxygen. Singlet oxygen is then quenched again by the nitroxyl compounds. The stabilizing effect of NILES may therefore be limited, since its singlet quenching efficiency has to be accompanied by a even higher singlet oxygen quenching efficiency. Singlet oxygen quenchers that do not interact with the singlet excited state of DPP to enhance the triplet yield would be preferable. From the ability of  $^1\text{DPP}^*$  to sensitize singlet oxygen, stabilizers should quench  $^1\text{DPP}^*$  vibronically. Substituents such as hydroxyl groups could stabilize the molecules as they act as an efficient energy dump and shorten the excited state lifetimes. This is in agreement with the observed large increase of the stability of the compound in the solid state.

## 4.7. References

- (1) Chassot, L. *Chimia* **1994**, *48*, 432-435.
- (2) CIBA "internal report," Ciba, 1990.
- (3) Bellus, D.; Lind, H.; Wyatt, J. F. *J. Chem. Soc. Chem. Commun.* **1972**, *1972*, 1199-1200.
- (4) Bellus, D. In *Singlet Oxygen*; B. Ranby and J. F. Rabek, Eds.; John Wiley & Sons: Chichester, 1978.
- (5) Mizuguchi, J.; Wooden, G. *Ber. Bunsenges. Phys. Chem.* **1991**, *95*, 1264-1274.
- (6) Mizuguchi, J.; Rochat, A. C. *Ber. Bunsenges. Phys. Chem.* **1992**, *96*, 708-11.
- (7) Mizuguchi, J. *Ber. Bunsenges. Phys. Chem.* **1993**, *97*, 693-701.
- (8) Mizuguchi, J. *Ber. Bunsenges. Phys. Chem.* **1994**, *98*, 28-34.
- (9) Adachi, M.; Nakamura, S. *J. Phys. Chem.* **1994**, *98*, 1796-1801.
- (10) Reichardt, C. *Solvents and solvent effects in organic chemistry*; VCH: Weinheim, 1988.
- (11) Lide, D. R. *CRC Handbook of chemistry and physics*; 73 ed.; CRC: Boca Raton, 1992-1993.
- (12) Murov, S. L.; Carmichael, I.; Hug, G. L. *Handbook of Photochemistry*; 2 ed.; Dekker: New York, Basel, 1993.
- (13) Strickler, S. J.; Berg, R. A. *J. Chem. Phys.* **1962**, *37*, 814.
- (14) Mizuguchi, J.; Rihs, G. *Ber. Bunsenges. Phys. Chem.* **1992**, *96*, 597-606.
- (15) Mizuguchi, J.; Rochat, A. C.; Rihs, G. *Ber. Bunsenges. Phys. Chem.* **1992**, *96*, 607-619.
- (16) Scaiano, J. C. *Handbook of Organic Photochemistry*; CRC Press: Boca Raton, 1989.
- (17) Oliveros, E.; Murasecco-Suardi, P.; Braun, A. M.; Hansen, H. J. *Meth. Enzym.* **1992**, *213*.
- (18) Murasecco-Suardi, P.; Oliveros, E.; Braun, A. M.; Hansen, H.-J. *Helv. Ch. Acta* **1988**, *71*, 1005-1010.
- (19) Oliveros, E.; Suardi-Murasecco, P.; Aminian-Saghafi, T.; Braun, A. M. *Helv. Ch. Acta* **1991**, *74*, 79-90.
- (20) Olea, A. F.; Wilkinson, F. *J. Phys. Chem.* **1995**, *99*, 4518-4524.
- (21) Stevens, B. In *Singlet Oxygen*; B. Ranby and J. F. Rabek, Eds.; John Wiley & Sons: Chichester, 1978; pp 54-60.
- (22) Gilbert, A.; Baggott, J. *Essentials of Molecular Photochemistry*; Blackwell Scientific Publications: Oxford, 1991.
- (23) Birks, J. B. *Photophysics of aromatic molecules*; 1 ed.; Wiley Interscience: London, 1970.

- (24) Scurlock, R. D.; Wang, B.; Ogilby, P. R.; Sheats, J. R.; Clough, R. L. *J. Am. Chem. Soc.* **1995**, *117*, 10194-10202.
- (25) Braun, A. M.; Maurette, M.-T.; Oliveros, E. *Technologie Photochimique*; Presses Polytechniques Romandes: Lausanne, 1986.
- (26) Wilkinson, F. In *Singlet Oxygen*; B. Ranby and J. F. Rabek, Eds.; John Wiley & Sons: Chichester, 1978; pp 36-47.
- (27) Maurette, M.-T.; Oliveros, E.; Infelta, P. P.; Ramsteiner, K.; Braun, A. M. *Helv. Ch. Acta* **1983**, *66*, 722-733.
- (28) Daraio, M. E.; Aramendia, P. F.; Roman, E. S. *J. Photochem. Photobiol. A: Chem.* **1994**, *77*, 41-48.
- (29) Haag, W. R.; Hoigné, J.; Gassman, E.; Braun, A. M. *Chemosphere* **1984**, *13*, 631.
- (30) Graf, G. A.; Braun, A. M.; Faure, J. *Chimia* **1980**, *34*, 234.
- (31) Foote, C. S.; Wuesthoff, M. T.; Wexler, S.; Burstain, I. G.; Denny, R.; Schenck, G. O.; Schulte-Elte, K. H. *Tetrahedron* **1967**, *23*, 2583-2599.
- (32) Roitman, L.; Ehrenberg, B.; Kobayashi, N. *J. Photochem. Photobiol. A: Chem.* **1994**, *77*, 23-28.
- (33) Matheson, I. B. C.; Lee, J. *Chem. Phys. Lett.* **1970**, *7*, 475-476.
- (34) Farmilo, A.; Wilkinson, F. *Photochem. Photobiol.* **1973**, *18*, 447-450.
- (35) Meites, L.; Zuman, P. *CRC Handbook of electrochemistry*; CRC Press Inc.: Cleveland, 1976.
- (36) Gosser, D. K. *Cyclic voltammetry*; VCH Publishers, Inc.: New York, 1993.
- (37) Haag, W. R.; Mill, T. *Photochem. Photobiol.* **1987**, *45*, 317.
- (38) Spikes, J. D.; Bommer, J. C. *J. Photochem. Photobiol. B: Biol.* **1993**, *17*, 135-143.
- (39) Harbour, J. R.; Issler, S. L. *J. Am. Chem. Soc.* **1982**, *104*, 903.
- (40) Bianchi, G. In *Chemistry of Functional Groups*; S. Patai and Z. Rappaport, Eds.; Wiley: New York, 1983; pp 752.
- (41) Padwar, A. *1,3-Dipolar Cycloaddition Chemistry*; Wiley: New York, 1984; Vol. 1 & 2.
- (42) Huisgen, R. In *Chemistry of Alkenes*; S. Patai, Ed. New York, 1964; Vol. 1; pp 806.
- (43) Ford, W. E.; Kamat, P. V. *J. Phys. Chem.* **1987**, *91*, 6373-6380.
- (44) Méallier, P.; Gudefin, A.; Ehlinger, N.; Perrin, M. *Dyes and Pigments* **1996**, *31*, 13-17.
- (45) Naguib, Y. M. A.; Steel, C.; Cohen, S. G.; Young, M. A. *J. Photochem. Photobiol. A: Chem.* **1996**, *96*, 149-154.
- (46) Saupp, U. Thesis, Universität Stuttgart, 1992.
- (47) Ng, H. C.; Guillet, J. E. In *Singlet Oxygen*; B. Ranby and J. F. Rabek, Eds.; John Wiley & Sons: Chichester, 1978; pp 278-281.
- (48) Chattopadhyay, S. K.; Das, P. K.; Hug, G. L. *J. Am. Chem. Soc.* **1983**, *105*, 6205-6210.

- (49) Rivail, J.-L. *Elements de Chimie Quantique à l'usage des chimistes*; 2 ed.; InterEditions: Paris, 1994, pp 435.
- (50) Atkins, P. W. *Molecular Quantum Mechanics*; 2 ed.; Oxford University Press: Oxford, 1983.
- (51) Kalyanasundaram, K. *Photochemistry in microheterogeneous systems*; Academic Press Inc.: Orlando, 1987, pp 388.
- (52) Chattopadhyay, S. K.; Das, P. K.; Hug, G. L. *J. Am. Chem. Soc.* **1982**, *104*, 4507-4514.
- (53) Sandros, K. *Acta Chemica Scandinavica* **1964**, *18*, 2355-2374.
- (54) Carmichael, I.; Hug, G. L. *Journal of Physical and Chemical Reference Data* **1986**, *15*, 1-250.
- (55) Ermolaev, V. L. *Opt. Spectrosc.* **1959**, *6*, 417.
- (56) Dexter, D. L. *J. Chem. Phys.* **1953**, *21*, 836-850.
- (57) Braun, A. M.; Murasecco-Suardi, P.; Gassmann, E.; Oliveros, E. *Helv. Ch. Acta* **1987**, *70*, 1760-1773.
- (58) Loutfy, R. O.; Sharp, J. H. *Photogr. Sci. Eng.* **1976**, *20*, 165.
- (59) Bard, A. J.; Faulkner, L. R. *Electrochemical Methods, Fundamentals and Applications*; John Wiley & Sons: New York, 1980, pp 718.
- (60) Herkstroeter, W. G.; Lamola, A. A.; Hammond, G. S. *J. Am. Chem. Soc.* **1964**, *86*, 4537-4540.
- (61) Sauv e, G.; Kamat, P. V.; Ruoff, R. S. *J. Phys. Chem.* **1995**, *99*, 2162-2165.
- (62) Herkstroeter, W. G. *J. Am. Chem. Soc.* **1975**, *97*, 4161-4167.
- (63) Kawaoka, K.; Khan, A. U.; Kearns, D. R. *J. Chem. Phys.* **1967**, *46*, 1842-1853.
- (64) Patterson, L. K.; Porter, G.; Topp, M. R. *Chem. Phys. Lett.* **1970**, *7*, 612-614.
- (65) Atkins, P. W. *Physical Chemistry*; 4 ed.; W.H. Freeman and Company: New York, 1990.
- (66) Atik, S. S.; Kwan, C. L.; Singer, L. A. *J. Am. Chem. Soc.* **1979**, *101*, 5696-5702.
- (67) Atik, S.; Singer, L. A. *J. Am. Chem. Soc.* **1978**, *100*, 3234-3235.
- (68) Green\_II, J. A.; Singer, L. A. *J. Am. Chem. Soc.* **1974**, *96*, 2730-2733.
- (69) Watkins, A. R. *Chem. Phys. Lett.* **1974**, *29*, 526-528.
- (70) Gijzeman, O. L. J.; Kaufman, F.; Porter, G. *J. Chem. Soc. Faraday. Trans.* **1973**, *69*, 727-737.
- (71) Green, S. A.; Simpson, D. J.; Zhou, G.; Ho, P. S.; Bough, N. V. *J. Am. Chem. Soc.* **1990**, *112*, 7331-7346.
- (72) Green, J. A. I.; Singer, L. A.; Parks, J. H. *J. Chem. Phys.* **1973**, *58*, 2690-2695.
- (73) Srivatsavoy, V. J. P.; Eschle, M.; Moser, J.-E.; Gr tzel, M. *J. Chem. Soc. Chem. Commun.* **1995**, 303.
- (74) F rster, T. *Annalen der Physik* **1948**, *6*, 55-75.
- (75) Zerner, M.; Ridley, J. *Theoretical Chemica Acta* **1973**, *32*, 11-134.

- (76) Nishimoto, K.; Mataga, N. *Z. Phys. Chem.* **1957**, *12*, 335-338.
- (77) Pople, J. A.; Segal, G. A.; Santry, D. P. *J. Chem. Phys.* **1965**, *43*, S129.
- (78) Pople, J. A.; Segal, G. A. *J. Chem. Phys.* **1965**, *43*, S136.
- (79) Pople, J. A.; Segal, G. A. *J. Chem. Phys.* **1966**, *44*, 3289.
- (80) Santry, D. P.; Segal, G. A. *J. Chem. Phys.* **1965**, *47*, 158.
- (81) Ridley, J. E.; Zerner, M. C. *Theoretical Chemica Acta* **1976**, *42*, 223-236.
- (82) Bacon, A. D.; Zerner, M. C. *Theoretical Chemica Acta* **1979**, *53*, 21-54.
- (83) Adachi, M.; Yoneyama, M.; Nakamura, S. *Langmuir* **1992**, *8*, 2240-2246.
- (84) Stewart, J. J. P. *MOPAC Manual*; 6 ed.; Frank J. Seiler Research Laboratory, United States Air Force Academy, Colorado: 1990.
- (85) Mizuguchi, J.; Grubenmann, A.; Wooden, G.; Rihs, G. *Acta Crystallogr. Sect. B* **1992**, *b48*, 696-700.
- (86) Mizuguchi, J.; Grubenmann, A.; Rihs, G. *Acta Crystallogr. Sect. B* **1993**, *B49*, 1056-1060.
- (87) Shirota, Y.; Kobata, T.; Noma, N. *Chem. Lett.* **1989**, 1145-1148.
- (88) Shirota, Y.; Kuwabara, Y.; Inada, H. *Appl. Phys. Lett.* **1994**, *65*, 807-809.
- (89) Beljonne, D.; Cornil, J.; Friend, R. H.; Janssen, R. A. J.; Brédas, J. L. *J. Am. Chem. Soc.* **1996**, *118*, 6453-6461.
- (90) Swanson, L. S.; Shinar, J.; Yoshino, K. *Phys. Rev. Lett.* **1990**, *65*, 1140-1143.



# 5. Electrical and photovoltaic properties of solid state DPP and derivatives

## 5.1. Introduction

Organic hole conductors (*p*-type organic semiconductors) have found various applications where large areas and cheap materials with moderate conductivity properties are needed. Applications such as electrostatic protection coatings or radar absorbing materials<sup>1</sup>, rechargeable batteries<sup>2</sup>, electrochromic windows<sup>2</sup>, polymer transistors<sup>3</sup> have been investigated. However the main application today is electrophotography<sup>4,5</sup> where organic materials act as photosensitive receptors or carrier (electron or hole) transporting materials. This is also one electronic application where polymers are superior to inorganic semiconductors<sup>5</sup>.

Generally organic photoconductive materials are either polymers or amorphous materials. Photoconductive polymers can be classified into the following categories based on their structures:

- polymers with pendent groups
- molecularly doped polymers (polymer blends)
- backbone conjugated polymers
- nanocluster composites

Non polymeric organic materials are generally used as hole or electron conductors in their amorphous state. In microcrystalline systems deep traps are supposed to deteriorate the mobility of the charge carriers. In fact, the transition from molecularly doped polymers to pure materials has been studied for different materials<sup>6</sup> and the mobilities are found to be maximum for the amorphous pure materials<sup>5</sup>. For industrial applications however, the crystallization process is difficult to prevent for pure amorphous materials. Polymer blends are therefore preferred for their stability and physical properties allowing to cast large surfaces. Recently liquid crystals have gained increased interest since their conductivity range has become competitive with polymeric materials<sup>7,8</sup> and further work is pursued to imbed them in matrices that allow the construction of mechanically stable thin films.

Microcrystalline materials have been used as hole conductors in spite of the above mentioned drawbacks. Kassi<sup>9</sup> has measured the hole mobility in a microcrystalline chlorophyll *a* layer using the theory of Scher and Montroll<sup>10,11</sup> and found that the transport mechanism follows the disorder formalism proposed by Bässler et al.<sup>12</sup>. Kontani<sup>13</sup> has measured the mobility of TiO-phthalocyanine for different substrate crystallinities from amorphous to 30 nm sized microcrystalline domains and found the mobility to increase from  $2 \cdot 10^{-6}$  V cm s<sup>-2</sup> for amorphous to  $2 \cdot 10^{-5}$  V cm s<sup>-2</sup> for microcrystalline layers .

Many attempts were made to build solid state organic solar cells. Most systems used sandwich structures consisting of one organic material forming a Schottky barrier with one of the contacting metals<sup>14-17</sup>, two organic layers forming a p-n heterojunction<sup>18-20</sup>, mixed layers of interpenetrating microdomains<sup>21,22</sup> or interpenetrating one dimensional molecular networks<sup>23</sup>. Interpenetrating systems offer the main advantage that excitations produced by the absorbed photons need to travel only short distances to reach an interface where they separate most efficiently into a positive hole and a negative electron. Since the exciton separation step is one of the limiting steps in many systems<sup>17,23</sup> and exciton mean free paths are generally short compared to the layer thickness needed to absorb all the light, in the order of 80Å for merocyanines<sup>17</sup>, 2700Å for perylenes<sup>24</sup> and 200-400Å for phthalocyanines<sup>4</sup>, interpenetrating systems may overcome this limitation. However, additional complexity arises in heterogeneous media from the charge carrier transport due to ill-defined local fields and discontinuities of the *p*- and *n*-phases and recombination and excitation disexcitation. These effects lower the observed quantum yields. A third approach is to use dye sensitized heterojunctions as a solid state analog of the liquid electrolyte containing photoelectrochemical cell<sup>25,26</sup> discussed in the previous chapter. Encouraging results have been reported by Tennakone<sup>27</sup> and O'Regan<sup>28,29</sup>.

Derivatives of DPP and especially its sulfur derivative DTPP<sup>30-32</sup> have been reported as photoconductors for electrophotography or data storage systems<sup>30,33,34</sup> and the application for solar cells has been suggested<sup>35</sup>. The dark conductivity and the observation of photoconductivity have been reported by Mizuguchi<sup>31,35,36</sup> and the effect of solvent vapor treatment on the photoconductivity has been shown. Solvent vapor treatment effects have also been reported to have a beneficial effect on the photovoltaic performance of perylenes<sup>37</sup>.

*In the following the conductivity of DMADPP will be investigated and DPP and DTPP will be applied as a hole conductor in solid state solar cells of different structures based on TiO<sub>2</sub>. Recognizing the fact that the interface between the n- and p-type semiconductor plays a crucial role, MCDPP (Mono Carboxylated DPP), a derivative of DPP, has been*

*synthesized to allow the attachment of the molecule onto TiO<sub>2</sub>. Its performance in a photoelectrochemical cell (PEC) has been tested. Finally Surface photovoltage spectroscopy (SPS)<sup>38,39</sup> of evaporated layers allows to give some insight in the band structure of the solid state solar cells.*

## **5.2. Heterogeneous charge injection from DPP derivatives adsorbed on TiO<sub>2</sub>**

In spite of the fact that DPP is known as a pigment<sup>40</sup> and a thin film photoconductor<sup>31,41</sup> and exhibits its distinguishing qualities in the solid state, its properties as a molecular sensitizer will be investigated in the following and demonstrated in a dye sensitized (Grätzel type) photoelectrochemical cell<sup>25,42</sup>. This allows to separate the study of the charge injection step and the charge transport in the bulk. The spectral range of the absorption of DPP is not optimal for an application in a dye sensitized solar cell, but the ability to inject electrons from the excited state from the molecule into the conduction band of TiO<sub>2</sub> is an important condition for its potential application as a molecular or a solid state sensitizer as the potential difference between the excited state of the dye and the bottom of the conduction band has to offer enough driving potential for the electron transfer and the electronic coupling of the dye to the TiO<sub>2</sub> has to be sufficient. Sensitization with organic dyes has been demonstrated in various works for TiO<sub>2</sub><sup>43-46</sup> and with organometallic complexes<sup>25,42,47-49</sup> or for ZnO<sup>50</sup>. For a good coupling to the TiO<sub>2</sub> surface involving  $\pi$ -orbital overlap the electron injection is in the femtosecond timescale, as shown for Ru<sup>II</sup>L<sub>2</sub>(NCS)<sub>2</sub><sup>51</sup> and coumarin 343<sup>52</sup>. However the coupling does not need to proceed via  $\pi$ -orbital overlap to the Ti<sup>4+</sup> on the semiconductor surface and is efficient for dyes attached on the semiconductor surface via phosphonate groups<sup>53</sup> or an ethyl carboxylate chain<sup>46</sup>. Slow electron transfer has been demonstrated for eosine-Y<sup>44</sup> reducing the injection efficiency to 40%.

For this study a *N*-acetyl DPP, named MCDPP, has been synthesized according to the procedure described in chapter 2.

### **5.2.1. Adsorption onto TiO<sub>2</sub>**

In order to find the best adsorption conditions for the MCDPP on the TiO<sub>2</sub> surface, the adsorption equilibria were measured using Langmuir isotherms of the adsorption on Degussa P-25 TiO<sub>2</sub> powder. P-25 was chosen for its homogenous

quality and well characterized surface. The BET surface is  $55 \text{ m}^2/\text{g}$  and the particle average diameter is 28 nm. The crystal phase is a mixture of anatase and rutile, whereas anatase accounts for more than 70%. P-25 was added to solutions of different concentrations and the solutions were left over night at room temperature. The particles were then centrifuged and the dye concentrations in the supernatant were determined by absorption measurement.

Adsorption from a DMSO solution yielded an equilibrium constant of  $6.7 \cdot 10^4 \text{ l mol}^{-1}$  and a surface per molecule of  $120 \text{ \AA}^2$ . This is consistent with the coloration of transparent sintered colloidal  $\text{TiO}_2$  films achieved by dipping the films for 1 hr in the dye solution. For these films, which have a surface roughness factor of 1000 due to their high porosity, an absorbance of 2.6 at 490 nm was obtained. The light scattering is negligible on these films and does not increase the apparent absorption, as this is the case for the opaque and highly scattering  $\text{TiO}_2$  electrodes. Using the extinction coefficient of  $\epsilon_{490\text{nm}} = 19500 \text{ l mol}^{-1} \text{ cm}^{-1}$  for MCDPP this coloration is consistent with the molecular area of  $120 \text{ \AA}^2$  and a totally covered surface. The same result was achieved by adsorption from EtOH.

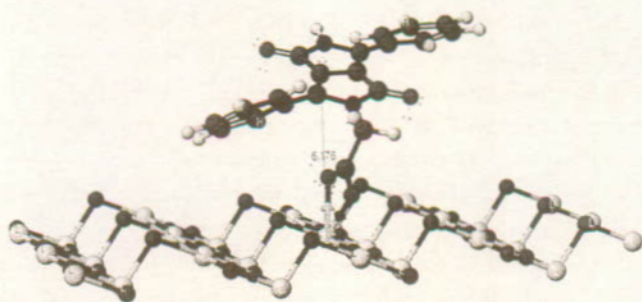


Fig. 5.1: MCDPP on the  $\text{TiO}_2$  anatase (101) surface. Geometry calculated by Molecular Mechanics and MM2 parameters.

The adsorption geometry was calculated using the Molecular Mechanics (MM2) programme of the Tektronix CAChe system. The  $\text{TiO}_2$  surface was taken from crystal data<sup>54</sup> and locked during the geometry optimisation. The carboxyl unit is assumed to coordinate directly to the  $\text{Ti}^{4+}$  ions on the surface and to replace existing hydroxyl groups at the surface<sup>55</sup>. The carboxyl unit coordinates to one  $\text{Ti}^{4+}$  ion, although the

presence of hydroxyl groups as linking bridges can not be completely ruled out. Natural and synthetic crystals of anatase expose the (001) and (111) surface planes<sup>56</sup>. On the colloidal TiO<sub>2</sub> electrodes however, most of the exposed surface is the (101) plane<sup>57,58</sup>. The distance of the center of the molecule to the surface Ti<sup>4+</sup> ions was found to be 6.2Å from the molecular mechanics calculation. The alkyl chain attached on the nitrogen atom is purely  $\sigma$ -bonded and there is no  $\pi$ -orbital link to the Ti<sup>4+</sup> acceptor states for the electron transfer. Moreover, the calculations of the ground and excited state orbital shapes in chapter 4 show that the excited state has the main electron density on the central carbon atoms of the pyrrolo-pyrrole unit, and thus the distance of the molecule center to the Ti<sup>4+</sup> ion describes well the distance of the excited electron to the nearest acceptor state in the semiconductor. Electron transfer in analogous systems with similar electron transfer distances from a dye attached via an acetate chain has been observed by Nüesch<sup>46</sup> and Moser<sup>59</sup> for a merocyanine dye. For this system highly efficient electron injection into TiO<sub>2</sub> has been achieved<sup>60</sup>, whereas the action spectrum shows that the dye forms J-aggregates on the semiconductor surface<sup>61</sup>.

### 5.2.2. Fluorescence quenching on the surface of TiO<sub>2</sub> particles

The adsorption of the dye on colloidal TiO<sub>2</sub> allows to investigate the quenching of the excited state due to charge transfer and concentration or aggregation effects<sup>44</sup>. The quenching of the fluorescence due to the adsorption of MCDPP on the surface of TiO<sub>2</sub> particles in a suspension allows to give an upper rate limit for the electron transfer from the excited state of the dye into TiO<sub>2</sub>.

TiO<sub>2</sub> colloids in EtOH were prepared according to the method described by Moser<sup>42</sup> to yield optically transparent suspensions with particles of average diameter of 20 nm. These suspensions are transparent in the visible and were preferred over P-25 suspensions, which are highly scattering, for their optical quality. The fluorescence yield of MCDPP in solution is unity within the experimental error of 5%. For fluorescence yield measurements DPP was used as a standard.

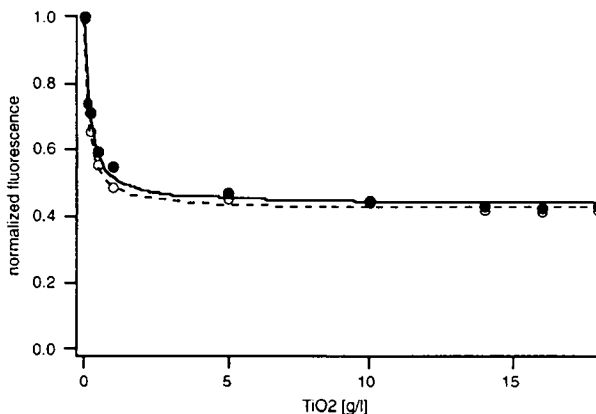


Fig. 5.2: Effect of the concentration of TiO<sub>2</sub> colloidal particles on the fluorescence yield of MCDPP in ethanol. The MCDPP concentration was 10<sup>-6</sup> mol l<sup>-1</sup>. Full circles were measured 15 min. after addition of TiO<sub>2</sub>, open circles were measured after 24 hours.

Figure 5.2 presents on a normalized scale the integrated fluorescence counts of solutions with constant MCDPP concentrations and varying TiO<sub>2</sub> colloid concentrations. The fluorescence yields were measured once 15 min. after the addition of TiO<sub>2</sub> colloids and a second time 24 hours later. No significant changes were observed. The results show that the fluorescence of the adsorbed dye is not completely quenched by electron transfer to the TiO<sub>2</sub> particles, since according to the adsorption equilibrium the concentration of non adsorbed dye is expected to become negligible at TiO<sub>2</sub> particle concentrations above 5 g/l. Therefore residual fluorescence from non adsorbed dye molecules cannot account for the fluorescence observed at higher TiO<sub>2</sub> particle concentrations. The fluorescence is therefore attributed to adsorbed molecules on the TiO<sub>2</sub> surface. Thus the observed fluorescence at different TiO<sub>2</sub> concentrations is the sum of free monomers and adsorbed molecules:

$$f = f_{\text{sol}} \cdot C_{\text{sol}} + f_{\text{ads}} \cdot C_{\text{ads}} \quad (5.1)$$

where:

- $f_{\text{sol}}$  = fluorescence yield of molecules in solution
- $f_{\text{ads}}$  = fluorescence yield of surface adsorbed molecules
- $C_0$  = dye concentration in solution before addition of TiO<sub>2</sub>
- $C_{\text{sol}}$  = dye concentration in solution =  $C_0 - C_{\text{ads}}$
- $C_{\text{ads}}$  = concentration of dye adsorbed on the surface

Assuming that the adsorption equilibrium is established, the data can be used to extract the adsorption equilibrium constant and the relative fluorescence yield  $\frac{f_{\text{ads}}}{f_{\text{sol}}}$  of adsorbed MCDPP.

$C_{\text{ads}}$  follows the adsorption equilibrium described by the Langmuir isotherm

$$\frac{C_{\text{sol}}}{C_{\text{ads}}} = \frac{1}{KN} + \frac{C_{\text{sol}}}{N} \quad (5.2)$$

where

$K$  = adsorption equilibrium constant

$N$  = number of adsorption sites in the solution = colloid surface / surface per molecule

$C_{\text{ads}}$  can thus be expressed as a function of  $N$ :

$$C_{\text{ads}} = - \frac{\left(\frac{1}{K} + C_o - N\right) - \left[\left(\frac{1}{K} - C_o + N\right)^2 + 4 \cdot \frac{C_o}{K}\right]^{\frac{1}{2}}}{2} \quad (5.3)$$

For the fitting the surface per molecule,  $A_m$ , was taken as a fitting parameter and  $C_{\text{ads}}$  could then be fitted to the total  $\text{TiO}_2$  surface of the colloid in the solution:

$$C_{\text{ads}} = - \frac{\left(\frac{1}{K} + C_o - \frac{A_{\text{TiO}_2}}{A_m}\right) - \left[\left(\frac{1}{K} - C_o + \frac{A_{\text{TiO}_2}}{A_m}\right)^2 + 4 \cdot \frac{C_o}{K}\right]^{\frac{1}{2}}}{2} \quad (5.4)$$

The integrated fluorescence as a function of the  $\text{TiO}_2$  colloid concentration was fitted with eq. 5.1 using eq. 5.4. The fitted curves are presented in fig. 5.2. From the fitting the parameters  $K$ ,  $\frac{f_{\text{ads}}}{f_{\text{sol}}}$  and the surface per molecule  $A_m$  are obtained. The best least square fit gave  $K = 3.47 \cdot 10^4 \text{ l mol}^{-1}$ ,  $A_m = 90 \text{ \AA}^2$  and  $\frac{A_{\text{TiO}_2}}{A_m} = 0.43$ . Taking into account that the  $\text{TiO}_2$  colloid used for this experiment is prepared in a different manner than the P-25 used for the Langmuir adsorption isotherms cited above and the change of the solvent these values are consistent with the values obtained from the previous experiments. Fig. 5.3 shows the concentration of unadsorbed dye calculated from eq. 5.4 using the parameters obtained from the previous fit. The figure confirms that above 5 g/l the contribution of unadsorbed dye to the fluorescence is negligible.

The data in fig. 5.2 also show that there is no minimum of fluorescence yield at low  $\text{TiO}_2$  concentrations contrary to what has been observed for the adsorption of eosin Y due to concentration quenching<sup>44</sup>.

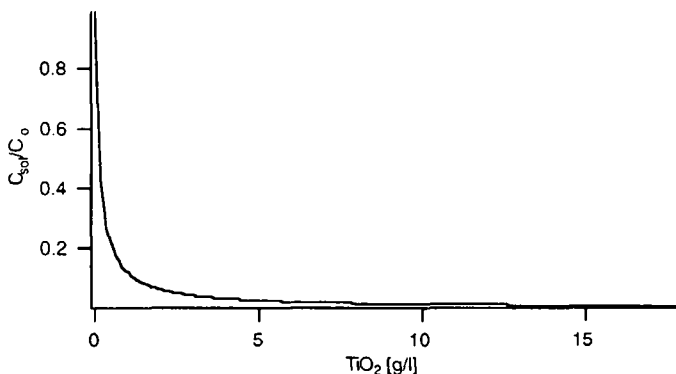


Fig. 5.3: relative concentration of unabsorbed dye calculated using eq. 5.4 and the parameters from the fit to the experimental points in fig. 5.2

From the high residual fluorescence of the monomer on  $\text{TiO}_2$  particles we conclude that the electron injection into  $\text{TiO}_2$  is slow under the present conditions. From transient fluorescence measurements using a 180 ps excitation pulse and an excitation wavelength of 355 nm the radiative lifetime of the excited state was measured as being 11 ns, i.e.  $k_f = 9 \cdot 10^7 \text{ sec}^{-1}$ . We calculate therefore for the electron injection rate constant  $k_{inj}$ :

$$k_{inj} = \frac{1 - \frac{A_{\text{TiO}_2}}{A_m}}{\frac{A_{\text{TiO}_2}}{A_m}} k_f = 1.3 \cdot 10^8 \text{ sec}^{-1}. \quad (5.5)$$

This rate constant is slow indicating weak electronic coupling between excited MCDPP and the acceptor manifold of  $\text{TiO}_2$ . It is nevertheless comparable to the injection rate constant for eosin Y, i.e.  $8.5 \cdot 10^8 \text{ sec}^{-1}$  found by Moser<sup>62</sup>. MCDPP will be used in the following as a molecular sensitizer on  $\text{TiO}_2$  for the photoelectrochemical cell and later as a linking layer in the interface  $\text{TiO}_2/\text{DPP}$ .

### 5.2.3. Photovoltaic electrochemical cell

MCDPP was used as a sensitizer on porous  $\text{TiO}_2$  electrodes in a solar cell setup analogous to the system described by Grätzel and coworkers<sup>25</sup>.  $\text{TiO}_2$  electrodes were prepared following a procedure by Barbé<sup>57</sup>. The thickness of the  $\text{TiO}_2$  layer was 10  $\mu\text{m}$ . The electrodes were then dipped for 30 minutes at room temperature in a  $10^{-2}$



4 mol/l solution of MCDPP in DMSO. The electrolyte used was acetonitrile/ethylenecarbonate in a 1:1 vol. ratio (AN/EC) containing 0.5 mol/l LiI and  $3 \cdot 10^{-2}$  mol/l  $I_2$  or NMO (*N*-methyl-oxazolidone (Aldrich)) containing 0.3 mol/l LiI and  $3 \cdot 10^{-2}$  mol/l  $I_2$ . AN/EC based electrolytes yielded higher efficiencies, whereas NMO based electrolytes yielded higher reproducibility of the results. The counter electrode was a platinum electrode treated with a  $5 \cdot 10^{-3}$  mol/l  $H_2PtCl_6$  isopropanol solution and heated for 15 min. at  $450^\circ C$ .

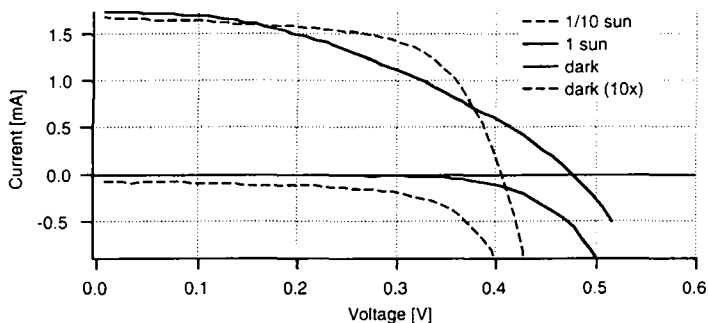


Fig. 5.4: I-V characteristics of a MCDPP sensitized solar cell measured after 2.5 hours illumination under short circuit conditions. The irradiation was  $100 \text{ mW}/\text{cm}^2$  white light from a Xe-lamp with a 400nm UV cut-off filter. The cell area is  $0.445 \text{ cm}^2$ . Total energy conversion efficiency is 0.77%.

The current-voltage (I-V) characteristics of the cell shown in figure 5.4 exhibits a good dark current characteristic, i.e. a low dark current up to 400 mV (on the scale 1 sun). The I-V curve of illumination by 1/10 of 1 sun intensity (1 sun = AM1.5,  $100 \text{ mW}/\text{cm}^2$ ) shows the same slopes as the dark current, indicating the validity of the model usually applied to solar cells that the current under illumination is the superposition of a constant current source (photocurrent) and a diode in parallel limiting the potential (dark current). This model has recently been confirmed for the photoelectrochemical cells by von Planta<sup>63</sup>. The open circuit potential agrees with the values found by Huang et al. for the electrochemical cell  $TiO_2/\text{dye}/(I_3^-/I^-)$  without using coadsorbants on the  $TiO_2$  electrode<sup>64</sup>.

However under illumination, the I-V curve changes qualitatively from the characteristics corresponding to the superposition of photocurrent and dark current (fig. 5.5), to the curve shown in fig. 5.4, where the photocurrent apparently decreases upon application of the external potential. This is attributed to a decrease in the injection efficiency or in the reduction efficiency of the oxidized dye in agreement with the discussion below of the remarkable current increase during the first 2-3 hours.

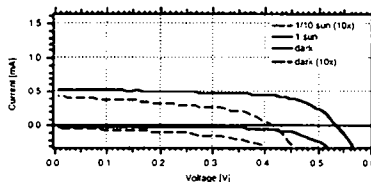


Fig. 5.5: I-V curve of the cell shown in fig. 5.4 recorded at the beginning of the 2.5 hrs illumination.

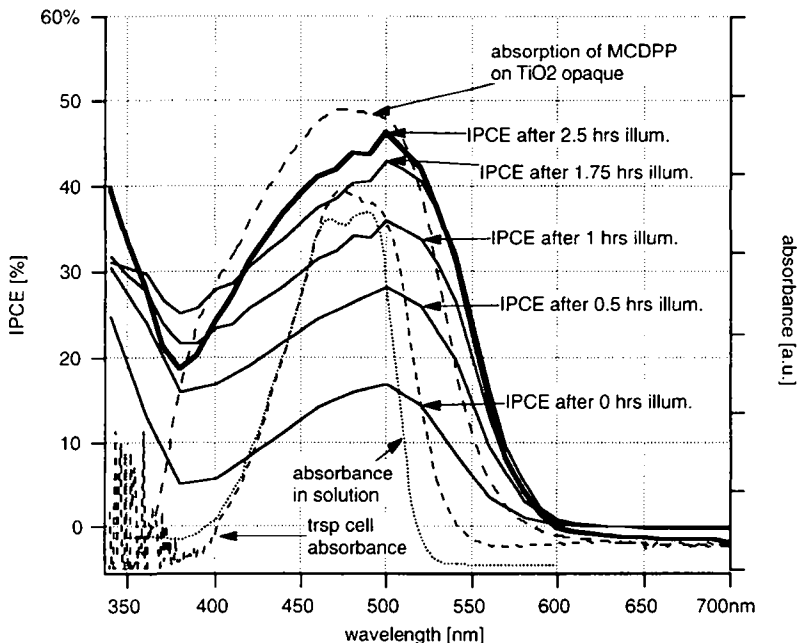


Fig. 5.6: action spectra (IPCE) of a MCDPP sensitized solar cell. The IPCE spectra were recorded after different times of continuous illumination, starting with a freshly prepared electrode. The working electrode was 10 $\mu$ m thick opaque colloidal TiO<sub>2</sub> layer sensitized by MCDPP. The electrolyte was NMO with 0.5 mol l<sup>-1</sup> LiI and 0.05 mol l<sup>-1</sup> I<sub>2</sub>. Irradiation was 100mW/cm<sup>2</sup> white light corresponding to AM1.5. The dashed lines show the absorption spectra of a cell of transparent TiO<sub>2</sub> and on opaque TiO<sub>2</sub> electrodes. The dotted line shows the absorption spectrum in solution.

The monochromatic photocurrent efficiency is described by the Incident Photon to Current conversion Efficiency (IPCE):

$$\text{IPCE} = \frac{\text{number of electrons collected}}{\text{number of photons incident on the cell surface}} \quad (5.6)$$

The IPCE is not a quantum efficiency for the charge injection, since recombination losses, short circuits and reflection losses may reduce the number of the collected electrons and the number of absorbed photons. Nevertheless it is the relevant quantity for photovoltaic applications.

The IPCE spectra shown in figure 5.6 were recorded at different times on the same cell. The cell was irradiated with AM1.5 light between the measurements. For the last measurement the electrolyte needed to be refilled since the cell dried out between the subsequent measurements. The change of the IPCE spectrum is thus attributed to the increased filter effect of the additional  $\text{I}_3^-$  in the electrolyte. The broadening of the IPCE spectrum compared to the absorption spectrum (shown in figure 5.6) is due to the opaque and highly scattering  $\text{TiO}_2$  electrodes used. Due to internal reflections leading to an increase of the effective optical path photons with energies in the absorption tail of the dye are more efficiently absorbed in highly scattering electrodes than in transparent electrodes.

The short circuit current increased under illumination during 3 hours to reach a maximum and subsequently decreased due to degradation of the dye on the electrode. The open circuit potential dropped during this period. Figure 5.7 depicts the short circuit currents as a function of the open circuit voltages for 3 NMO based cells.

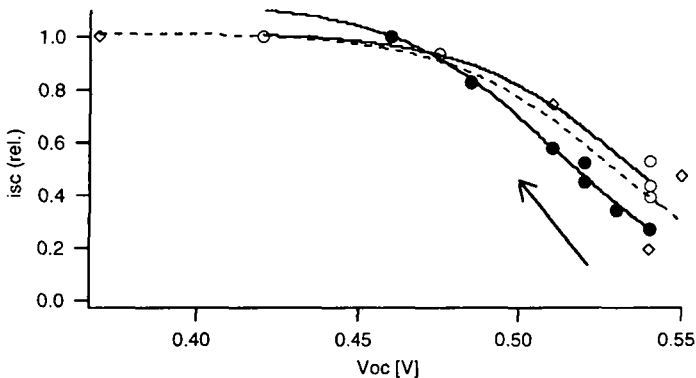


Fig. 5.7: Short circuit current vs open circuit voltage of 3 different cells sensitized with MCDPP. The arrow indicates the evolution direction with time.

The large increase of the short circuit currents during the first 2-3 hours of illumination was observed systematically. As depicted in figure 5.7 it was

accompanied by a decrease of the open circuit voltage. Since the investigation of the charge injection from the monomer in a electrochemical cell is beyond the scope of this work, the effect has not been studied in detail. Several reasons may account for the current increase and the simultaneous potential drop and shall be briefly mentioned:

Fluorescence quenching experiments of MCDPP by  $\text{LiI}/\text{I}_2 = 10/1$  in ethanol showed that the quenching rate of the excited state of MCDPP is controlled by diffusion. Since the charge transfer reaction is slow, as seen from the fluorescence quenching on  $\text{TiO}_2$  colloids, the excited dye can be reduced by  $\text{I}^-$  and the anion subsequently injects an electron into  $\text{TiO}_2$ . This reaction will be favored by the heating of the cell and the decrease of the solvent viscosity upon illumination of the cell. The dye may reorganize on the surface to a more homogenous coverage. Vibronic deactivation will be decreased.

Since the electron transfer reaction from the excited state of the dye is slow, it is non-adiabatic. The maximum driving force for this reaction is the difference between the excited state oxidation potential and the energy of the bottom of the conduction band of  $\text{TiO}_2$ . The latter depends on the solvent, the surface adsorbed ions and particularly on the pH of the solvent. Also the dark current depends on the flatband potential and increases with a lowering of the latter, thus lowering the open circuit voltage. A change in the flatband potential therefore explains simultaneously the increase of the injection yield and the decrease of the open circuit potential of the cell. The flatband potential variation is well explained by the degradation of the sensitizer on the surface of the  $\text{TiO}_2$  electrode. Analysis of the degradation products of DPP showed that benzoic acid is one of the major degradation products<sup>65,66</sup>. This product will then acidify the surrounding medium and lower the pH on the  $\text{TiO}_2$  surface, thus lowering the flatband potential.

Degradation products adsorbing on the  $\text{TiO}_2$  may also enhance the dark current and lower the open circuit potential. Indeed it has been shown by Moser<sup>67</sup> that the interfacial electron transfer from the  $\text{TiO}_2$  conduction band to acceptors in solution is enhanced by bidentate benzene derivatives that are adsorbed on the surface of the  $\text{TiO}_2$  particles.

### 5.3. Conductivity of DMADPP

DPP and its derivatives, especially the dithioketo derivative DTPP, have been shown to exhibit interesting conductive and photoconductive properties<sup>30-33,35</sup>. The conductivity of the *p*-dimethylamino derivative DMADPP has not yet been investigated.

The molecule has a more extended orbital structure for the HOMO than the DPP derivatives without the amino group. Therefore, while the charges will still be localized on one molecule, a better coupling to its neighbouring molecules is expected for the transport of holes. Furthermore the molecule has promising spectral properties for its application on organic solid state photovoltaic devices, since its spectrum is bathochromically shifted by 50 nm<sup>40</sup> yielding a blue color in the solid state.

Previous conductivity measurements of DPP's and DTPP were done based on a 2 electrode configuration, where the 2 electrodes were interpenetrating comb-like grids of Al at 100  $\mu\text{m}$  distance<sup>31</sup>. The compounds were then evaporated on top of the electrodes. In the present work the van der Pauw four point probe method was preferred in order to avoid contact resistance effects that are uncontrollable in 2 electrode methods.

The van der Pauw method<sup>68,69</sup> is extensively used in semiconductor material and device characterization<sup>70</sup>. Under application of a magnetic field it allows at the same time to determine the Hall mobility of the charge carriers. However, Hall potential may give misleading information about the drift mobility of the charge carriers in materials where the transport is supposed to happen through a hopping process, such as in non- or low crystalline organic conductors due to the ill defined hopping direction of the individual charge carriers<sup>71</sup>.

### 5.3.1. Experimental

Samples of 9 mm diameter were evaporated on glass substrates using a 0.5 mm thick aluminum mask shown in fig. 5.8. This configuration allows to minimize distortions due to non-ideal contact spots<sup>68,70</sup>. The background pressure was  $7 \cdot 10^{-6}$  mbar, the deposition rate was kept between 1 and 2 nm/sec. Sample thickness was 830 nm.

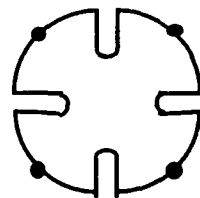


Fig. 5.8: Shape of van der

Pauw samples. Dark dots indicate contacting spots. Wires were contacted to the sample pads using silver paint. The wires were not screened with a triax voltage compensating system. However comparison of our measurements with measurements on a fully triax equipped system showed no significant difference, thus showing that leakage currents<sup>70</sup> did not influence our results.

The sample was held in a controlled atmosphere of pure nitrogen or oxygen at 1 atm pressure in a cryostat at room temperature.

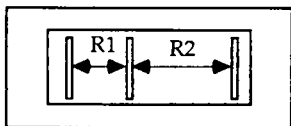


Fig. 5.9: geometry for estimating contact resistances.

The contact resistance was estimated by differentiating the total resistance vs the sheet resistance using different sample lengths. The geometry is shown in figure 5.9. The contact resistance was estimated to be less than  $10^8$  Ohm/cm<sup>2</sup>. Thus for the size of the contacts, 0.1 cm<sup>2</sup>, the contact resistance is about 1/10 of the total measured resistance of the sample, which is in the order of  $10^{10}$  Ohms.

### 5.3.2. Results and discussion

The resistivity was measured using a voltage source between 1.5V and 130V and the resulting current was measured using a Keithley 616 shunt electrometer. Voltages were measured with a  $10^{14}$  Ohm input impedance device.

The resistivity was measured at room temperature to be  $4.4 \cdot 10^5 \pm 10\%$  Ohm cm. Ambient humidity produced a large increase of the conductivity, whereas in pure nitrogen or oxygen stable results were achieved. No difference of the resistivity was observed under nitrogen or oxygen as an ambient atmosphere. The resistivity was independent of the applied field for  $E=2$  V cm<sup>-1</sup> to  $10^3$  V cm<sup>-1</sup>.

The temperature dependence of the resistivity shows an activation energy of 0.49 eV (fig. 5.10). This value is smaller than the value observed by Mizuguchi for DTPP<sup>31</sup>, but higher than the values observed for pure phthalocyanines<sup>72</sup>, where the observed activation energies correspond to the energy gap. The available temperature domain is too small to distinguish different transport mechanisms by their temperature dependence<sup>72</sup>.

No photoconductivity and no photocurrent in the ITO/DMADPP/Al sandwich cell was observed upon irradiation with white light (AM 1.5). The photoinduced charge carrier generation is thus not efficient. Similarly to the argumentation of Mizuguchi for the DPPP<sup>35</sup> this observation indicates that the exciton splitting in the material is not efficient. Due to the relatively large dark conductivity of the undoped sample, comparable to that observed for protonated DPPP, the mobility of the charge carrier is expected to be high and thus additional charge carriers would increase the conductivity. This observation is confirmed by the fact that no surface photovoltage is observed. The material was therefore not used for the solid state photovoltaic cells in the following part.

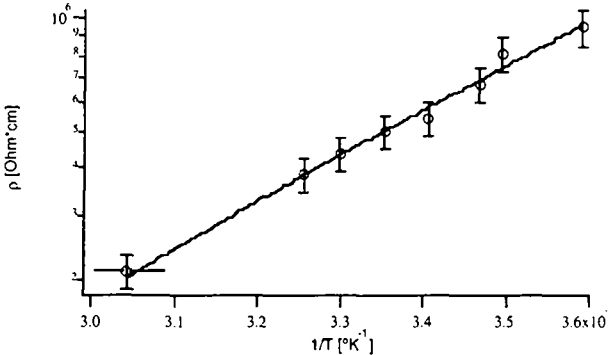


Fig. 5.10: Temperature dependence of bulk resistivity of DMADPP evaporated layer. The layer thickness was 835nm. The vertical lines indicate the estimated errors of the measured resistivity. The horizontal lines on the measurement at  $T^{-1} = 3.05 \cdot 10^{-3} \text{K}^{-1}$  indicates the uncertainty of the temperature of this particular point. The additional uncertainty is due to the method of heating by light irradiation previous to the resistance measurement.

## 5.4. Solid state solar cells

### 5.4.1. Sample preparation

The solid state solar cells were prepared as sandwich structures. Glass substrates with fluor doped  $\text{SnO}_2$  ( $10\Omega/\square$ ) transparent conductive layers were received from NSG.  $\text{SnO}_2$  was etched with Zn powder and 4N HCl solution.  $\text{TiO}_2$  colloidal layers were deposited by screen printing technique yielding 300 nm thick optically transparent layers.  $\text{SnO}_2$  (fluor doped) layers were rinsed with alcohol prior to sputter etching.  $\text{SnO}_2$  and  $\text{TiO}_2$  layers were cleaned by a plasma sputter etching procedure with  $5 \cdot 10^{-4}$  mbar residual air pressure in a separate vessel during 10 minutes and exposed to ambient air for the transfer to the evaporator. Dye layers were evaporated at a background pressure  $< 5 \cdot 10^{-6}$  mbar at 1-2 nm/sec for layer thicknesses  $< 500$  nm and 10 nm/sec for thicker layers. For the evaporation of the Au layers the samples had to be exposed to air and moved to a second evaporator. Au layers were evaporated at  $2 \cdot 10^{-6}$  mbar to 30 nm thickness. MCDPP was adsorbed from a saturated solution in acetonitrile.

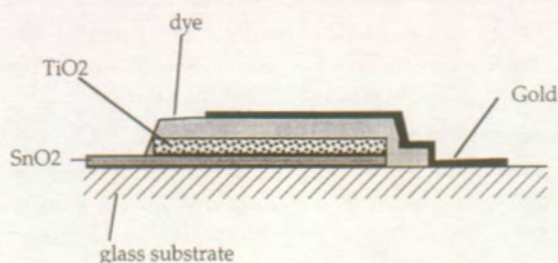


Fig. 5.11: Structure of the solar cells.

Sample	Structure	Thickness [nm]
A	Au	30
	DPP	300
	TiO <sub>2</sub>	300
	SnO <sub>2</sub>	400
B	Au	30
	DPP	300
	MCDPP	monolayer adsorbed
	TiO <sub>2</sub>	300
	SnO <sub>2</sub>	400
C	Au	30
	DTPP	500
	SnO <sub>2</sub>	400
D	Au	30
	DTPP	500
	TiO <sub>2</sub>	300
	SnO <sub>2</sub>	400

Table 5.1: Structures of the solid state solarcells

#### 5.4.2. Results and discussion

DPP and DTPP were used as hole conductors and simultaneously as the photosensitive and charge injecting layer into TiO<sub>2</sub> or SnO<sub>2</sub>. DPP and DTPP form a p-n heterojunction on TiO<sub>2</sub>. From table 5.2 it is seen that DPP and MCDPP have a large overpotential for the injection into TiO<sub>2</sub>, whereas DTPP has only a small overpotential if the TiO<sub>2</sub> surface is not protonated<sup>62</sup>.

##### 5.4.2.1. Cells using DPP

From the cell A only a very small photocurrent of 10 to 60 nA at 100 mW/cm<sup>2</sup> white light illumination was observed. The photocurrent increased during the first 5



minutes of illumination and the I-V characteristics changed drastically from a well blocking dark characteristic to 1.3 k $\Omega$  resistivity at zero potential. From SEM pictures it was seen that the dye penetrates only a few nanometers into the porous TiO<sub>2</sub> layer. It was however difficult to measure a precise penetration depth due to the weak contrast of organic materials in SEM pictures. A 300 nm thick TiO<sub>2</sub> layer thickness was chosen as it is the lowest thickness achieved that allows to avoid pinholes with the colloidal TiO<sub>2</sub> layers available in our laboratory. The cell B using a monolayer of adsorbed MCDPP on the surface of the TiO<sub>2</sub> brought a drastic improvement of the photocurrent (figure 5.13). MCDPP<sup>\*</sup> has been shown to efficiently inject electrons into TiO<sub>2</sub>. The monosubstituted DPP offers an organic surface to the subsequently evaporated DPP molecules and allows to form a good contact on the molecular scale. The action spectrum of the cell in figure 5.12 and comparison to the action spectrum of molecular MCDPP in the photoelectrochemical cell show that MCDPP is the electron injecting species. The larger extension of the action spectrum in the photoelectrochemical cell is attributed to the multiple reflection enhanced absorption of red light in the opaque TiO<sub>2</sub> electrodes due to the internal scattering and is observed for all dye classes on these electrodes.

compound	E(R/R <sup>-</sup> )	E(R <sup>+</sup> /R)
DPP	-1130	+840
MCDPP	-1150	+990
DTPP	-660	

**Table 5.2:** Redox potentials of DPP and derivatives mV vs SCE. The measured by cyclic voltammetry in DMF (dimethyl formamide) with the supporting electrolyte 0.1M TBATFB (tetrabutylammonium tetrafluoroborate) and a glassy carbon working electrode. For DTPP the oxidation wave could not be observed due to the limited electrochemical window of DMF for oxidation reactions.

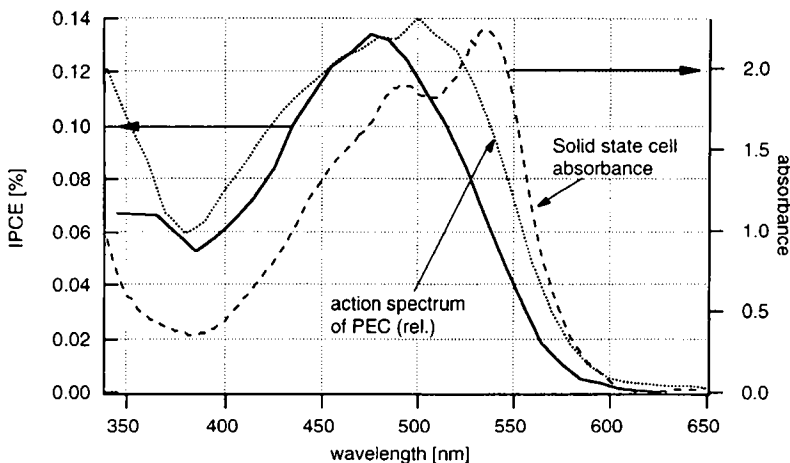
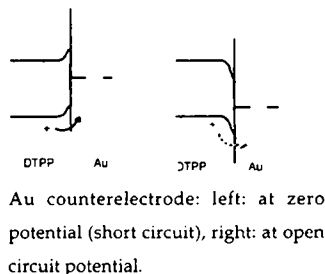


Fig. 5.12: IPCE spectrum of DPP on  $\text{TiO}_2$  (cell B) with a monolayer of MCDPP adsorbed before evaporation of DPP. The dashed line shows the absorption spectrum of the cell and the dotted line shows the action spectrum of a photoelectrochemical cell using MCDPP as a sensitizer and an opaque  $10\mu\text{m}$  thick  $\text{TiO}_2$  layer.

Typical I-V curves are shown in figure 5.13 in darkness and under white light. It shows that the cell presents a double junction and thus the DPP-Au interface presents a Schottky barrier for the hole transfer from DTPP to Au, i.e. the counterelectrode does not form an ohmic contact.

Illumination through the Au electrode resulted however in negligible photocurrent, confirming that the active interface is between MCDPP and  $\text{TiO}_2$ . Similar current-voltage curves have been observed on organic-organic heterojunction systems, e.g.  $\text{CuPc}/\text{Im-PTC}^{21}$ . The open circuit potential achieved was 0.75 V.



Au counterelectrode: left: at zero potential (short circuit), right: at open circuit potential.

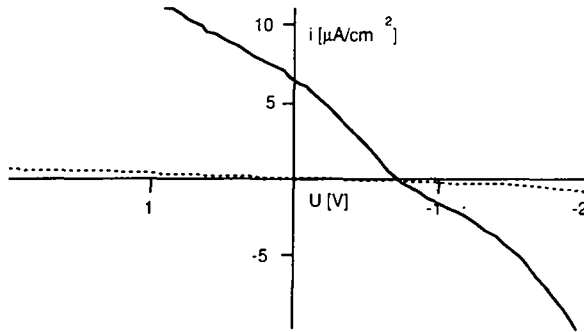


Fig. 5.13: I-V characteristics of DPP on  $\text{TiO}_2$  (cell B). The dashed line presents the I-V curve at dark, the solid line at and illumination of  $100 \text{ mW}/\text{cm}^2$  from a Xe-lamp with a 400 nm cutoff filter.

Furthermore the I-V curve shows that the conductivity of the DPP is increased under illumination and the photocurrent generation of DPP is increased by the applied potential. The field is too low to assist excitation separation, but it supports the charge carrier migration away from the surface and thereby decreases the recombination. Since the photocurrent is produced by the electron injection from MCDPP to  $\text{TiO}_2$  this indicates that the photocurrent is limited by the charge transport away from the interface.

#### 5.4.2.2. Cells using DTPP

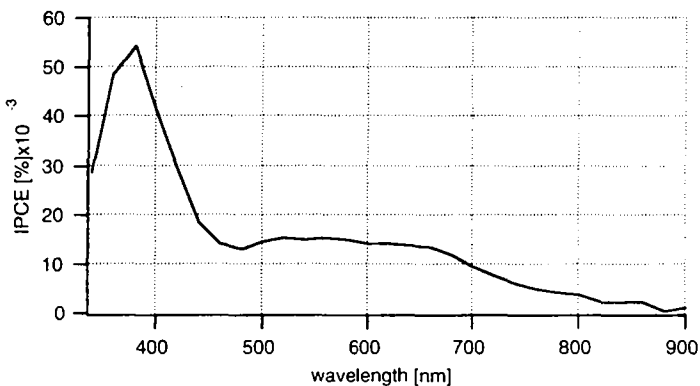


Fig. 5.14: IPCE spectrum of DTPP on  $\text{TiO}_2$  (D) .

Figure 5.14 shows the action spectrum of DTPP on  $\text{TiO}_2$ . The spectrum corresponds to the absorption tail of  $\text{TiO}_2$  in the near UV region and the dye layer in the visible region. From photovoltage measurements (see below) on the identical  $\text{TiO}_2$  layers, subband-gap states were located at wavelengths up to 450 nm. However, the relative charge carrier generation efficiencies do not correspond to the relative absorptions of the  $\text{TiO}_2$  and the DTPP layers.

Upon exposure of the sample to acetone vapor for 1.5 hours (vapor treatment<sup>32</sup>) the absorption spectrum changes as it has been described by Mizuguchi<sup>32,41</sup> and Arita<sup>73</sup> and the photocurrent is largely increased (figure 5.15). This observation is in agreement with the increase of photocurrent reported by Mizuguchi<sup>41</sup> of the vapor treated DTPP thin films. However, the action spectrum does not correspond to the absorption of the cell, indicating again that the charge carrier separation efficiency of DTPP is lower than for  $\text{TiO}_2$ .

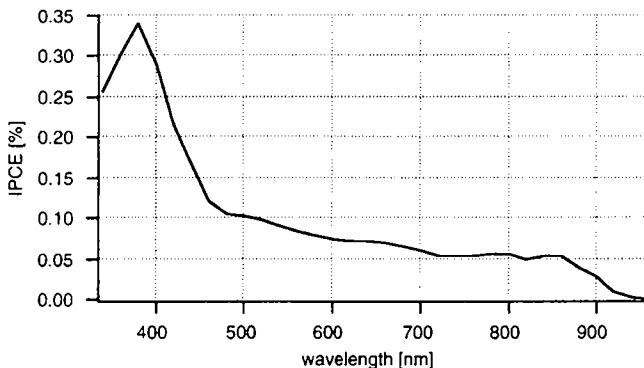


Fig. 5.15: IPCE spectrum of DTPP on  $\text{TiO}_2$  (D) after exposure to acetone vapor for 1.5 hrs.

The I-V curve in figure 5.16 exhibits similar properties as observed for the DPP cell (A). The photocurrent generation of DTPP on the  $\text{TiO}_2$  surface is increased by the applied external field. The photocurrent is sublinear with the illumination intensity, at 1/10 of the illumination intensity 12% of the photocurrent were measured. This indicates that the resistivity, or the charge transport, are limiting the cell performance. The fill factor is less than 25% due to the double junction characteristics.

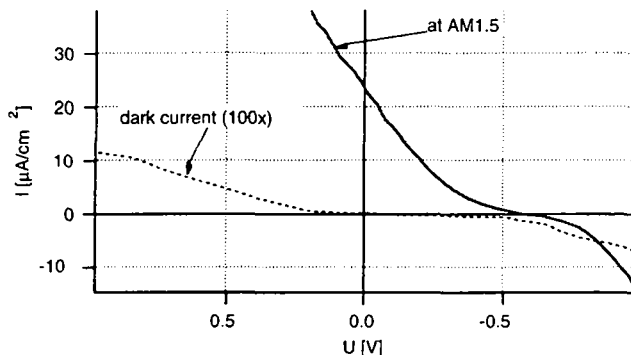


Fig. 5.16: I-V curve of DTTP on  $\text{TiO}_2$  (D) after exposure to acetone vapor for 1.5 hrs. Illumination from a Xe-lamp using a 400 nm filter with an intensity of  $100 \text{ mW}/\text{cm}^2$ .

From the IPCE spectra in figures 5.14 and 5.15 it is seen that the bulk DTTP injects electrons into  $\text{TiO}_2$  with a poor yield compared to the yield of the direct  $\text{TiO}_2$  excitation in the UV. Nevertheless DTTP is a good hole conductor for the hole collection from  $\text{TiO}_2$ . This may be attributed to a too low conduction band energy in DTTP for the injection into  $\text{TiO}_2$ .

In order to check the hypothesis of too low conduction band in DTTP a sandwich cell  $\text{SnO}_2/\text{DTTP}/\text{Au}$  has been tested. The dye injects electrons into  $\text{SnO}_2$  as shown in figure 5.17. The action spectrum of a DTTP layer on  $\text{SnO}_2$  covers the whole wavelength range of absorbance of the cell. The IPCE is comparable to the IPCE observed for the DTTP on  $\text{TiO}_2$  but the spectral features of the DTTP are better reflected in the  $\text{SnO}_2/\text{DTTP}/\text{Au}$  cell. From the direct correlation of the absorption spectrum and the IPCE spectrum, i.e. there is no inner filter effect, we conclude that the charge separation takes place at the  $\text{SnO}_2/\text{DTTP}$  interface. Illumination from the back side through the 30 nm Au layer yielded only a photocurrent of  $150 \text{ nA}/\text{cm}^2$  compared to  $10 \text{ } \mu\text{A}/\text{cm}^2$  from illumination on the  $\text{SnO}_2$  side confirming that the charge separation at the Au/DTTP interface is not efficient.

As will be seen in the following part, the investigations by Kelvin probe showed that a band bending exists at the  $\text{SnO}_2/\text{DTTP}$  interface and extends 200 nm into the DTTP layer, suggesting that the photoactive layer is 200 nm thick. The preparation of 200 nm thick samples was not successful, due to frequent short circuits. These are due to the fact that the evaporated layers were composed of microcrystalline grains of 200 nm average size as seen from scanning electron microscopy (SEM) images.

The I-V curve under illumination showed a pure ohmic behaviour around the zero potential. Application of higher potentials resulted in irreversible breakdown of

the samples. Again the conductivity of the illuminated sample is greatly increased, owing to the photoconductivity of the compound.

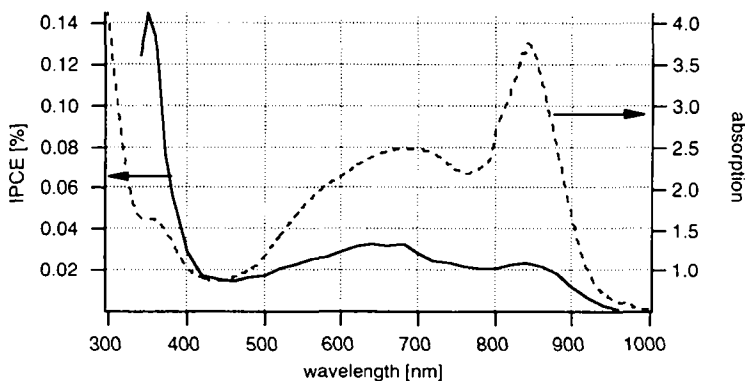


Fig. 5.17: IPCE spectrum of DTPP on  $\text{SnO}_2(\text{C})$  after exposure to acetone vapor for 1.5 hrs. The dotted line shows the absorption spectrum of the sample.

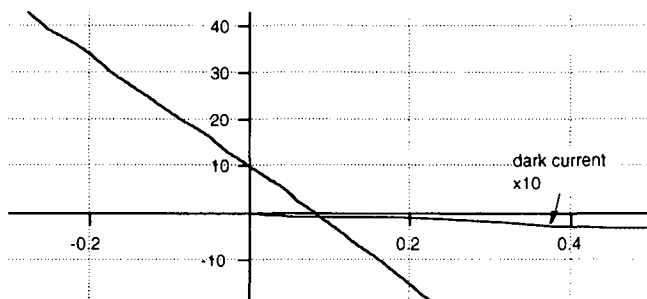


Fig. 5.18: I-V curve of DTPP on  $\text{SnO}_2(\text{C})$  after exposure to acetone vapor for 1.5 hrs. Illumination from a Xe-lamp using a 400 nm filter with an intensity of  $100 \text{ mW/cm}^2$ .

The results show that both DTPP and DPP do produce photovoltaic effects on  $\text{TiO}_2$ , but the photocurrent yields are poor. This is attributed to the weak conductivity of the materials yielding poor I-V characteristics and fill factors and the weak exciton splitting yielding low photocurrents at short circuit. This is supported by the large increase of photoconduction upon heating DTPP reported by Mizuguchi<sup>31</sup> attributed to temperature assisted exciton splitting, showing that the exciton splitting at room temperature is not very efficient.

*Comments on Time of flight measurements*

In organic solid state solar cells the charge carrier transport is often an efficiency limiting step and it has been concluded that this applies together with the limited exciton splitting efficiency to the DPP and DTPP based solar cells. High mobilities are needed due to the small potential loss affordable. In order to quantify the charge carrier transport in DTPP and DPP, transient current measurements or time-of-flight were undertaken. The setup constructed for this purpose has been described in the chapter 2. It allows us to measure transient current signals with a time resolution of up to 100ns using a shunt resistance of 50  $\Omega$ . Higher shunt resistances increase the sensitivity but decrease the time resolution of the setup. Sandwich cells with a SnO<sub>2</sub>/DTPP/Au or SnO<sub>2</sub>/TiO<sub>2</sub>/DTPP/Au structure with organic layer thicknesses ranging from 1  $\mu\text{m}$  up to 17 $\mu\text{m}$  were prepared by the same evaporation method as described above. The samples were similar to the chlorophyll *a* samples used by Kassi<sup>9</sup>. The additional TiO<sub>2</sub> layer was a sputtered layer prepared at Hoechst AG, Germany. The TiO<sub>2</sub> layer absorbed more than 95% of the excitation light at 347 nm. It was used as a blocking layer to block the dark current and simultaneously as a hole injection layer upon TiO<sub>2</sub> band to band excitation at 347nm. The validity of the setup was confirmed by the measurement of the mobility of a novel organic hole conductor from the company Hoechst AG, where a mobility in the range of  $2 \cdot 10^{-5} \text{ cm}^2\text{V}^{-1}\text{s}^{-1}$  to  $10^{-4} \text{ cm}^2\text{V}^{-1}\text{s}^{-1}$  was measured for samples of the same design with an organic layer thickness of 1 $\mu\text{m}$ .

For DPP and DTPP however, the signals observed were below the time resolution of the setup as seen from the lack of dependence of the observed time constants on the applied field. Under application of a constant voltage to the thick samples with the structure SnO<sub>2</sub>/DTPP/Au the amplitude of transient current decreased during a series of laser pulses and was restored after application of an inversed voltage and at least one laser pulse. Therefore it was concluded that the majority of the created charge carriers were efficiently trapped within the sample. The accumulated charges produce an electrical field of opposite sign to the externally applied field and lower the charge separation efficiency during subsequent laser pulses. Application of inverse external field or short circuit and generation of charges by one laser pulse allows the charge carriers to neutralize the built up internal field, thus restoring the initial conditions in the sample.

## 5.5. Surface photovoltage spectroscopy

The surface photovoltage (SPV) measurement is a contactless, nondestructive and sensitive tool for the investigation of surface and interface band bending based on the effect of illumination on the semiconductor work function. The interfaces considered in this work are solid/gas interfaces and solid/solid interfaces and the focus is on the bandgap illumination. Surface photovoltage spectroscopy (SPS) is an offshoot of this technique<sup>38</sup>, which has been used for the study of surface and interface gap states using subband-gap illumination. Three techniques are currently used for SPV/SPS measurements: the Kelvin probe method, used in this work, the chopped light fixed electrode method and ac illumination modulated electron beam method.

SPV/SPS has been widely used for the characterisation of inorganic materials<sup>38,74,75</sup> e.g. for the investigation of surface treatment effects<sup>76</sup> or surface and interface band bending and built in potentials in solar cells<sup>39,77-79</sup>. Recently it has been applied also for the investigation of organic semiconductors such as porphyrins<sup>80</sup> and phthalocyanines<sup>81,82</sup>. Kelvin probe measurements in the dark have been used for the determination of the conduction type of perylene derivatives<sup>83</sup>.

### 5.5.1. Theory of the SPV/SPS method

In the following part we will focus on the effect of surface photovoltage experiments based on bandgap excitation and neglect effects of surface state excitation by sub-bandgap light since this region was out of the accessible wavelength range of our equipment. In the experiments presented below the spectral features of SPS measurements were used to distinguish front- and backside illumination effects of the bandgap excitation (fig. 5.19).

In the following presentation of the theoretical background extensive use of energy diagrams is made. The definition of the vacuum level used in there deserves to be defined more closely in this introductory remark. The energy of an electron at rest at infinity is defined as zero and is called the absolute vacuum level,  $E_{vac. abs.}$ . In solid state science it is commonly used as the reference for potential energy. For our convenience we use a local vacuum level,  $E_{vac.}$ , which represents the energy of an electron at rest just outside the semiconductor and free from the influence of the crystal potential. Thus, the position of  $E_{vac.}$  with respect to  $E_{vac. abs.}$  is given by the potential energy other than that due to the crystal potential<sup>84</sup>. In other words, it is a "gedanken" potential energy which an electron would have if, at any place in the



crystal it could be removed from its environment to a position just outside the semiconductor, without crossing the electric fields present at the surface due to surface charges or dipoles. The difference between  $E_{vac}$  and  $E_{vac, abs}$  is also called the outer potential,  $\Psi$ , and is due to the electrostatic field at the surface<sup>85,86</sup>. The local vacuum levels appear in the diagram as a continuous but not constant top line.

SPV/SPS discussed here is based on the classical Kelvin probe technique<sup>75,87</sup>, which measures the difference in work functions (=contact potential difference (CPD)) between a metallic reference probe and the semiconductor surface under investigation. The sample and the reference electrode form a capacitor whose capacity is modulated by the variation of the distance between the reference electrode and the sample by means of a piezoelectric crystal (fig. 5.19). If the two workfunctions in the probe and the reference electrode are not equal, an AC current is generated by this capacity modulation for the charging/discharging of the capacitor. Adding an offset potential to the reference electrode allows to null the work function difference thereby nulling the charging current. The magnitude of the necessary offset potential is equal and opposite to the CPD. Figure 5.19 a) depicts the energy levels at the semiconductor-air-probe interface for a p-type semiconductor.  $\chi$  is the electron affinity,  $E_{vac}$  is the local vacuum level (i.e. subject to the local electrostatic field)<sup>84</sup>,  $E_C$  and  $E_V$  are the conduction and valence band energies respectively,  $\phi_{ref}$  is the Fermi energy of the reference probe vs vacuum.  $eV_s$  is the surface band bending. Hence, the CPD in the dark is

$$eV_{CPD} = \phi_{ref} - [\chi + (E_C - E_F)_{bulk} - eV_s] \quad (5.7)$$

In the dark, the Kelvin probe measures the work function at the surface of the semiconductor. On samples with thickness below the depletion width the term  $(E_C - E_F)$  changes from the bulk value towards the surface value and is reflected in the workfunction measured at the surface. Thus by varying the thickness of the samples the depth of the band bending at the substrate/semiconductor interface can be investigated (figure 5.20).

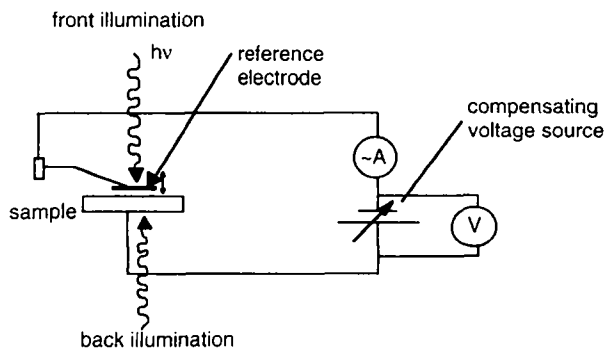
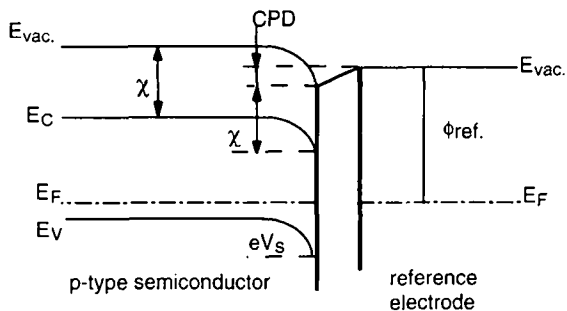


Fig. 5.19: Energy band diagram for p-type semiconductor and schematic circuit diagram for CPD measurement technique.

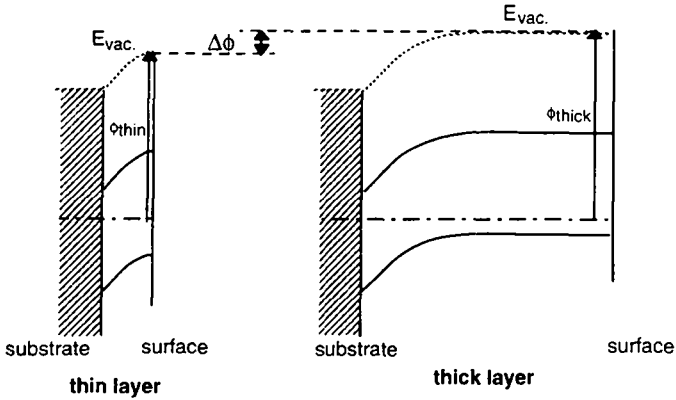


Fig. 5.20: Energy band levels for a thick (right) and a thin( left) sample.  $\Delta\phi$  denotes the variation of the CPD observed for the different film thicknesses in the presence of a band bending. For a *p*-type semiconductor the CPD decreases in the region of the band bending.

In SPV charge carriers are excited from the valance band to the conduction band by bandgap illumination. Some of the charge carriers are captured in empty surface states, resulting in diminished surface charge and hence surface band bending. The variation of the CPD is illustrated in figure 5.21. Thus the absolute value of  $|eV_s|$  decreases and the observed CPD changes according to the sign of  $eV_s$  as can be seen in eq. 5.8. Hence the response to the illumination serves as a straightforward means of determining the size and direction of the surface band bending and thus of the type of the semiconductor (*n* or *p*).

$$\Delta\text{CPD} = - [\Delta\chi + \Delta(E_C - E_F)_{\text{bulk}} - \Delta eV_s] \quad (5.8)$$

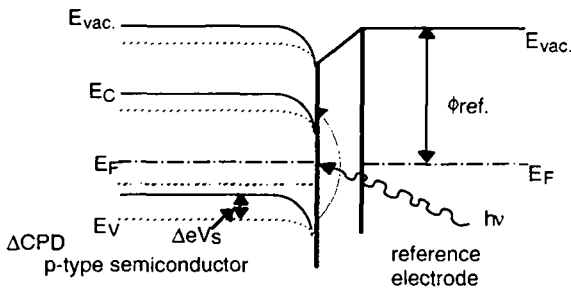


Fig. 5.21: Energy band diagram of a *p*-type semiconductor with a surface band bending, depicting the CPD variation induced by front side illumination of the semiconductor.

The illumination of the backside of the sample generates charge carriers near the interface substrate/semiconductor. Under the influence of the band bending they will separate and build up an electric field opposed to the built in potential difference.

The effects on the position of the Fermi level and the CPD are depicted in figure 5.22. Due to the flattening of the bands on the substrate/semiconductor side the Fermi level shifts downwards. The expression in equation 5.7 needs to be completed with the variation of the backside band bending expression,  $\Delta eV_{bs}$ :

$$\Delta CPD = - [\Delta\chi + \Delta(E_C - E_F)_{bulk} - \Delta eV_s + \Delta eV_{bs}] \quad (5.9)$$

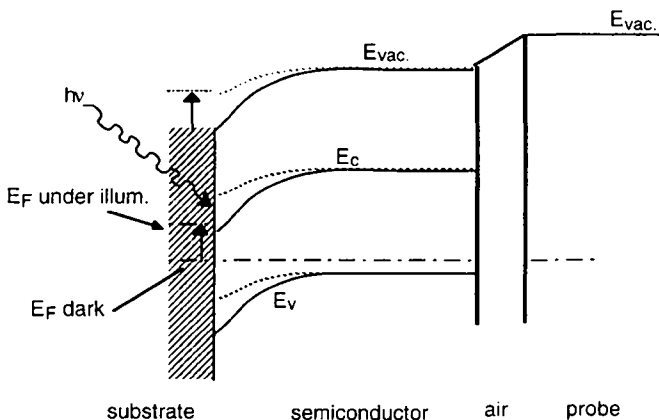


Fig. 5.22: Energy band diagram of a p-type semiconductor with a band bending on the substrate interface and variation upon backside (substrate side) illumination. For the better understanding of the backside effect the surface (probe side) band bending has been omitted. The voltage difference measured upon illumination is the shift of the substrate against the potential of the probe.

### 5.5.2. Sample preparation

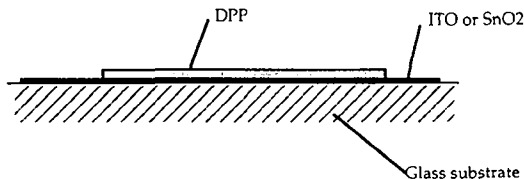


Fig. 5.23: samples for SPS

The samples were evaporated on ITO (DPP and DMADPP) or SnO<sub>2</sub> (all DTPP samples) conductive glass substrates as described above. ITO substrates were cleaned with a HELMATEX solution and rinsed with MeOH. SnO<sub>2</sub> substrates were cleaned with MeOH and cleaned by plasma sputter etching for 15 minutes at  $5 \cdot 10^{-4}$  mbar residual air pressure.

### 5.5.3. Results and discussion

The work functions of DPP, DMADPP and DTPP were determined by the measurement of the contact potential difference in air in the dark. The measurements are very reproducible and independent of air humidity indicating that surface adsorbed water is not influencing the measurements as is often observed for the measurement of hydrophilic surfaces such as metal oxides. The observed variations of the CPD are attributed to the relaxation of the samples that proved to be in the range of several tens of minutes after illumination by ambient light.

compound	work function
DPP	$5.38 \pm 0.03$ eV
DMADPP	$5.08 \pm 0.03$ eV
DTPP	$4.95 \pm 0.03$ eV

**Table 5.3:** Workfunctions measured in the dark. DPP and DMADPP were evaporated onto ITO substrates, thickness was for DPP 0.9  $\mu\text{m}$  and 3  $\mu\text{m}$ , both yielding the same workfunction, and for DMADPP 0.5  $\mu\text{m}$ . DTPP was evaporated onto SnO<sub>2</sub>. The workfunction was constant for samples thicker than 230 nm (see fig. 5.24).

The work function of DPP is 5.38 eV vs vacuum level. Comparing this to the redox levels in table 5.2 taking into account that 0V vs SCE = 4.74 eV vs vacuum and assuming that the oxidation potential is identified with the valence band and the reduction potential with the conduction band<sup>88</sup>, this identifies DPP as a p-type semiconductor. For DMADPP the work function was  $5.08 \pm 0.03$  eV. This value is lower than for DPP and the variation corresponds to the down shift of the oxidation potential observed in the electrochemical measurement presented in chapter 4.4.2.1.

For DTPP the work function was found to be 4.95 eV. The relation to the redox potentials is more difficult with DTPP, since the absorption onset, and thus the  $E_{00}$  energy, undergoes a large shift in the solid<sup>41</sup>. In view of the photovoltaic performance of DTPP and the reported photoconductivity<sup>32,41</sup>, the work function was investigated in more detail. The work function was found to depend on the thickness of the DTPP layer as shown in figure 5.24.

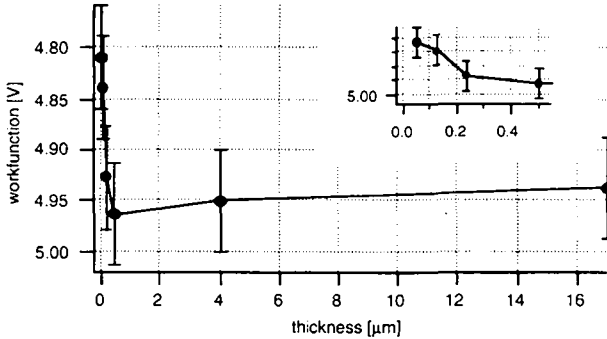


Fig. 5.24: Work function of DTPP as a function of layer thickness. The inset shows the detail for the low thickness.

The work function evolves from 4.95 V for thick samples to 4.81 eV for samples below 230 nm thickness. The workfunction of bare  $\text{SnO}_2$  was  $4.84 \pm 0.05$  eV. The variation is not attributed purely to the effects of imperfect surface coverage on the basis of the photovoltage of the 50 nm thick layer that was still more than 60% of the value observed for thick samples, although it can not be completely ruled out. The difference in the work function between  $\text{SnO}_2$  and thick DTPP shows that there is a built in potential of at least 100 mV at this interface and the band bending is confined to a layer thickness of less than 230 nm. This built in potential value is a lower limit, since on the DTPP a surface photovoltage was observed of +80 mV under an illumination intensity less than that needed for saturating. The Fermi level in the bulk DTPP is therefore at least 80 mV more positive than the workfunction measured at the surface and this value adds to the built in potential at the  $\text{SnO}_2/\text{DTPP}$  interface. The same argument explains the lower work function measured for the 50 nm thick layer than for the bare  $\text{SnO}_2$ . No photovoltage was observed on the latter.

The photovoltage spectra of DTPP have been recorded using both the back side and front side illumination. On thick samples the light does not penetrate through the whole sample and the observed photovoltages may be attributed to separate back- and front side effects. On the thin samples however, the light penetrates through the whole sample and mixed effects of the back- and front side are observed simultaneously.

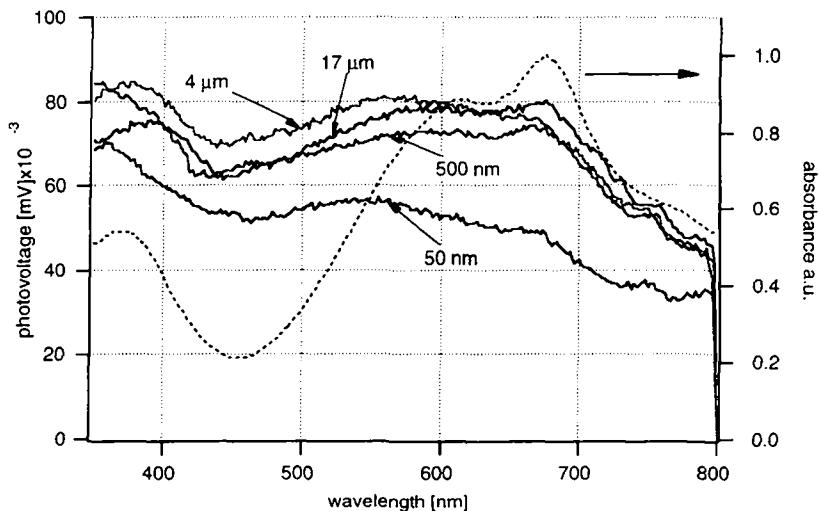


Fig. 5.25: SPS spectra of 4 different sample thicknesses. The dashed line shows the absorption spectrum of the evaporated layer on a relative scale.

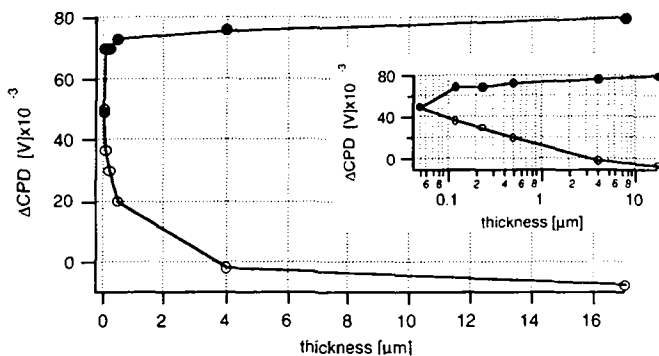


Fig. 5.26: dependence on the sample thickness of the SPV signal upon front (full circles) and back (open circles) illumination. The inset shows the same data on a logarithmic scale of thickness.

From figure 5.26 it is seen that the photovoltage is independent of the sample thickness down to 100 nm. The decrease observed for the 50 nm thick sample may be attributed to a limited surface coverage of the sample. The corresponding band bending must therefore be confined to a layer of less than or equal to 100 nm thickness. The sign of the photovoltage indicates a depletion layer at the surface,

indicating that DTPP is a p-type organic semiconductor. The spectrum is correlated to the absorption spectrum, however the characteristic variations are less pronounced in the SPS spectrum. This is due partly to the fact that the illumination is dependent on the Xe lamp spectrum since our equipment does not allow to maintain a constant photon flux over the whole spectral region. Since the photovoltage is not linear with the irradiation intensity, corrections for the Xe lamp spectrum of the observed signal would introduce additional errors.

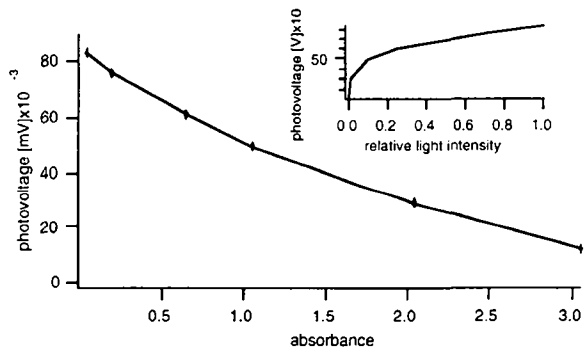


Fig. 5.27: SPV signal of the 4  $\mu\text{m}$  thick sample upon irradiation at 660 nm filtered by gray filters of absorbances up to absorbance 3. The inset shows the same data as a function of the relative light intensity

Figure 5.27 shows that the SPV signal decreases only by 40% for a decrease of the irradiation intensity of a factor of 10. This explains the weak dependence of the SPV signal on the absorption spectrum.

Irradiation from the back side yielded a small negative signal for the thick samples and a signal identical to the front illumination signal for the thin samples. The dependence of the SPV signal at 660 nm on the sample thickness for the front and the back side illumination signals is shown in figure 5.26 and the SPS spectra observed for 3 different sample thicknesses are presented in figure 5.28.



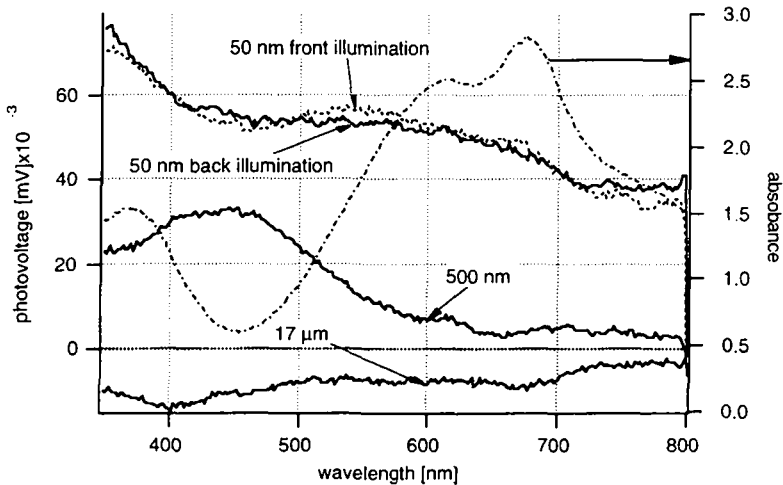


Fig. 5.28: SPS spectra of back illumination of 3 different sample thicknesses. The dashed line shows the absorption spectrum of the 500 nm thick layer. For comparison the front illumination signal of the 50 nm thick sample is plotted as a dotted line.

In thick layers all the light is absorbed within the bulk (trace “17 $\mu\text{m}$ ” in figure 5.28). The signal observed upon backside illumination is thus the variation of the voltage difference between the substrate and the probe due to the band flattening at the substrate/DTPP interface. In ideal cases the signal amplitude is identical to the open circuit voltage, i.e. the built in potential, of the junction on the backside, as has been demonstrated for *a*-Si solar cells by Goldstein<sup>78</sup>. The signal of DTPP on SnO<sub>2</sub> is weak in spite of the band bending determined from the thickness variation of the dark work function presented above. Since DTPP injects charges into SnO<sub>2</sub> as it was shown in the solid state solar cell experiments above, the charge generation process that decreases the band bending has to compete with the charge injection reaction leading to charge recombination if the cell is in open circuit situation. The effect of reduced SPV signals due to charge carrier recombination in metal on the surface of the semiconductor has been demonstrated for the Al-GaAs interface on GaAs single crystals by Brillson<sup>89</sup>. The Al layer was shown to limit the saturation of the SPV signal with light intensity. Indeed, on our layers the back illumination signal shows a much weaker tendency to saturate than the front side signal (figure 5.29).

In thin samples both the back and the front side are excited by the irradiating light since the sample absorbs only a small fraction of the light and the SPV signal is dominated by the front (surface) side photovoltage (trace "50nm" in figure 5.28).

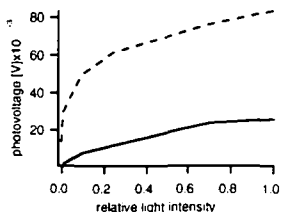


Fig. 5.29: photovoltages of a 4  $\mu\text{m}$  thick (opaque) sample of back and front side illumination at different intensities. Back side illumination was at 420 nm, front side illumination at 660 nm.

In medium thick samples we observe a signal that corresponds to the front side signal obtained by irradiation through a filter with the spectrum of DTPP, i.e. filtered by the inner filter effect of the sample itself. The comparison of the  $\Delta\text{CPD}$  observed upon backside and frontside illumination on the 500 nm thick sample illustrates this effect best (fig. 5.31). Fig. 5.30 compares the

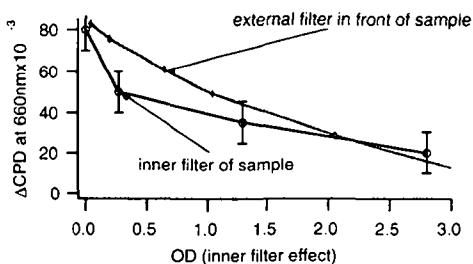


Fig. 5.30: Inner filter and external filter effect on the SPV signal observed at 660 nm. For the external filter effect measurement the 4  $\mu\text{m}$  thick sample was used. For the inner filter effect the data in fig. 5.26 were used and the optical density of the layers calculated as a function of their thickness.

measured backside illumination signal at  $\lambda = 660$  nm of layers of different thicknesses plotted as a function of the absorbance of the sample itself and the front side signal measured by filtering the light with gray filters of absorbances up to 3. The backside illumination SPV signal show a relatively large scatter, but their values compare well to the values obtained from the front side illumination by the application of external filters. The signal obtained from the 50 nm thick layer is below the expected value from the pure inner filter effect. But it coincides with the signal obtained upon front illumination of the sample. This signal is lower than the one obtained from a thick sample due to other effects discussed above.

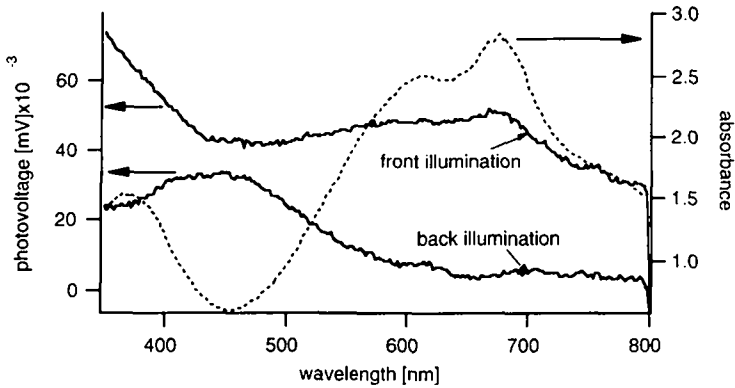


Fig. 5.31: SPS spectra of front and backside illumination of a 500 nm thick sample. The dashed line shows the absorption spectrum of the sample.

The results allow to conclude, that the depletion layer at the surface is confined to 100 nm or less and the depletion layer at the interface SnO<sub>2</sub>/DTPP to 200 nm or less. The difference of the work functions of 110 meV and the observed surface photovoltage of 80 meV indicate a total built in potential at the interface is 190 mV as a lower limit. It allows us to propose the following model for the energy band diagram of the SnO<sub>2</sub>/DTPP cell:

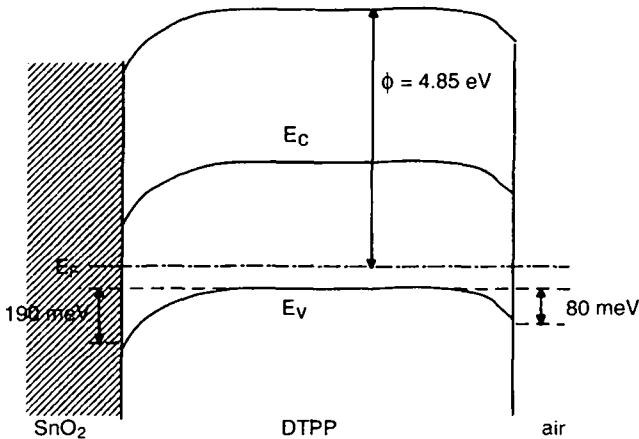


Fig. 5.32: Energy band diagram for the SnO<sub>2</sub>/DTPP cell

This model is in agreement with the photovoltaic behavior observed above for the SnO<sub>2</sub>/DTPP/Au solar cell, where a junction at the SnO<sub>2</sub>/DTPP interface allowed

the charge injection from DTPP to SnO<sub>2</sub> resulting in a photocurrent with the DTPP acting as a hole conductor, i.e. a p-type organic semiconductor.

## 5.6. Conclusion

The use of solid state DPP or DTPP for organic-on-inorganic solar cells has shown that the limitations of these compounds in the way they were applied are their exciton splitting efficiencies and the resistivities. The importance of the charge separation step was shown by the addition of a monomolecular layer of DPP derivatized to adsorb on the TiO<sub>2</sub> interface, thus ensuring the contact between the organic and inorganic semiconductors on the molecular scale. The I-V characteristics indicated that the charge carrier transport is a second limiting step in the overall performance. DMADPP has a promising dark conductivity but lacks photoconductivity for the application in photovoltaic cells.

From the SPV/SPS measurements a model for the energy bands in the SnO<sub>2</sub>/DTPP cell could be proposed in agreement with the characteristics of the photovoltaic cells. It was also shown that the comparison of back- and frontside illumination effects for different sample thicknesses allows to locate the band bendings within the layers and to give upper limits for the depth of the corresponding depletion layers.

## 5.7. References

- (1) Kuhn, H. H.; Child, A. D.; Kimbrell, W. C. *Synth. Met.* **1995**, *71*, 2139.
- (2) Kanatzidis, M. G. *C&EN* **1990**, *3*, 36-54.
- (3) McCoy, C. H.; Wrighton, M. S. *Chem. Mater.* **1993**, *5*, 914-916.
- (4) Law, K.-Y. *Chem. Rev.* **1993**, *93*, 449-486.
- (5) Wang, Y. In *Encyclopedia of Chemical Technology*; 4 ed.; Kirk-Othmer, Ed.; John Wiley & Sons: 1996; Vol. 18; pp 837.
- (6) Mori, T.; Sugimura, E.; Mizutani, T. *J. Phys. D: Appl. Phys.* **1993**, *26*, 452.
- (7) Adam, D.; Closs, F.; Frey, T.; Funhoff, D.; Haarer, D.; Ringsdorf, H.; Schuhmacher, P.; Siemensmeyer, K. *Phys. Rev. Lett.* **1993**, *70*, 457-460.
- (8) Lux, M.; Strohriegel, P. *Makromol. Chem.* **1987**, *188*, 811-820.
- (9) Kassi, H.; Hotchandani, S.; Leblanc, R. M. *Appl. Phys. Lett.* **1993**, *62*, 2283.
- (10) Scher, H.; Lax, M. *Phys. Rev.* **1973**, *B 7*, 4491-4502.
- (11) Scher, H.; Montroll, E. W. *Phys. Rev.* **1975**, *B12*, 2455-2477.
- (12) Bäessler, H.; Schönherr, G.; Abkowitz, M.; Pai, D. M. *Phys. Rev.* **1982**, *B 26*, 3105.
- (13) Kontani, T.; Muranoi, T.; Kukuma, I.; Masui, M.; Takuichi, M. *Jpn. J. Appl. Phys.* **1995**, *34*, 3654.
- (14) Ghosh, A. K.; Feng, T. *J. Appl. Phys.* **1978**, *49*, 5982-5989.
- (15) Boussaad, S.; Hotchandani, S.; Leblanc, R. M. *Appl. Phys.* **1993**, *63*, 1768.
- (16) Skotheim, T.; Yang, J.-M.; Otvos, J.; Klein, M. P. *J. Chem. Phys.* **1982**, *77*, 6144-6150.
- (17) Skotheim, T.; Yang, J.-M.; Otvos, J.; Klein, M. P. *J. Chem. Phys.* **1982**, *77*, 6151-6161.
- (18) Tang, C. W. *Appl. Phys. Lett.* **1986**, *48*, 183.
- (19) Chamberlain, G. A. *Solar Cells* **1983**, *10*, 199-210.
- (20) Panayotatos, P.; Prikh, D.; Sauers, R.; Bird, G.; Peichowski, A.; Husain, S. *Solar Cells* **1986**, *18*, 71-84.
- (21) Hiramoto, M.; Fujiwara, H.; Yokoyama, M. *J. Appl. Phys.* **1992**, *72*, 3781-3787.
- (22) Hiramoto, M.; Fujiwara, h.; Yokoyama, M. *Appl. Phys. Lett.* **1991**, *58*, 1062-1064.
- (23) Yu, G.; Gao, J.; Hummelen, J. C.; Wudl, F.; Heeger, A. J. *Science* **1995**, *270*, 1789-1791.
- (24) Popovic, Z. D.; Hor, A. M.; Loutfy, R. O. *Chem. Phys.* **1988**, *127*, 451.
- (25) Nazeeruddin, M. K.; Kay, A.; Rodicio, I.; Humphry-Baker, R.; Müller, E.; Liska, P.; Vlachopoulos, N.; Grätzel, M. *J. Am. Chem. Soc.* **1993**, *115*, 6382-6390.
- (26) O'Regan, B.; Grätzel, M. *Nature* **1991**, *353*,

- (27) Tennakone, K.; Kumara, G. R. R. A.; Kumarasinge, A. R.; Wijyantah, K. G. U.; Sirimanne, P. M. *Semiconductor Science Technology* **1995**, preprint for 10(1995) 1-5,
- (28) O'Regan, B. *preprint* **1996**,
- (29) O'Regan, B.; Schwartz, D. T. *Chemistry of Materials* **1995**, 7, 1349-1354.
- (30) Mizuguchi, J.; Rochat, A. C. *J. Imag. Sci.* **1988**, 32, 135-140.
- (31) Mizuguchi, J. *J. Appl. Phys.* **1989**, 66, 3111-3113.
- (32) Mizuguchi, J.; Homma, S. *J. Appl. Phys.* **1989**, 66, 3104.
- (33) Mizuguchi, J.; Rochat, A. C. *J. Imag. Tech.* **1991**, 17, 123-126.
- (34) Langhals, H. *J. Inf. Rec. Mater.* **1991**, 19, 449-454.
- (35) Mizuguchi, J. *Ber. Bunsenges. Phys. Chem.* **1993**, 97, 684-701.
- (36) Mizuguchi, J.; Rihs, G. *Ber. Bunsenges. Phys. Chem.* **1992**, 96, 597-606.
- (37) Gregg, B. A. *J. Phys. Chem.* **1996**, 100, 852.
- (38) Lagowski, J. *Surface Science* **1994**, 299/300, 92.
- (39) Kronik, L.; Burstein, L.; Leibovitch, M.; Shapira, Y.; Gal, D.; Moons, E.; Beier, J.; Hodes, G.; Cahen, D.; Hariskos, D.; Kelnk, R.; Schock, H.-W. *Appl. Phys. Lett.* **1995**, 67, 1405.
- (40) Iqbal, A.; Cassar, L.; Rochat, A. C.; Pfenninger, J.; Wallquist, O. *Journal of Coatings Technology* **1988**, 60, 37-45.
- (41) Mizuguchi, J.; Rochat, A. C.; Rihs, G. *Ber. Bunsenges. Phys. Chem.* **1992**, 96, 607-619.
- (42) Nazeeruddin, M. K.; Liska, P.; Moser, J.; Vlachopoulos, N.; Grätzel, M. *Helv. Ch. Acta* **1990**, 73, 1788-1803.
- (43) Fitzmaurice, D. J.; Frei, H. *Langmuir* **1991**, 7, 1129-1137.
- (44) Moser, J.; Grätzel, M. *J. Am. Chem. Soc.* **1984**, 106, 6557-6564.
- (45) Frei, H.; Fitzmaurice, D. J.; Grätzel, M. *Langmuir* **1990**, 6, 198-206.
- (46) Nüesch, F. Thesis, EPFL Switzerland, 1995.
- (47) Desilvestro, J.; Grätzel, M.; Kavan, L.; Moser, J.; Augustynsky, J. *J. Am. Chem. Soc.* **1985**, 107, 2988-2990.
- (48) Vlachopoulos, N.; Liska, P.; Augustynski, J.; Grätzel, M. *J. Am. Chem. Soc.* **1988**, 110, 1216-1220.
- (49) O'Regan, B.; Moser, J.; Anderson, M.; Grätzel, M. *J. Phys. Chem.* **1990**, 94, 8720-8726.
- (50) Hada, H.; Yonezawa, Y.; Inaba, H. *Ber. Bunsenges. Phys. Chem.* **1981**, 85, 425-430.
- (51) Moser, J.-E.; Graetzel, M.; Durrant, J. R.; Klug, D. R. In *Femtochemistry*; M. Chergui, Ed.; World Scientific: London, 1996.
- (52) Rehm, J. M.; McLendon, G. L.; Nagasawa, Y.; Yoshihara, K.; Moser, J. E.; Graetzel, M. *J. Phys. Chem.* **1996**, 100, 9577-9578.

- (53) Pechy, P.; Rotzinger, F. P.; Nazeeruddin, M. K.; Kohle, O.; Zakeeruddin, S. M.; Humphry-Baker, R.; Grätzel, M. *J. Chem. Soc. Chem. Commun.* **1995**, 1995, 65-66.
- (54) Gmelin In *Handbuch der anorganischen Chemie*; Vol. 41; pp 238.
- (55) Ruprecht, H. *Cosmetics and Toiletries* **1976**, 91, 30-33.
- (56) Hartman, P. In *Crystal Growth*; P. Hartman, Ed.; Elsevier: Amsterdam, 1973; Vol. 1; pp 367.
- (57) Barbé, C.; Arendse, F.; Comte, P.; Jirousek, M.; Lenzmann, F.; Shklover, V.; Grätzel, M. "Nanocrystalline TiO<sub>2</sub> electrodes for photovoltaic applications," accepted for publication, *J. Am. Cer. Soc.* 1997.
- (58) Shklover, V.; Nazeerruddin, M.; Zakeerruddin, S. M.; Barbé, C.; Haibach, T.; Steurer, W.; Hermann, R.; Nissen, H. U.; Grätzel, M. "Study of the structure of nanocrystalline TiO<sub>2</sub> powders and their highly efficient photosensitizer Ru(2,2'-bipyridyl-4,4'-dicarboxylate)<sub>2</sub>(SCN)<sub>2</sub>," EPFL, 1996.
- (59) Moser, J. E.; Grätzel, M. *Chem. Phys.* **1993**, 176, 493.
- (60) Kay, A. Thesis, EPFL, 1993.
- (61) Nüesch, F.; Moser, J. E.; Shklover, V.; Grätzel, M. *J. Am. Chem. Soc.* **1996**, 118, 5420.
- (62) Moser, J. E. Thesis, EPFL, 1986.
- (63) Planta, C. V. Thesis, EPFL, 1996.
- (64) Huang, S. Y.; Schlichthörl, G.; Lee, B. G.; Nozik, A. J.; Grätzel, M.; Frank, A. J. "Charge recombination in dye-sensitized nanocrystalline TiO<sub>2</sub> solar cells," NREL/EPFL, 1996.
- (65) Chassot, L.,
- (66) Chassot, L. *Chimia* **1994**, 48, 432-435.
- (67) Moser, J.; Punchihewa, S.; Infelta, P. P.; Grätzel, M. *Langmuir* **1991**, 7, 3012-3018.
- (68) Pauw, L. J. v. d. *Phil. Res. Rep.* **1958**, 13, 1.
- (69) Pauw, L. J. v. d. *Phil. Tech. Rev.* **1958**, 20, 220.
- (70) Schroder, D. K. *Semiconductor material and Device Characterization*; John Wiley & Sons, Inc.: New York, 1990, pp 599.
- (71) Meier, H. In *Organic semiconductors*; Verlag Chemie: Weinheim, 1974; pp 386.
- (72) Simon, J.; André, J.-J. *Molecular Semiconductors, Photoelectrical Properties and Solar Cells*; Springer-Verlag: Berlin Heidelberg, 1985, pp 290.
- (73) Arita, M.; Fukushima, K.; Homma, S.; Kura, H.; Yamamoto, H.; Okamura, M. *J. Appl. Phys.* **1991**, 70, 4065.
- (74) Lüth, H. *Appl. Phys.* **1975**, 8, 1.
- (75) Lüth, H. In *Surfaces and interfaces of solid materials*; 3 ed.; Springer Verlag: 1995; pp 464-471.

- (76) Moons, E.; Gal, D.; Beier, J.; Hodes, G.; Cahen, D.; Kronik, L.; Burstein, L.; Mishori, B.; Shapira, Y.; Hariskos, D.; Schock, H.-W. *Solar Energy Materials and Solar Cells* **1996**, *43*, 73.
- (77) Moons, E. Thesis, Weizmann Institute of Science, Rehovot, Israel, 1995.
- (78) Goldstein, B.; Redfield, D.; Szostak, D. J.; Carr, L. A. *Appl. Phys. Lett.* **1981**, *39*, 258.
- (79) Leibovitch, M.; Kronik, L.; Fefer, E.; Burstein, L.; Korobov, V.; Shapira, Y. *J. Appl. Phys.* **1996**, *79*, 8549.
- (80) Moons, E.; Savenije, T.; Goossens, A. "Direct determination of surface potential of porphyrin layers on ITO using Kelvin probe technique," Delft University of Technology, manuscript in preparation.
- (81) Pfeiffer, M.; Leo, K.; Karl, N. *J. Appl. Phys.* **submitted**,
- (82) Pfeiffer, M.; Leo, K.; Karl, N. In *Electronic and Related Properties of Organic Solids*; Poland, 1996; pp .
- (83) Hiramoto, M.; Ihara, K.; Fukusumi, H.; Yokoyama, M. *J. Appl. Phys.* **1995**, *78*, 7153.
- (84) Marshak, A. H. *IEEE Trans ED* **1989**, *36*, 1764.
- (85) Bockris, J. O.; Khan, S. U. M. *Surface Electrochemistry, a Molecular Level Approach*; Plenum Press: New York & London, 1993.
- (86) Bockris, J. O.; Reddy, A. K. N. *Modern Electrochemistry*; Plenum Press: New York, 1970.
- (87) Surplice, N. A.; D'Arcy, R. J. *J. Phys. E: Sci. Instr* **1970**, *3*, 477.
- (88) Reiss, H. *J. Phys. Chem.* **1985**, *89*, 3783.
- (89) Brillson, L. J.; Kruger, D. W. *Surface Science* **1981**, *102*, 518.



## 6. Conclusion

The investigations of the initiator step of the photochemical reactions of DPP pigments covered the compound as a pigment in a polymer matrix, the monomer in solution and molecular orbital calculations on the monomers. This chain of investigations allowed to

- link the photoactivity of the pigments to the molecular dye
- prove the involvement of singlet oxygen in the degradation of the molecular dye
- explain the mechanism of singlet oxygen sensitization from the DPP singlet and triplet excited states
- give some insight based on molecular orbital (MO) calculations to why this mechanism is important for this class of compounds.

From these results the conclusion could be drawn to that the NILES compounds act primarily as singlet oxygen quenchers rather than radical interceptors thus explaining why they are more efficient stabilizers than the HALS for the DPP pigments. TEMPO, a NILES compound, does however enhance the triplet yield of DPP and may therefore enhance the singlet oxygen sensitization. It must therefore be applied in a form that allows it to quench singlet oxygen even more efficiently than the DPP excited states.

The sensitization of singlet oxygen by DPP is possible due to the large singlet-triplet energy splitting of DPP. The MO calculations showed that this is a property of the core of the chromophore. Variation of the substituent allowed to correlate the MO calculation predictions to the experiment. Based on these observations a new substituent, *p*-diphenylamine, was proposed yielding a near infrared absorbing hole conductor based on the DPP chromophore. The bathochromic shift was predicted from the MO calculations and the hole conducting properties are inferred from the similarity of the triphenyl-amino groups thus formed with the triphenyl-amine found in a large variety of hole conductors.

The hole conducting properties were exploited for solid state solar cells using TiO<sub>2</sub> or SnO<sub>2</sub> and DPP or DTPP. Although only poor yields were achieved, the importance of the intimate contact between the two materials in a heterojunction was shown by the use of substituted DPP attached on the surface of a porous TiO<sub>2</sub> electrode thus insuring the contact at the interface of the heterojunction. The use of the dithioketo-DPP (DTPP) yielded somewhat higher photocurrents but showed still a poor charge generation efficiency. However the results show that the application of nanoporous TiO<sub>2</sub> electrodes in connection with organic hole

conductors is a viable concept for solid state photovoltaic devices involving organic/inorganic heterojunctions.

The use of Kelvin probe measurements and surface photovoltage spectroscopy for the system DTPP/SnO<sub>2</sub> showed that these methods are valuable tools for the investigation of highly resistive organic layers. Front- and backside illumination effects could be separated thus allowing to localize the band bending. Based on Kelvin probe in darkness and SPS results a band diagram could be proposed, indicating the presence of a p-type depletion layer both at the SnO<sub>2</sub>/DTPP and DTPP/air interfaces.

# Acknowledgement

First of all I would like to thank Prof. M. Grätzel for having given me the opportunity to work in his group. He thereby offered to me not only the possibility to do scientific research, but also to gather experience in industrial collaboration as a technology transfer assistant. Both research and industrial collaboration experience prove to be valuable enrichments for my professional orientation.

I am indebted to Dr. Jacques Moser who has not only managed the project's funding from CERS, but who was, with his scientific and experimental experience, my principal mentor during the PhD work. I appreciated his constructive sense of collaboration throughout our collaboration and his careful correction of the manuscript. I am grateful to Dr. V.J.P. Srivatsavoy who introduced many ideas to the first part of this thesis. I want to thank Dr. Ellen Moons for introducing the Kelvin probe technique in our group and for the stimulating collaboration we had. She showed me how fruitful an enthusiastic collaboration can be! Dr. Laurent Chassot, Ciba, is acknowledged for providing the DPP samples. I gratefully acknowledge Dr. François Rotzinger for his advice and the helpful discussions of the computational results, Dr. Peter Pechy for sharing with me his experience in organic synthesis, Dr. Augustin McEvoy for many discussions extending to the technology transfer and for correcting the manuscript, Dr. Chris Barbé for sharing his experience and for his commitment as a thin-film-group leader, Dr. Nick Vlachopoulos for doing the cyclic voltammetry measurements and Pascal Comte for promptly answering my "last minute orders" of TiO<sub>2</sub>-layers. Dr. Valery Shklover, ETH Zürich, is acknowledged for making the electron microscopy images of the solid samples. Almut Branner, Alexandre Closset and Monika Kowalczyk are acknowledged for their contributions during their respective student projects.

I would like to thank all the colleagues at the ICPII/LPI, especially my PhD student colleagues. Their friendship extended well beyond discussing science and added a great deal to the pleasure of working in this group.

Finally I would like to profoundly thank Maggie for her love and moral support especially during the period of writing up the thesis and my parents for giving me the personal strength to face such stressful periods.

# Curriculum vitae

Name: Martin Karl Eschle  
Date of birth: 5. January 1966  
Home village: Lucern  
Nationality: Swiss

## Education and degrees:

1973-1985: Primary, secondary and high school in Laufen/BE

1986-1991: Studies in Physics at EPFL  
Final examination January 1991: Ing. phys. dipl. EPFL  
Diploma work on "Characterization of sub micron MOSFET devices at low temperatures".

1992-1997: Graduate studies at the institute of physical chemistry, ICP2, at EPFL, under the direction of Prof. M. Grätzel

1993-1996: Studies in economics at the University of Lausanne, HEC.  
Final examination July 1996: Lic. HEC

## Work experience:

1986: Assistant programmer on PASCAL CAD applications at EIE SA, Genève (4 months)

1991: Research assistant at LBL, Chemical Biodynamics, Berkeley, CA under the direction of Dr. H. Frei (4 months)

1995-1996: Assistant for technology transfer for the license holders of ICP2-EPFL. 50% position in parallel with the research work for the Ph.D. project.